



Searches for invisibly decaying Higgs bosons with the CMS detector

Patrick James Dunne
of Imperial College London

A dissertation submitted to Imperial College London
for the degree of Doctor of Philosophy

Summary of Comments on Searches for invisibly decaying Higgs bosons with the CMS detector

Page: i

 Number: 1 Author: ptd Subject: Sticky Note Date: 10/06/2016 12:49:00

General Comments

=====

- there is some issue with extraneous full stops being added at the end of chapter headings, and at the end of figure, table and sectionn numbers. More details in my first comment in Chapter 1.
- there are many instances of numerical value and corresponding units not being separated (eg "800MeV" instead of "800 MeV" (normally there should be a half-space separating the two; in LaTeX: $800\,\text{MeV}$).
- use of personal pronouns (eg "I", "We") is usually avoided in scientific documentation. Use the passive voice instead.
- many instances of missing hyphens: either in composite words (such as "centre-of-mass", "four-momentum", "four-vector") or in words that are adjectivating the following noun (eg "two-hit track", "best-fit track").
- there are some occurrences of comma splices, which need to be fixed (typically by replacing the comma with a colon or semi-colon) (eg see Wikipedia).
- notation/conventions need to be adhered to consistently throughout. For instance, stick to "Run 1", not "run 1" or "Run I". Similarly for variables: for instance, in the transverse " p_T " variable, " p " should be italic (math mode) and " T " is in roman upright script.
- the formatting of the references has many obvious mistakes and inconsistencies: needs to be fixed.

Declaration

This dissertation is the result of my own work. Where figures and results are taken from other sources this is indicated by an appropriate reference. Some figures referenced as from other sources were created by me, but appear in other public documents.

The description of the analysis described in Chapter 4 follows Ref. [5], which includes elements of my work, and was ~~made public~~ [1]. Ref. [1]. Specifically, I was responsible for cross-checking the results of all the W+jets background estimations, I contributed to the development of the formula used to carry out the Z+jets background estimation, I calculated and cross-checked several of the systematic uncertainties, I produced plots of the discriminating variables for final publication, and I performed all limit setting and production of limit plots.

I was the main analyser for the analysis described in ~~Chapter 4.4~~, responsible for all steps of the analysis including trigger efficiency measurement, background estimation, systematic uncertainty studies and limit setting. The QCD background estimation method was developed and implemented collaboratively with other members of the Imperial College high energy physics (HEP) group. This work was ~~made public~~ [3] Ref. [2].

I was also solely responsible for the combinations described in Chapter 5. For the interpretations of the VBF invisibly decaying Higgs boson searches as limits on dark mater models described in Chapter 6 I worked collaboratively with theorists at Rutgers University and members of the Imperial College and Bristol University HEP groups. This work was ~~made public~~ [4] Ref. [4].

As well as the work described in this thesis I have also carried out preparations for a search for VBF produced invisibly decaying Higgs bosons using Run 2 data from the LHC. These preparations have included measurements of the trigger efficiency for the triggers used in 2015 CMS data taking and

Page: iv

 Number: 1 Author: ptd Subject: Inserted Text Date: 12/06/2016 14:32:04
published

 Number: 2 Author: ptd Subject: Highlight Date: 19/05/2016 15:14:48
Chapter 5
[fix Chapter splitting in current Chapter 4]

 Number: 3 Author: ptd Subject: Inserted Text Date: 12/06/2016 14:51:47
published

 Number: 4 Author: ptd Subject: Inserted Text Date: 12/06/2016 14:32:45
published

List of figures

1.1. Evidence for dark matter (DM): (a) Rotation velocity in the galaxy NGC 6503 as a function of distance from the galactic centre [28]. [1]	11
1.2. Feynman diagrams for the four standard model (SM) Higgs boson production processes with the highest cross-sections: gluon fusion (ggH) (a), vector boson fusion (VBF) (b), vector boson associated production (VH) (c) and top quark associated production (d).	14
1.3. Cross-sections for Higgs boson production via the most common production processes at $\sqrt{s} = 8$ TeV as a function of Higgs boson mass, m_H [29]. [3] The widths of the lines represent the theoretical uncertainties on the cross-section calculation.	15
1.4. Branching ratios for the dominant Higgs boson decays as a function of Higgs boson mass with the line widths representing the uncertainties (a), and the SM Higgs boson total width, Γ_H , as a function of Higgs boson mass (b) [29]. [4]	16
1.5. Best fit results for the decay signal strengths of the five highest branching ratio Higgs boson decays from a combination of CMS and ATLAS [34] Run 1 data (a). The negative log-likelihood as a function of $\mathcal{B}(H \rightarrow \text{inv})$, here denoted BR_{BSM} (b) [35]. [5]	16
1.6. Feynman diagrams for the dark matter theories considered. (a) VBF production of a scalar, H , or pseudoscalar A mediator. (b) Gluon based production of an H or A mediator. (c) An effective field theory where the mediator has been replaced by a contact interaction between the vector bosons and a hypothetical DM particle.	17

Page: X

Number: 1 Author: ptd Subject: Oval Date: 19/05/2016 15:18:38

In this and the following pages, the list of Figures contains many instances of this: garbled text due to a reference number overlapping with the text. Needs fixing throughout. I have not indicated all occurrences that need fixing, but please find them and fix them all.

Number: 2 Author: ptd Subject: Oval Date: 19/05/2016 15:15:55

Number: 3 Author: ptd Subject: Oval Date: 19/05/2016 15:16:23

Number: 4 Author: ptd Subject: Oval Date: 19/05/2016 15:16:12

Number: 5 Author: ptd Subject: Oval Date: 19/05/2016 15:16:17

Chapter 1.

Introduction and theory

In order to describe the search for invisible decays of the Higgs boson [2 ‘Higgs to invisible’), it is necessary to describe the theory behind them [3] and the statistical techniques used in carrying out the search. This chapter will start with an introduction to the current best theory of particle physics, the [4]SM, focusing on the Higgs mechanism, before outlining the motivations behind, and some candidates for, physics beyond the SM (BSM), then concluding with a discussion of the statistics of hypothesis testing. Natural units, where $\hbar = c = 1$, Einstein summation convention and Feynman slash notation are used throughout. [5]our vector indices are labeled using Greek letters, and gauge group generators using Roman letters.

1.1. The standard model of particle physics

The SM describes the interaction of the particles currently thought to be fundamental with the strong, weak and electromagnetic forces [6–9]. Its predictions, which come from specifying the symmetries the theory respects and how they are broken, the particles in the theory, and 18 free parameters, have been tested in many different experiments, in some cases up to one part in a trillion [10]. However, it does face challenges, one example being that it does not describe [6]DM.

The SM is a gauge invariant quantum field theory (QFT). To construct a QFT the symmetries that are respected by the theory and the fields it describes must be specified. The symmetries are important because of Noether’s theorem, which states that for every continuously differentiable symmetry of the Lagrangian of a theory there is a corresponding conservation law [11, 12]. An example of this is the conservation of energy,

Page: 2

 Number: 1 Author: ptd Subject: Highlight Date: 10/06/2016 00:04:00

[There should be no full stop here (and in every other chapter heading). There probably is some underlying issue causing these extraneous full stops. I have encountered this once before in a thesis in some other University, and suspect the issue is probably arising from the LaTeX template you are using...?]

It also affects the numbering of all sections, figures, tables: eg the section below is numbered "1.1.", whereas it should be "1.1"]

 Number: 2 Author: ptd Subject: Cross-Out Date: 20/05/2016 15:37:37

[remove: this does not seem to be adding anything new...]

 Number: 3 Author: ptd Subject: Inserted Text Date: 20/05/2016 15:37:54

it

 Number: 4 Author: ptd Subject: Highlight Date: 20/05/2016 15:49:57

standard model (SM)

[You can't use an acronym before you've defined it.]

I would also suggest you should write "Standard Model" (capitalised) but won't insist, as I know that "standard model" is sometimes also used.]

 Number: 5 Author: ptd Subject: Highlight Date: 20/05/2016 15:39:11

"Four vector indices" and "Four-vector indices" mean different things. The meaning you're after is the second one...

 Number: 6 Author: ptd Subject: Highlight Date: 20/05/2016 15:54:05

Dark Matter [or "dark matter"]

[I don't think using "DM" in running text to mean Dark Matter is a good idea. We don't use "HB" for Higgs boson, etc...]

 Number: 7 Author: ptd Subject: Highlight Date: 09/06/2016 23:34:44

[Some issue here: this should be page 1... not 2.]

linear momentum and angular momentum, which result through Noether's theorem from Poincaré invariance, the invariance of the laws of physics under translations and rotations in space and time. In addition to giving rise to conservation laws, some types of symmetry lead to additional fields being required to preserve 1 variance, this will be discussed further in Section 1.1.2 [13].

Because particles correspond to the quantised excitations of fields, the fields that can be described by the QFT are constrained by the fundamental particles seen in nature. In order to add a new field an explanation for why the corresponding particle has not yet been observed must, therefore, be provided. Specifically, a scalar field corresponds to a 2 in zero boson, spinor fields correspond to 3 in half fermions, and vector fields correspond to 4 in 1 bosons. We will now go through the particles observed in nature and how they are represented in the SM.

1.1.1. Fundamental particles in nature

There are two types of fundamental particles in nature, fermions and bosons. The fermions observed in nature that are currently thought to be fundamental are then divided into those which interact via the strong force (the quarks), and those which don't (the leptons). Both 5 in quarks and leptons exist in two further types: charged and neutral in the case of the leptons, and 6 in type and 7 in own type in the case of the fermions. Another interesting feature of the fermions is that they are arranged in three generations. Each generation has one fermion of each type with the same quantum numbers as those in the other generations, except that the mass is different. Table 1.1 shows this structure.

The bosons in nature also exist in two types. The first type are vector bosons, which mediate the three fundamental interactions described by the SM. The vector bosons are summarised in Table 1.2, where it can be seen that their masses are very different, the photon and the eight gluons being massless, while the W^\pm and Z bosons are massive. As we will see in Section 1.1.4, explaining these masses requires the Higgs mechanism [15–20]. The Higgs mechanism also gives rise to the other type of boson seen in nature, the scalar Higgs boson. In order to see how all of the above particles are represented in the SM, an introduction to gauge theories is necessary.

Page: 3

 Number: 1 Author: ptd Subject: Highlight Date: 20/05/2016 15:54:46
invariance. This

 Number: 2 Author: ptd Subject: Highlight Date: 20/05/2016 15:55:08
spin-0

 Number: 3 Author: ptd Subject: Highlight Date: 20/05/2016 15:56:58
spin-\$\frac{1}{2}\$

 Number: 4 Author: ptd Subject: Highlight Date: 20/05/2016 15:55:27
[hyphenate]
spin-1

 Number: 5 Author: ptd Subject: Cross-Out Date: 20/05/2016 15:57:43

 Number: 6 Author: ptd Subject: Highlight Date: 20/05/2016 15:58:11
up-type

 Number: 7 Author: ptd Subject: Highlight Date: 20/05/2016 15:58:24
down-type

Table 1.1.: The fundamental fermions observed in nature separated into their three generations. Each particle shown also has an antiparticle with opposite charge and identical mass [24]

Generation	Leptons			Hadrons		
	Particle	Mass	Electric Charge	Particle	Mass	Electric Charge
1	e^-	511 keV	-1	u	2.3 MeV	$+\frac{2}{3}$
	ν_e	~ 0	0	d	4.8 MeV	$-\frac{1}{3}$
2	μ^-	105.7 MeV	-1	c	1.275 GeV	$+\frac{2}{3}$
	ν_μ	~ 0	0	s	95 MeV	$-\frac{1}{3}$
3	τ^-	1.777 GeV	-1	t	173.2 GeV	$+\frac{2}{3}$
	ν_τ	~ 0	0	b	4.18 GeV	$-\frac{1}{3}$

Table 1.2.: The fundamental vector bosons observed in nature separated by the force which they mediate [14].

Force	Particle	Mass	Electric Charge
Electromagnetism	γ	0	0
Weak	W^\pm	80.4 GeV	± 1
	Z	91.2 GeV	0
Strong	g	0	0

Page: 4

T Number: 1 Author: ptd Subject: Highlight Date: 10/06/2016 00:00:07
[should be "1.1", not "1.1." - see comment at the very beginning of this chapter.]

T Number: 2 Author: ptd Subject: Highlight Date: 20/05/2016 16:01:34
"." missing

[Then add:]

The electric charges are given in units of the magnitude of the charge of the electron. [This also needs to be added to the caption of the Table below.]

1.1.2. Introduction to gauge theories

Gauge symmetries are local transformations, i.e. the transformation can be different at different points in space and time. To see the effect of imposing such a symmetry on a theory, consider imposing local invariance under $U(1)$ transformations on the Dirac Lagrangian for a fermion, ψ , with mass, [1]:

$$\mathcal{L} = i\bar{\psi}\not{\partial}\psi - m\bar{\psi}\psi [2] 1. \quad (1.1)$$

This Lagrangian is invariant under a global $U(1)$ transformation $\psi \rightarrow e^{iq\theta}\psi$, where [3] and θ are constant. However, if the $U(1)$ transformation is local i.e. θ is a function of spacetime position the Lagrangian is no longer invariant and transforms as:

$$\mathcal{L} \rightarrow \mathcal{L} - q(\partial_\mu\theta)\bar{\psi}\gamma^\mu\psi. \quad (1.2)$$

In order to restore invariance, a vector field, A_μ , referred to as a gauge field or gauge boson, which transforms as $A_\mu \rightarrow A_\mu + \partial_\mu\theta$ and has an interaction with the fermion field:

$$\mathcal{L}_{int} = q(\bar{\psi}\gamma^\mu\psi)A_\mu, \quad (1.3)$$

can be added to the theory. The interaction term of the new gauge field transforms as:

$$\mathcal{L}_{int} \rightarrow \mathcal{L}_{int} + q(\partial_\mu\theta)\bar{\psi}\gamma^\mu\psi, \quad (1.4)$$

which precisely cancels the non-gauge invariance seen in Equation 1.2. Assuming the new gauge field to be massless the Lagrangian is now:

$$\mathcal{L} = i\bar{\psi}\not{\partial}\psi - m\bar{\psi}\psi + q(\bar{\psi}\gamma^\mu\psi)A_\mu - \frac{1}{4}F_{\mu\nu}F^{\mu\nu}, \quad (1.5)$$

where $F_{\mu\nu}$ is the field strength tensor of the vector field. For a gauge boson from a general gauge group $F_{\mu\nu}$ is written as:

$$F_{\mu\nu}^a = \partial_\mu A_\nu^a - \partial_\nu A_\mu^a + g f_{abc} A_\mu^b A_\nu^c, \quad (1.6)$$

where f^{abc} are the structure constants of the gauge group, which are a representation of the commutation relations between the group's generators. For $U(1)$, which only has one self-commuting generator, the single structure constant is 0. However, for non-Abelian

Page: 5

 Number: 1 Author: ptd Subject: Highlight Date: 20/05/2016 16:02:26
m [21]:

 Number: 2 Author: ptd Subject: Cross-Out Date: 20/05/2016 16:02:52

 Number: 3 Author: ptd Subject: Highlight Date: 20/05/2016 16:04:34

\$q\$

[consistent use of notation; same as in the exponential factor you've just introduced]

gauge groups (i.e. those with non-commuting generators) they can be non-zero causing the $F_{\mu\nu}F^{\mu\nu}$ term in the Lagrangian to include self-interaction terms of the vector bosons.

Equation 1.5 can be rewritten as:

$$\mathcal{L} = i\bar{\psi}\gamma^\mu \mathcal{D}_\mu \psi - m\bar{\psi}\psi - \frac{1}{4}F_{\mu\nu}F^{\mu\nu}, \quad (1.7)$$

where $\mathcal{D}_\mu = \partial_\mu + iqA_\mu$ and is referred to as the covariant derivative. Comparing Equation 1.1 and Equation 1.7 it can be seen that to go from a globally invariant Lagrangian to a locally invariant one we have substituted the normal spacetime derivative for the covariant derivative and added the free term of the vector field.

In the case of $U(1)$ transformations, which have one degree of freedom ~~so~~ 1 can be described by one ~~2~~ parameter, in the above case θ , in order to make the Lagrangian locally invariant one interacting gauge boson had to be added. This correspondence between the number of degrees of freedom and the number of gauge bosons holds generally. For each degree of freedom of a group's transformations there exists a generator of the group, and for each generator one interacting gauge boson must be added to achieve local invariance.

1.1.3. The SM gauge group and fundamental particle representations

The SM is locally gauge invariant under the group $SU[4]_C \otimes SU(2)_L \otimes U(1)_Y$. $SU(3)[3]$ is the group governing the strong force interactions which couple to colour charge, C. $SU(2)_L$, which couples to ~~5~~ ft handed fermions, L, and $U(1)_Y$, which couples to weak hypercharge, Y are the groups governing the electroweak interactions. The weak hypercharge of any given particle is:

$$Y = 2(Q - T_3), \quad (1.8)$$

where Q is the electric charge, and T_3 is the third component of the weak isospin, which is $\pm \frac{1}{2}$ for ~~6~~ ft handed fermions, and zero for all other particles.

Fermions in the SM are spin half spinor representations of these symmetry groups. These spinors can be split into chirally ~~7~~ left and right handed components using the projection operators $P_L = \frac{1}{2}(1 \mp \gamma^5)$. Chirally ~~8~~ ft and ~~9~~ ght handed fermions transform differently under $SU(2)_L$. The ~~10~~ ht handed spinors are not charged under $SU(2)_L$ and thus are represented as a singlet, while the left handed spinors transform as a doublet.

Page: 6

 Number: 1 Author: ptd Subject: Inserted Text Date: 20/05/2016 16:05:01
and therefore

 Number: 2 Author: ptd Subject: Highlight Date: 20/05/2016 16:06:15
parameter (θ , in the case above)

 Number: 3 Author: ptd Subject: Cross-Out Date: 20/05/2016 16:40:25
[remove extraneous ")"]

 Number: 4 Author: ptd Subject: Highlight Date: 20/05/2016 16:42:40
[there shouldn't be a space between "SU" and "(3)", dito in SU(2), U(1). Please fix here and throughout the thesis.]

 Number: 5 Author: ptd Subject: Highlight Date: 20/05/2016 16:38:14
as "left handed" is being used to adjecivate "fermions", you have to hyphenate it: "left-handed fermion"

 Number: 6 Author: ptd Subject: Highlight Date: 20/05/2016 16:38:44
[hyphenate]

 Number: 7 Author: ptd Subject: Highlight Date: 20/05/2016 16:39:16
spin-1/2 [as before]

 Number: 8 Author: ptd Subject: Highlight Date: 20/05/2016 16:39:31
left-

 Number: 9 Author: ptd Subject: Highlight Date: 20/05/2016 16:39:49
[hyphenate]

 Number: 10 Author: ptd Subject: Highlight Date: 20/05/2016 16:43:01
[hyphenate]

The first generation of leptons can, therefore, be written as:

$$\psi_1 = e_R, \psi_2 = L = \begin{pmatrix} \nu_e \\ e_L \end{pmatrix}. \quad (1.9)$$

The SM treats neutrinos as massless and has no **light handed** neutrino. Similarly the first generation of quarks can be written as:

$$\psi_3 = u_R, \psi_4 = d_R, \psi_5 = \begin{pmatrix} u_L \\ d_L \end{pmatrix}. \quad (1.10)$$

As we saw in Section 1.1.2 gauge symmetries in theories with fermions require the addition of an interacting vector boson per symmetry generator to preserve gauge invariance. $SU(3)_C$ has eight generators whose eight vector bosons, $G_{a\mu}$, correspond to the eight physical gluons of QCD, which mediate the strong interaction. $SU(2)_L$ has three generators whose three vector bosons, W_μ^i , mix with the one vector boson from $U(1)_Y$, B_μ unifying the electromagnetic and weak forces into one electroweak force. The physical states that result are:

$$\begin{aligned} W^\pm_\mu &= \frac{1}{\sqrt{2}} (W_\mu^1 \mp i W_\mu^2) \\ Z_\mu &= \boxed{2} ps(\theta_W) W_\mu^3 - \boxed{3} n(\theta_W) B_\mu \\ A_\mu &= \boxed{4} n(\theta_W) W_\mu^3 + \boxed{5} ps(\theta_W) B_\mu, \end{aligned} \quad (1.11)$$

where θ_W is the Weinberg (weak) mixing angle and A_μ is the photon field. Also, as described in Section 1.1.2 the interaction between these vector bosons and the fermion fields occurs through their presence in the covariant derivative, and interactions between the vector bosons occur because $SU(3)_C$ and $SU(2)_L$ are non-Abelian.

Now let **6s** try to construct a Lagrangian for these fields. First ignoring the masses **7e** find:

$$\mathcal{L} = i \bar{\psi}_i \not{D} \psi_i - \frac{1}{4} F_{\mu\nu j} F_j^{\mu\nu}, \quad (1.12)$$

Page: 7

 Number: 1 Author: ptd Subject: Highlight Date: 20/05/2016 16:43:14

 Number: 2 Author: ptd Subject: Highlight Date: 20/05/2016 17:10:27

[use the LaTEX \cos command; as you have for used \ln and \tan in eg Eqtns 1.39 and 2.3, and in page 8.]

 Number: 3 Author: ptd Subject: Highlight Date: 20/05/2016 16:33:26

 Number: 4 Author: ptd Subject: Highlight Date: 20/05/2016 16:33:30

 Number: 5 Author: ptd Subject: Highlight Date: 20/05/2016 16:33:32

 Number: 6 Author: ptd Subject: Highlight Date: 20/05/2016 17:08:26

Use of personal pronouns (such as "I", "we", "us") is normally avoided in scientific papers (and theses as well, which are supposed to conform to the same writing standard). This whole sentence is definitely colloquial; something you would say in conversation, but wouldn't write in a scientific paper.

I suggest you rewrite as

"Ignoring mass terms, a Lagrangian for these fields can be constructed:"

 Number: 7 Author: ptd Subject: Highlight Date: 20/05/2016 16:51:26

where the sum over all ψ also includes the second and third generations, $F_{\mu\nu}F_j^{\mu\nu}$ is a sum of the free terms of all the SM gauge bosons and \mathcal{D} is the SM covariant derivative:

$$\mathcal{D}_\mu = \partial_\mu + ig_1 \frac{Y}{2} B_\mu + ig_2 \frac{\tau_i}{2} W_\mu^i + ig_3 \frac{\lambda_a}{2} G_\mu^a, \quad (1.13)$$

with Y being the constant generator of $U(1)$, τ_i the generators of $SU(2)_L$, λ_a the generators of $SU(3)_C$ and g_i the coupling constants of the fields. It should be noted that $\frac{g_1}{g_2}$ is equal to $\tan(\theta_W)$.

When we try to include mass a problem occurs. We know that some of the fermions have mass, and consequently we should have fermion mass terms of the form:

$$\begin{aligned} \mathcal{L}_{m_f} &= -m_f \bar{f} f \\ &= -m_f \bar{f} \left[\frac{1}{2} (1 - \gamma^5) + \frac{1}{2} (1 + \gamma^5) \right] f \\ &= -m_f (\bar{f}_R f_L + \bar{f}_L f_R), \end{aligned} \quad (1.14)$$

in our Lagrangian. However, as the left and right handed fields do not transform in the same way under $SU(2)_L$, this term breaks the gauge symmetry of the Lagrangian and can't be present.

A similar problem occurs for vector fields. In Section 1.1.2 we didn't consider the mass term of these vector fields:^[1]

$$\mathcal{L}_{m_V} = \frac{1}{2} m_V^2 A_\mu A^\mu \quad [2] \quad (1.15)$$

which is ^[3] gauge invariant, so it is not possible to include the massive vector bosons on their own in gauge invariant theories either. The additional piece of the SM required to allow particles to have mass is the Higgs mechanism.

1.1.4. Spontaneous symmetry breaking and the Higgs mechanism

The Higgs mechanism is a form of spontaneous symmetry breaking [15–20]. A symmetry is said to be spontaneously broken when the Lagrangian remains invariant while the vacuum state, i.e. that with lowest energy, does not [21]. Terms of the Lagrangian which are not gauge invariant can then be incorporated into the theory by adding a field which has a non-zero vacuum expectation value and coupling it to the other fields present in

Page: 8

 Number: 1 Author: ptd Subject: Inserted Text Date: 20/05/2016 17:19:25
[Re-write in passive voice to avoid use of "we" ...:]

"mass terms for the vector fields were not considered:"

 Number: 2 Author: ptd Subject: Inserted Text Date: 20/05/2016 17:20:54
Replace comma with full stop.

 Number: 3 Author: ptd Subject: Inserted Text Date: 20/05/2016 17:19:51
"Such terms are"

the desired term. For the Higgs mechanism this field is a complex scalar $SU(2)_L$ doublet, ϕ , called the Higgs field:

$$\phi = \begin{pmatrix} \phi^+ \\ \phi^0 \end{pmatrix}. \quad (1.16)$$

The main part of the Higgs field Lagrangian is:

$$\mathcal{L} = T - V = (\mathcal{D}_\mu \phi)^\dagger (\mathcal{D}^\mu \phi) + \mu^2 \phi^\dagger \phi - \lambda (\phi^\dagger \phi)^2, \quad (1.17)$$

Where the first two terms on the right hand side make up the kinetic part of the Higgs field Lagrangian, T , and the third term is the Higgs field potential, V . For $\mu^2 > 0$, the values of the Higgs field which minimise the Lagrangian are non-zero and form a circle in the phase space of ϕ . All of these minima are equivalent and a particular minimum can be chosen with no physical effect. By convention we choose the following minimum:

$$\langle 0 | \phi | 0 \rangle = \begin{pmatrix} 0 \\ \sqrt{\frac{\mu^2}{2\lambda}} \end{pmatrix} = \frac{1}{\sqrt{2}} \begin{pmatrix} 0 \\ v \end{pmatrix}. \quad (1.18)$$

~~Next we consider~~ Small perturbations around this ~~minimum~~ gives: Ignoring perturbations that can be set to zero by gauge freedom gives:

$$\phi = \begin{pmatrix} 0 \\ v + H \end{pmatrix}. \quad (1.19)$$

Inserting this into Equation 1.17 and ignoring terms with more than one type of field gives at leading order:

$$\mathcal{L} = \frac{1}{2} \partial_\mu H \partial^\mu H - \frac{1}{2} \mu^2 H^2 + \frac{v^2}{8} [g_2^2 W_\mu^+ W^{+\mu} + g_2^2 W_\mu^- W^{-\mu} + (g_1^2 + g_2^2) Z_\mu Z^\mu]. \quad (1.20)$$

As expected, the weak vector bosons W_μ^\pm and Z_μ acquire masses $\frac{g_2 v}{2}$ and $\frac{v}{2} \sqrt{g_1^2 + g_2^2}$ respectively. We also see an additional massive scalar H , which is the Higgs boson, with mass $\sqrt{2}\mu$. The photon and gluons do not acquire masses, as the particular choice of coupling constants and the structure of the group generators leads to the terms in A_μ and $G_{\mu a}$ being zero.

Page: 9

 Number: 1 Author: ptd Subject: Highlight Date: 20/05/2016 17:21:59
minimum and ignoring

 Number: 2 Author: ptd Subject: Inserted Text Date: 20/05/2016 17:21:43
Next, considering

 Number: 3 Author: ptd Subject: Inserted Text Date: 20/05/2016 17:22:39
[inser comma]

The final part of the Higgs field Lagrangian is that giving rise to the fermion masses. These are generated by a Yukawa term in the Lagrangian for each fermion as follows:

$$\mathcal{L}_{Yuk} = y_f (\bar{f}_L \phi f_R + \bar{f}_R \phi^\dagger f_L), \quad (1.21)$$

where y_f is the Yukawa coupling. The fermion's mass is then $\frac{y_f v}{\sqrt{2}}$, so heavier fermions couple more strongly to the Higgs boson. The SM provides no prediction of, or relationship between, the Yukawa couplings of the fermions, however they can be determined using the observed masses of the fermions.

A scalar particle with a mass of approximately 125 GeV, consistent with the SM Higgs boson, was discovered in 2012 by both the ATLAS and CMS collaborations [22, 23].

1.1.5. Dark matter

Despite its many successes, there are phenomena in nature which the SM does not explain. It does not predict the non-zero neutrino masses which are necessary to explain neutrino oscillation experiments [24]. It also does not predict sufficient violation of CP symmetry to explain the large matter-anti-matter asymmetry observed in the universe [21]. However, one of the most striking differences between observation and the SM prediction is the existence of **[1] M**.

Evidence for **[2] M** was first observed in studies of the rotation velocity of galaxy clusters as a function of distance from the centre of the cluster [25]. **[3]** shown in Figure 1.1a, these rotation velocities cannot be explained without the addition of significant additional non-luminous matter, or a modification of the laws of gravity. Further evidence for dark matter is provided by gravitational lensing and X-ray images of galaxy clusters such as the bullet cluster, shown in Figure 1.1b [26]. The figure shows two galaxy clusters which have passed through each other. It can be seen that the visible mass of the ~~galaxy~~**[4]** indicated by the colour-scale, is not in the same place as the majority of the gravitational mass, indicated by the green contours. This difference indicates that most of the mass in the clusters continues unimpeded on collision, and is not visible, i.e. it is **[6] M**. Cosmological observations suggest that **[8] M** makes up $\sim 25\%$ of the energy in the universe [27].

Page: 10

 Number: 1 Author: ptd Subject: Highlight Date: 20/05/2016 17:32:56

dark matter

[repeats: please fix here and everywhere else in the thesis.]

 Number: 2 Author: ptd Subject: Highlight Date: 20/05/2016 17:23:44

 Number: 3 Author: ptd Subject: Inserted Text Date: 20/05/2016 17:31:55

[Figure 1.1a refers to a single galaxy, not a galaxy cluster (which is what the previous sentence refers to). Therefore you need to make clear the transition between the two. I suggest you insert the following:]

"Evidence for dark matter has also been conclusively found from measurements of the rotation velocity in individual galaxies."

 Number: 4 Author: ptd Subject: Inserted Text Date: 20/05/2016 17:35:41

clusters

 Number: 5 Author: ptd Subject: Highlight Date: 20/05/2016 17:34:04

 Number: 6 Author: ptd Subject: Highlight Date: 20/05/2016 17:23:57

 Number: 7 Author: ptd Subject: Highlight Date: 20/05/2016 17:24:26

 Number: 8 Author: ptd Subject: Highlight Date: 20/05/2016 17:34:11

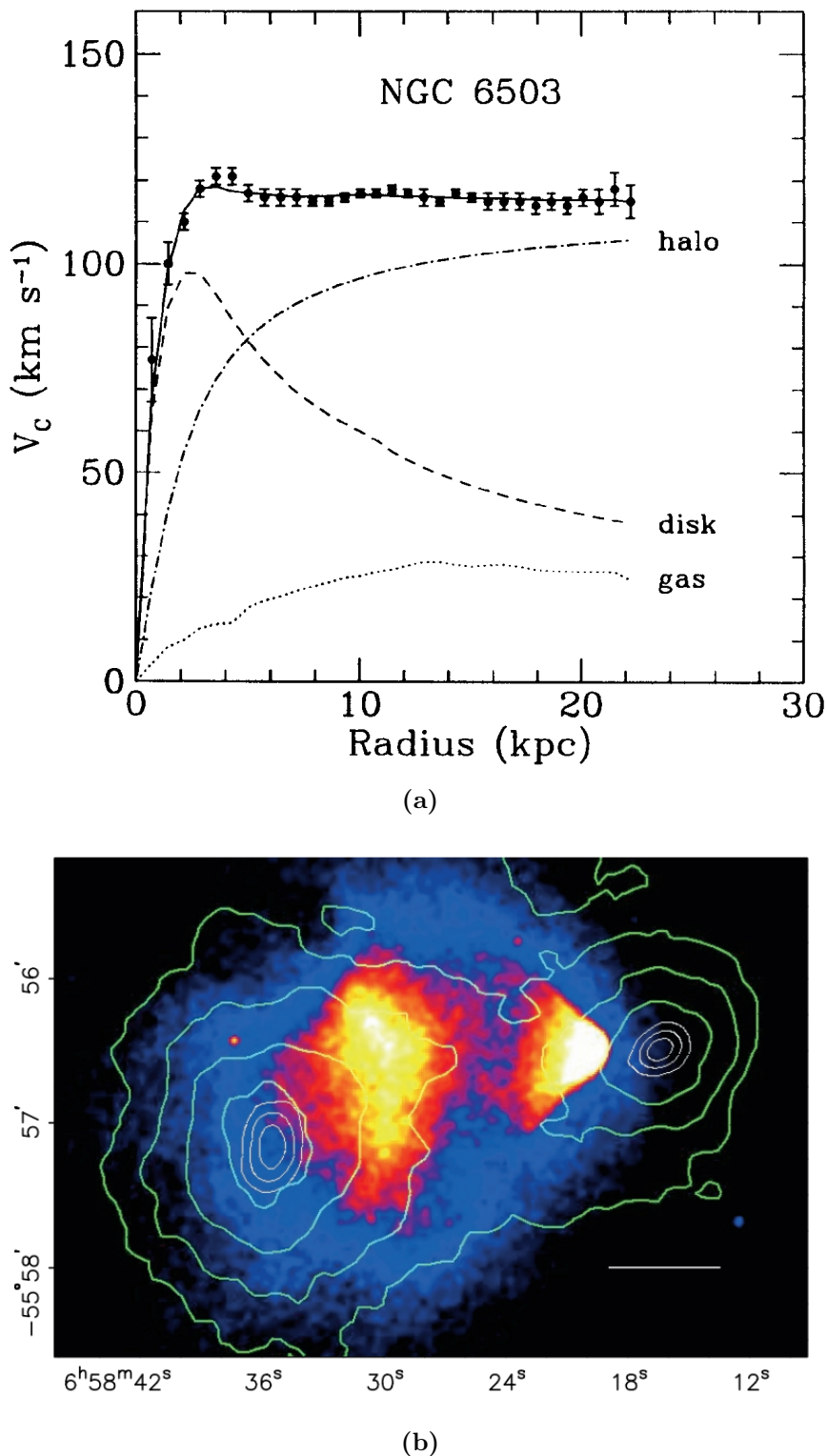


Figure 1.1: Evidence for 2D M: (a) Rotation velocity in the galaxy NGC 6503 as a function of distance from the galactic centre [28]. (b) The disk and gas components shown are made of visible matter, while the halo component shows the effect of adding an additional 3D M halo to the galaxy. A superposition of X-ray (colour-scale) and gravitational lensing (green contours) images of the bullet cluster of galaxies [26].

Page: 11

 Number: 1 Author: ptd Subject: Highlight Date: 10/06/2016 00:00:34
[should be "1.1", not "1.1." - see comment at the very beginning of this chapter.]

 Number: 2 Author: ptd Subject: Highlight Date: 20/05/2016 17:24:39

 Number: 3 Author: ptd Subject: Highlight Date: 20/05/2016 17:24:41

1.2. Searching for dark matter with Higgs bosons

A SM 125 GeV Higgs boson can only decay to invisible final states by first decaying to a pair of Z bosons, which then both decay to neutrinos. The branching fraction for this process is less than 1% [29], so the observation of larger invisible branching ratios of the Higgs boson, $\mathcal{B}(H \rightarrow \text{inv})$, would be strong evidence for new physics and could indicate couplings to DM-like particles. Observing decays of Higgs or Higgs-like bosons to **[1DM]** presents an experimental problem in that the final state particles are not visible to the particle detectors used at the Large Hadron Collider (LHC), such as the Compact Muon Solenoid, CMS [30], which the data used in this thesis were collected with. Therefore, if a Higgs boson were to be created alone and decay to DM there would be no way to observe these decays. Fortunately, several Higgs boson production mechanisms (as described in Section 1.2.1 below), lead to additional particles being created with the Higgs boson. By conservation of momentum, the vectorial sum of the momenta of these additional particles transverse to the LHC beams will be non-zero due to the unobserved particles. This missing transverse momentum, \cancel{E}_T , can therefore be used to identify the presence of **[2DM]** particles in the event. This type of search is referred to as a direct search.

Another indication of Higgs boson decays to unseen particles would be a difference between the total decay width of the Higgs boson and the sum of the decay widths of all visible decays. This type of search is referred to as an indirect search. For both direct and indirect searches it is necessary to understand how the Higgs boson is produced and how it decays.

1.2.1. Higgs boson production and decay at the LHC

The LHC (discussed in detail in Section 2.1) collides protons at high energies. The results of these collisions are referred to as “events”. The dominant production mechanisms for Higgs bosons in high energy proton collisions are shown in Figure 1.2, and they have the cross-sections shown in Figure 1.3. It can be seen that ggH production, where two gluons fuse via a quark loop to produce a Higgs boson (as shown in Figure 1.2a), has the highest cross-section across the full Higgs boson mass range shown. Unfortunately, this production mode normally results in no visible particles in the final state and therefore most ggH events cannot be used to search for invisibly decaying Higgs bosons. In some ggH events there is QCD radiation from the initial state particles (initial state radiation (ISR)). Due to asymptotic freedom [31, 32] these radiated quarks and gluons

Page: 12

 Number: 1 Author: ptd Subject: Highlight Date: 20/05/2016 17:24:47

 Number: 2 Author: ptd Subject: Highlight Date: 20/05/2016 17:24:50

which is only approximate, but greatly decreases the computational power needed to process the same number of events.

Several MC generators are used to carry out the perturbative hard-scattering calculations. Some, such as PYTHIA [41], are also able to provide the hard-scatter calculation for a wide ranges of processes as well as perform other stages of the factorisation. Others like MADGRAPH [42] and POWHEG [43–45] only calculate the hard-scattering component. However, these other generators produce more accurate results for certain processes they have been tuned to, or allow for a larger range of processes to be simulated than the multipurpose generators such as PYTHIA. In all of the MC samples used in this thesis, the results of the hard-scatter are then passed on to PYTHIA for parton showering and hadronisation.

Finally, some generators, such as MCFM [46], VBFNLO [47–49], TOP++ [50] and FEWZ [51] are used only to calculate cross-sections very accurately at next-to-leading order (NLO) or next-to-next-to-leading order (NNLO). These calculations are much more computationally intensive than the lower order calculations above, which renders them unsuitable for generating full MC samples with a four vector for each final state particle.

1.4. Statistics of exclusion limits

Limits on the parameters of theoretical models are presented throughout this thesis. These limits are set by performing a hypothesis test to discriminate between a null, **background only** model, hypothesis, b and a test hypothesis, the signal process, s , plus background model. The particular procedure used is based on the CL_S statistic and was developed by the LHC Higgs Combination Group [53]. This procedure is used by both the ATLAS [34] and CMS experiments.

The procedure starts by defining a likelihood function, \mathcal{L} , which quantifies how likely a certain observation is given the expectation under a given hypothesis. \mathcal{L} takes the form:

$$\mathcal{L} = \prod_i \text{Poisson}(n_i | \nu_i(\mu, \theta)) \cdot \prod_j \text{Constraint}(\theta_j, \bar{\theta}), \quad (1.38)$$

where the first term is the contribution from the Poisson probability to observe n_i events in each analysis category, i , given a predicted number of events from the hypothesis, ν_i . ν_i is a function of a signal strength parameter, μ , which in the case of the signal

 Number: 1 Author: ptd Subject: Highlight Date: 05/06/2016 20:07:22

background-only

[need to hyphenate, as "background-only" adjectivates "model"]

hypothesis being an SM Higgs boson is 1 for the SM and 0 for the background only case, and the “nuisance parameters,” θ , which account for the uncertainties on parameters of the signal and background models and any correlations between them. The second term in Equation 1.38 represents the constraints on the allowed values of these nuisance parameters, with $\bar{\theta}$ being the best estimate of θ obtained from external measurements. The shape of the constraint function varies depending on the nuisance parameter it represents. For example, uncertainties on the event yield in a category are usually modelled with log-normal constraints, which exclude negative values of the event yield.

Profile likelihood ratios, q_μ , are then calculated, which are defined as:

$$q_\mu = -2 \ln \frac{\mathcal{L}(obs|\mu \cdot s + b, \hat{\theta}_\mu)}{\mathcal{L}(obs|\hat{\mu} \cdot s + b, \hat{\theta})}, \quad (1.39)$$

where obs is the observation, and $\hat{\mu}$ and $\hat{\theta}$ are the values of μ and θ where the likelihood is maximised given the constraint $0 \geq \hat{\mu} \geq \mu$. $\hat{\theta}_\mu$ are the values of the nuisance parameters that maximise the likelihood for a given μ . The profile likelihood ratio therefore describes how likely it is to observe a signal strength equal to or higher than μ compared to the most likely signal strength.

The CL_s statistic itself is then defined as:

$$CL_s = \frac{P(q_\mu \geq q_\mu^{obs} | \mu \cdot s + b)}{P(q_\mu \geq q_\mu^{obs} | b)}, \quad (1.40)$$

where the probability P of a given q_μ can be calculated using the asymptotic limit approximation [54]. The region in which a signal strength $\mu \cdot s$ is excluded at the $1 - \alpha$ CL is then the region for which CL_s is less than or equal to α , i.e. when the signal hypothesis is α times less probable than the background.

Page: 23

 Number: 1 Author: ptd Subject: Highlight Date: 05/06/2016 20:33:17
background-only

[needs to be hyphenated, as it modifies the noun that follows]

 Number: 2 Author: ptd Subject: Highlight Date: 05/06/2016 20:08:14
parameters

Chapter 2.

The LHC and the CMS experiment

This chapter introduces the CMS experiment and the LHC[55]. In Section 2.1 an overview of the LHC and the chain of accelerators which feed into it is given. This is then followed in Section 2.2 by a description of the CMS experiment focusing on the aspects most relevant to the search for invisibly decaying Higgs bosons.

2.1. The LHC

The LHC is situated **100m** underground in a tunnel formerly built for the LEP accelerator [56] at CERN near Geneva, Switzerland. It is a **27km** storage ring which accelerates both protons and heavy ions and collides them at the highest centre of mass energies of any collider built to date. The work contained in this thesis uses data from proton-proton collisions. These protons are obtained by taking hydrogen gas and stripping its atoms of their electrons with an electric field. The first accelerator in the chain of accelerators feeding into the LHC, Linac 2, accelerates the protons to 50 MeV. The protons are then accelerated to 1.4 GeV by the next accelerator, the Proton Synchrotron Booster (PSB), which is followed by the Proton Synchrotron (PS) where they reach 25 GeV. The beam energy is then increased to 450 GeV in the Super Proton Synchrotron (SPS). Finally, the protons are injected into the LHC where, at **time** of writing, the maximum energy the beams have been accelerated to is 6.5 TeV, close to the design maximum of 7 TeV.

When fully filled the LHC contains two counter-rotating beams which are formed of up to 2808 bunches spaced **25 ns** apart and each containing $\mathcal{O}(10^{11})$ protons. The two beams are kept travelling in a **circle** by 1232 superconducting dipole magnets and steered to four collision points around the LHC. Detectors are situated at these

Page: 24

 Number: 1 Author: ptd Subject: Highlight Date: 05/06/2016 20:10:15
[the value and the units need to be separated, normally by a half-space:]

"100\,m"

 Number: 2 Author: ptd Subject: Highlight Date: 05/06/2016 20:10:24
27\,km

 Number: 3 Author: ptd Subject: Inserted Text Date: 05/06/2016 20:10:45
the

 Number: 4 Author: ptd Subject: Cross-Out Date: 05/06/2016 20:11:31

 Number: 5 Author: ptd Subject: Cross-Out Date: 05/06/2016 20:16:56
[when fully filled there is no 50 ns option.]

 Number: 6 Author: ptd Subject: Inserted Text Date: 05/06/2016 20:17:23
closed orbit

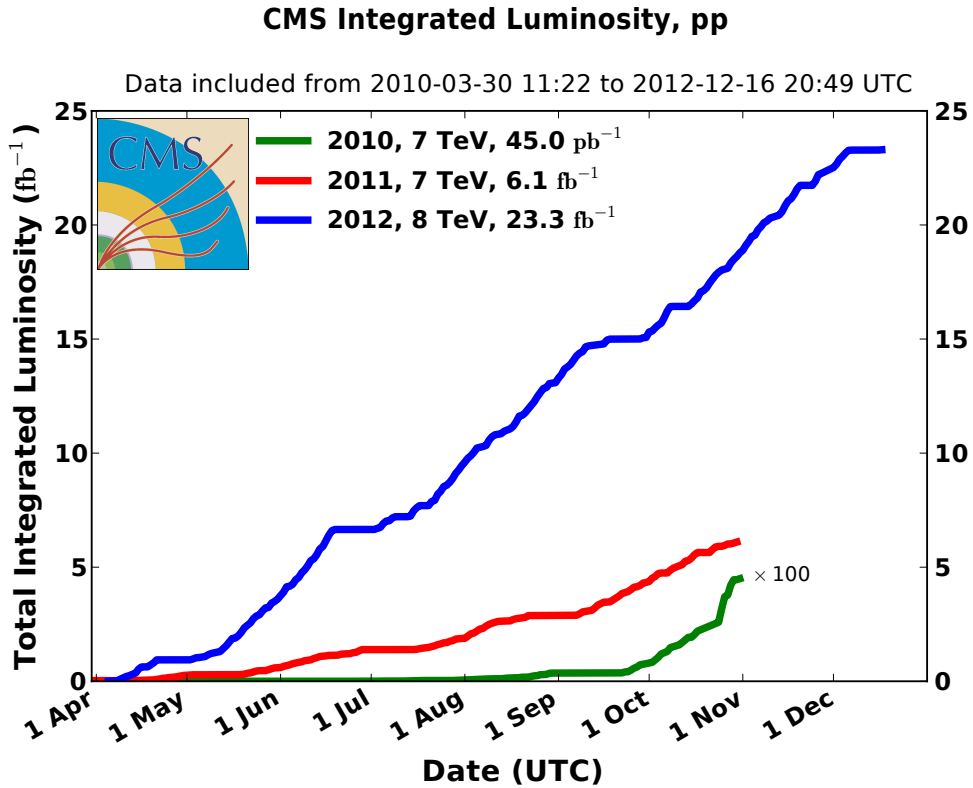


Figure 2.2.: A summary of the luminosity delivered to CMS during Run 1 of the LHC [61].

where k_b is the number of bunches per beam, N_b the number of protons per bunch, f_{rev} the revolution frequency, ϵ_n the normalised transverse beam emittance, β^* the beta-function at the interaction point and γ the Lorentz factor. The design instantaneous luminosity of the LHC is $10^{34} \text{ cm}^{-2}\text{s}^{-1}$ with 25 bunch spacing. The integrated luminosity is defined as $\mathcal{L}_{int} = \int \mathcal{L} dt$.

The LHC started physics runs in 2010, during which it operated at a centre of mass energy of 7 TeV and delivered an integrated luminosity of 45.0 pb^{-1} to CMS. In 2011 the LHC also operated at 7 TeV and delivered 6.1 fb^{-1} to CMS. The centre of mass energy was increased to 8 TeV in 2012 and 23.3 fb^{-1} of data were delivered to CMS. A summary of the luminosity delivered to CMS during the three periods of Run 1 can be seen in Figure 2.2. In Run 2 the centre of mass energy was further increased to 13 TeV and during 2015 4.09 fb^{-1} of data were delivered to CMS at this energy. In order to be used for physics analysis data must be certified. This certification ensures that the detector was fully operational when the data were recorded. In 2011 5.1 fb^{-1} were certified, in 2012 19.7 fb^{-1} were certified and in 2015 2.2 fb^{-1} were certified.

Page: 26

 Number: 1 Author: ptd Subject: Inserted Text Date: 05/06/2016 20:18:12
\\ [insert half space to separate value and units]

 Number: 2 Author: ptd Subject: Highlight Date: 05/06/2016 20:21:13
"centre-of-mass"
[this is a compound word, always hyphenated; please fix here and everywhere.]

 Number: 3 Author: ptd Subject: Highlight Date: 05/06/2016 20:25:35
[In the rest of this page, everywhere there is an energy in TeV there seems to be too much space between the value and the unit (2 spaces, in some cases?). Conversely, everywhere where there is a luminosity in fb^-1 there is no space between the value and the unit. Use half-spaces ("\\," in LaTeX) to separate each value for the corresponding unit. This should be fixed here and throughout the thesis.]

 Number: 4 Author: ptd Subject: Highlight Date: 05/06/2016 20:25:53

 Number: 5 Author: ptd Subject: Highlight Date: 05/06/2016 20:25:47

 Number: 6 Author: ptd Subject: Highlight Date: 05/06/2016 20:21:47

 Number: 7 Author: ptd Subject: Highlight Date: 05/06/2016 20:26:06

 Number: 8 Author: ptd Subject: Highlight Date: 05/06/2016 20:25:59

 Number: 9 Author: ptd Subject: Highlight Date: 05/06/2016 20:26:20

 Number: 10 Author: ptd Subject: Highlight Date: 05/06/2016 20:26:28

 Number: 11 Author: ptd Subject: Highlight Date: 05/06/2016 20:26:32

The cross-sections for several processes are shown in Figure 2.3 and it can be seen that the cross-section for VBF Higgs production is approximately 1.5 pb. Therefore, we expect approximately 30000 [1]BF produced Higgs bosons in the 2012 dataset. By contrast the vector boson production cross-section is approximately 100 nb and the total cross-section for any process is orders of magnitude higher still. The separation of the relatively small number of signal events from the large background is a major challenge for the search for invisibly decaying Higgs bosons.

The large total cross-section combined with the high instantaneous luminosities that the LHC operates at leads to the probability for multiple proton-proton interactions per bunch crossing being high. The distribution of the number of interactions per bunch crossing, μ , can be seen in Figure 2.4. The additional interactions on top of the process of interest in a bunch crossing are called pile-up (PU).

2.2. The CMS experiment

The CMS detector was designed to search for the SM Higgs and new physics at the TeV energy scale. Both because the nature of new physics is not known and the SM Higgs has a wide range of decays and production mechanisms CMS must be sensitive to many different types of final state particles and topologies. In order to achieve this it has a hermetic design comprising a barrel, endcaps and a forward calorimetry system. It is composed of several layers of subdetectors each sensitive to different particles as shown in Figure 2.5. The hermiticity of the detector is particularly important for the VBF Higgs to invisible search. Further details on the CMS detector beyond those in this section can be found in Ref. [30].

A central design feature of CMS is the superconducting magnet, inside which is generated a [2]8T axial field. This field bends the path of charged particles travelling through it allowing their momentum to be measured. Not all particles are charged however, and the path of several types of particles through the CMS detector is shown in Figure 2.6. The first layer is the tracker which records the paths taken by charged particles, as [3]well as providing a momentum measurement the tracks also allow the vertex from which the particle came to be identified. The next layer is the ECAL where electrons and photons deposit energy through electromagnetic showers. This is followed by the HCAL where hadrons deposit most of their energy. After the calorimetry systems is the superconducting magnet which is not instrumented. Outside the magnet are the muon

 Number: 1 Author: ptd Subject: Highlight Date: 05/06/2016 20:28:09

VBF-produced

[needs to be hyphenated, as "VBF-produced" is an adjective modifier for "Higgs boson".]

 Number: 2 Author: ptd Subject: Highlight Date: 05/06/2016 20:28:36

3.8\T

 Number: 3 Author: ptd Subject: Inserted Text Date: 05/06/2016 20:35:08

particles. As

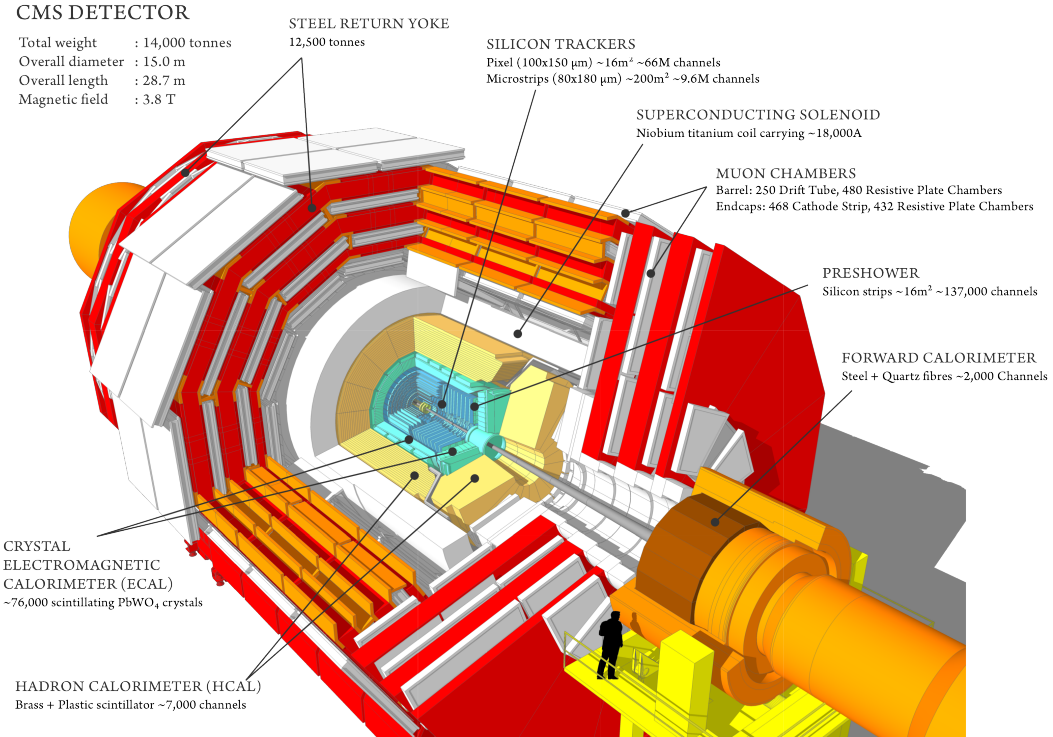


Figure 2.5.: A diagram of the subsystems making up the CMS detector, illustrating the hermeticity and layered structure of the experiment [63].

detection systems, which are interspersed with iron plates which form the return yoke for the magnet. Due to their high mass compared to electrons, muons do not deposit much energy in the detector and often are not stopped, so the muon system is primarily a tracking detector.

The origin of the co-ordinate system used by CMS is at the nominal interaction point. It is a right handed cartesian system with the x_1 axis pointing towards the centre of the LHC ring and the y_2 axis vertically upwards, the z_3 axis then points along the beam line. The azimuthal angle ϕ and the polar angle θ are measured in radians from the x_4 and z_5 axes respectively. It is common to describe the direction of outgoing particles using ϕ and their pseudo-rapidity, η which is defined as:

$$\eta = -\ln[\tan(\theta/2)]. \quad (2.3)$$

Distances in the $\eta - \phi$ plane are given by $\Delta R = \sqrt{\Delta\phi^2 + \Delta\eta^2}$. Two other quantities often used at hadron colliders are the projections of a particle's momentum and energy in the transverse plane, these are denoted as p_T and E_T respectively. The missing transverse energy, defined as the negative vector sum of the momentum in the transverse plane of

Page: 30

 Number: 1 Author: ptd Subject: Inserted Text Date: 05/06/2016 20:35:48
\$x\$

 Number: 2 Author: ptd Subject: Inserted Text Date: 05/06/2016 20:36:01
\$y\$

 Number: 3 Author: ptd Subject: Inserted Text Date: 05/06/2016 20:36:13
\$z\$

 Number: 4 Author: ptd Subject: Inserted Text Date: 05/06/2016 20:36:25
\$x\$

 Number: 5 Author: ptd Subject: Inserted Text Date: 05/06/2016 20:36:34
\$z\$

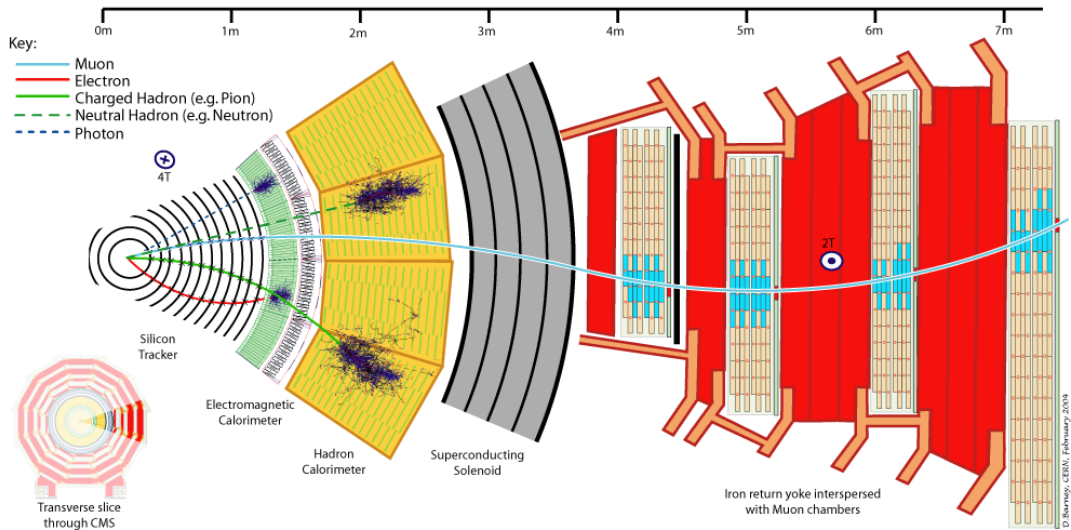


Figure 2.6.: A schematic cross-section of the CMS experiment showing the path taken by several types of particles [64].

all particles in an event, is important in inferring the presence of invisible particles and is denoted \cancel{E}_T . Also, when describing an event the terms **[1]ading** and **[2]b-leading** refer to the highest and second-highest p_T objects in an event respectively.

2.2.1. Tracker

The tracker is designed to measure the paths of charged particles precisely from LHC collisions which curve in CMS's magnetic field. The design transverse momentum resolution of the full tracking detector is 1-2% at 100 GeV. In order to measure the particles' positions precisely and ensure the occupancy of the tracker is low a high granularity is required. Due to the frequency of collisions at the LHC and the high instantaneous luminosity a radiation hard system with fast response is also necessary. This combination of requirements motivates the use of a **[3]ilicon based** system. When traversing silicon charged particles create electron-hole pairs, which are then separated by an applied electric field, causing a current pulse.

The tracker layout can be seen in Figure 2.7. In order to keep the sensor occupancy below 1% at design luminosity, the innermost component is a silicon pixel detector. This detector has three layers in the barrel, at radii of 4.7, 7.3 and 10.2 cm, and two in the endcap. There are 66 million pixels each $100_{[5]}^{[4]} 150_{[6]}$ in size. The resulting resolution of the pixel detector is approximately $10_{[7]}$ in the $r - \phi$ plane and $17_{[8]}$ in the $r - z$

Page: 31

T Number: 1 Author: ptd Subject: Highlight Date: 05/06/2016 20:40:06
"leading" [insert quotation marks]

T Number: 2 Author: ptd Subject: Highlight Date: 05/06/2016 20:40:25
"sub-leading"

T Number: 3 Author: ptd Subject: Highlight Date: 05/06/2016 20:40:50
silicon-based

T Number: 4 Author: ptd Subject: Highlight Date: 05/06/2016 20:41:42
\$\times\$

T Number: 5 Author: ptd Subject: Inserted Text Date: 05/06/2016 20:41:25
\

T Number: 6 Author: ptd Subject: Inserted Text Date: 05/06/2016 20:41:50
\

T Number: 7 Author: ptd Subject: Inserted Text Date: 05/06/2016 20:42:05
\

T Number: 8 Author: ptd Subject: Inserted Text Date: 05/06/2016 20:42:13
\

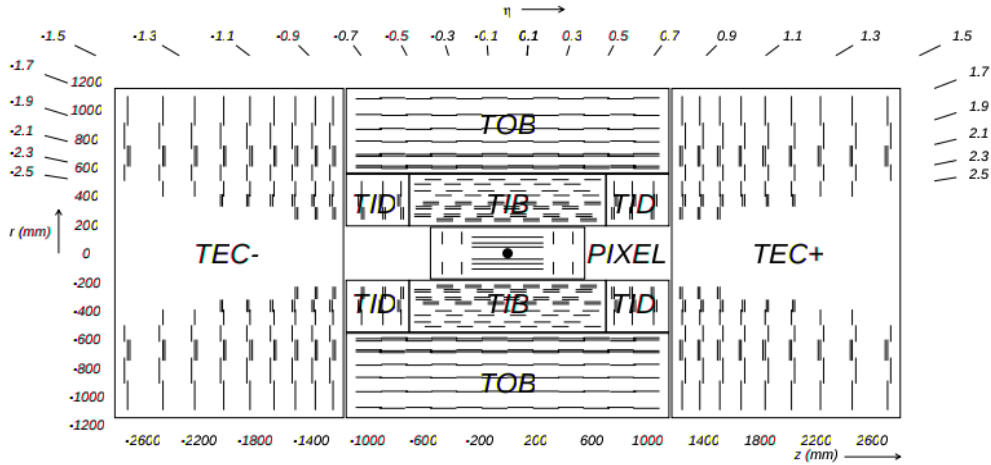


Figure 2.7.: A cross-section of the CMS tracker, indicating the subsystems that comprise it. Each line indicates a detector module [30] and the labels for each subsection are the names given by CMS to the various subsections of the tracker.

plane [65]. During run 1 the proportion of modules in the pixel (strip) tracker known to be defective was 2.4% (2.3%) [66].

Surrounding the pixel detector is a silicon strip detector with 10 layers in the barrel, at radii of 20 to 116 cm, and 12 pairs of disks in the endcap. The strips are typically 10-20 cm long and 80-180₁₂ wide, with the strip size increasing with radius as the particle flux decreases. The strip detector's single point resolution is 230-530₁₃ in the $r-z$ plane and 23-52₁₄ in the $r-\phi$ plane. The better resolution in the $r-\phi$ plane allows p_T to be measured with higher precision, as this is the direction in which a particle's track bends in the CMS magnetic field. The barrel and endcap detectors together have an acceptance of $|\eta| < 2.5$ for both the pixel and strip detectors. Further details on the position resolution of the tracking detector for vertex reconstruction will be given in Section 3.2.

2.2.2. Electromagnetic calorimeter

The ECAL is designed to provide accurate photon and electron reconstruction and precise measurement of the electromagnetic component of hadron jets. It is a homogeneous calorimeter made of lead tungstate (PbWO_4) crystals, separated into a barrel section, with 61200 crystals and two endcaps each with 7234 crystals. These crystals are 25.8 radiation lengths in depth in the barrel and instrumented with 5 photodetectors, avalanche photodiodes 6 being used in the barrel and vacuum phototriodes in the endcap 7

Page: 32

 Number: 1 Author: ptd Subject: Inserted Text Date: 05/06/2016 20:43:30
Run

 Number: 2 Author: ptd Subject: Inserted Text Date: 05/06/2016 20:42:30
\

 Number: 3 Author: ptd Subject: Inserted Text Date: 05/06/2016 20:42:39
\

 Number: 4 Author: ptd Subject: Inserted Text Date: 05/06/2016 20:42:50
\

 Number: 5 Author: ptd Subject: Highlight Date: 05/06/2016 20:44:40
photodetectors (avalanche)

 Number: 6 Author: ptd Subject: Cross-Out Date: 05/06/2016 20:44:51

 Number: 7 Author: ptd Subject: Inserted Text Date: 05/06/2016 20:45:33
endcaps)

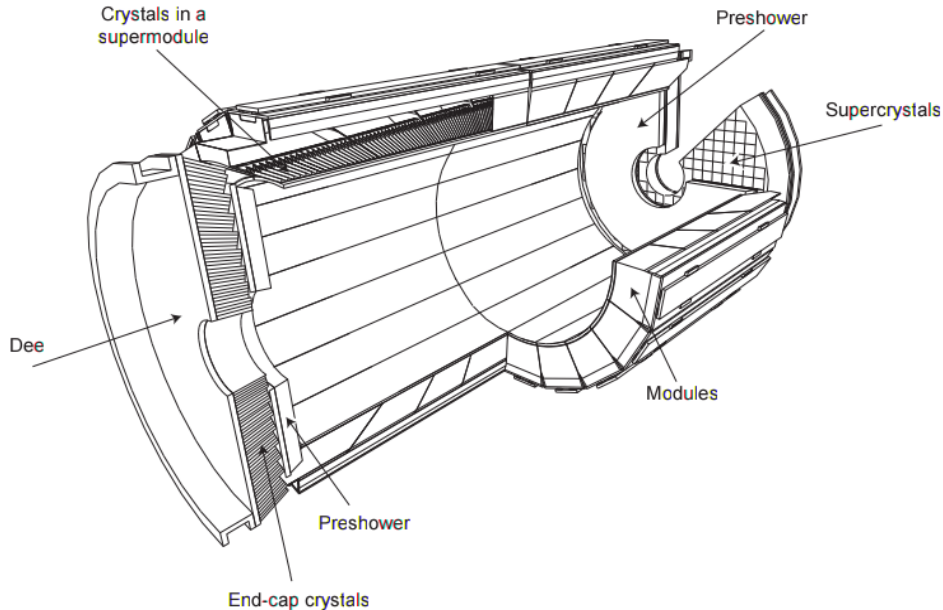


Figure 2.8.: A schematic of the CMS ECAL, indicating the subsystems that comprise it. The ECAL is **1.8m** long by **2.5m** wide [30].

The layout of the ECAL is shown in Figure 2.8. The ECAL barrel (EB) crystals have a 170×30 arrangement in $\eta - \phi$ space such that the gaps between crystals are offset by 3° from the vector to the detector origin, thus avoiding particles travelling through the gaps. The EB extends to $|\eta| = 1.479$, with higher values of η covered by the ECAL endcaps (EE). The crystals in the EE are arranged in an $x - y$ grid pointing at a focus **4.3m** from the nominal interaction point, giving a $5 - 8^\circ$ separation between the gaps between crystals and the vector to the detector origin. In addition to the main PbWO_4 detector the endcaps also have a preshower detector. This preshower is a lead silicon strip sampling calorimeter, which initiates the electromagnetic showers and provides sufficient position resolution to distinguish single photons from pairs produced in neutral pion decays. The total acceptance of the barrel and endcap detectors is $|\eta| < 3.0$.

On entering the ECAL high energy electrons or photons initiate an electromagnetic shower by undergoing Bremsstrahlung or pair production respectively. The resulting cascade of particles continues to lose energy by successive Bremsstrahlung and pair production until their energy is low enough that the photons no longer undergo pair-production and the electrons lose their energy mainly by ionisation. The excitation of the PbWO_4 crystals leads to the emission of scintillation light, proportional to the amount of energy deposited, which is collected by the photodetectors.

Page: 33

 Number: 1 Author: ptd Subject: Highlight Date: 05/06/2016 20:48:08

\ [insert half-space]

 Number: 2 Author: ptd Subject: Highlight Date: 05/06/2016 20:48:27

 Number: 3 Author: ptd Subject: Inserted Text Date: 05/06/2016 20:46:52

\$\times\$

 Number: 4 Author: ptd Subject: Highlight Date: 05/06/2016 20:51:10

 Number: 5 Author: ptd Subject: Highlight Date: 05/06/2016 20:50:39

2^{circ}

The choice of PbWO₄ is motivated by its high density (8.28 g/cm³), short radiation length (0.89 cm), small Moli  re radius [1.2cm] and radiation hardness. These properties lead to the showers being contained in a small area and allows the calorimeter to be compact and have fine granularity. Another advantage of PbWO₄ is that 80% of the scintillation light is emitted within the LHC's [25ns] design [3unch crossing] time, so particles can be properly associated with the [4unch crossing] from which they originate.

For particle energies below 500 GeV, where the resulting shower ceases to be contained in the full depth of the ECAL, the ECAL resolution can be parameterised as:

$$\left(\frac{\sigma}{E}\right)^2 = \left(\frac{S}{\sqrt{E}}\right)^2 + \left(\frac{N}{E}\right)^2 + C^2. \quad (2.4)$$

Where S is the stochastic term, N the noise term and C the constant term. The stochastic term is comprised of fluctuations in the lateral containment of showers and also in the amount of scintillation light. The noise term is made up of electronic and digital noise, and signals from other bunch crossings which do not fully dissipate in time. The constant term comes from non-uniformity of light collection along the crystals, errors in the calibration of crystals against each other and leakage of energy from the back of the calorimeter. The energy resolution was measured without an applied magnetic field in an electron beam using particles with momenta between 20 and 250 GeV. The stochastic, noise and constant terms were found to be 0.028 GeV^{1/2}, 0.12 GeV and 0.003 respectively.

As the ECAL is exposed to radiation the PbWO₄ crystals darken and as a result fewer photons are collected per unit energy deposited. The loss of response due to this darkening at the end of Run I varies from 6% for crystals in the most central region of the ECAL to 30% in the endcaps [67].

2.2.3. Hadronic calorimeter

The HCAL is designed to measure the energy of strongly interacting particles. This measurement is particularly important for neutral hadrons which do not leave tracks in the tracking system and deposit most of their energy in the HCAL, and for the determination of \cancel{E}_T . The main part of the HCAL consists of a brass and scintillator plus wavelength shifting fibre sampling calorimeter split into hadron barrel (HB) and hadron endcaps (HE) sections. The primary design consideration for the HCAL is that it must fit between the outer edge of the ECAL ($r = 1.77$ m) and the inner edge of

Page: 34

 Number: 1 Author: ptd Subject: Highlight Date: 05/06/2016 20:51:41

 Number: 2 Author: ptd Subject: Highlight Date: 05/06/2016 20:51:48

 Number: 3 Author: ptd Subject: Highlight Date: 05/06/2016 20:52:27
bunch-crossing

 Number: 4 Author: ptd Subject: Highlight Date: 05/06/2016 20:52:52
bunch-crossing

 Number: 5 Author: ptd Subject: Inserted Text Date: 05/06/2016 20:54:06
for which

 Number: 6 Author: ptd Subject: Inserted Text Date: 05/06/2016 20:54:34
showers are

the magnet ($r = 2.95$ m). In order to satisfy this requirement and achieve satisfactory containment of hadronic showers the magnet coil is also used as an absorber, and there is a further layer of scintillator outside the magnet coil (hadron outer (HO)). The barrel and endcap detectors extend to $|\eta| < 3$.

Brass is chosen as the main HCAL absorber because it is not magnetic and has a relatively short nuclear interaction length of 16.42 cm. Once showers have been initiated in the absorber layers they then pass through the plastic scintillator tiles, where they create pulses of light. These pulses are transferred via wavelength shifting fibres to hybrid photodiodes. The segmentation of the scintillator is such that the $\eta - \phi$ resolution in the HB (HE) is 0.087×0.087 (between 0.087×0.087 and 0.17×0.17 depending on η).

In addition to the barrel and endcap sections of the HCAL there is also a steel and quartz fibre Cherenkov forward calorimeter (hadron forward (HF)), which extends the calorimetry coverage of CMS to $|\eta| < 5.2$. The choice of this technology is driven by its ability to withstand the very high particle fluxes present so close to the beamline. Showers are initiated by the steel absorber and signals are generated in the quartz fibres by particles above the Cherenkov threshold generating Cherenkov light, which is collected by photomultiplier tubes. Due to the Cherenkov energy threshold increasing with particle mass the HF is primarily sensitive to the electromagnetic component of showers.

A diagram of the HCAL layout can be seen in Figure 2.9. In total the HCAL corresponds to 10-15 interaction lengths, depending on η . The resolution of the barrel and endcap sections of the HCAL as a function of the incident particle energy was measured in a pion beam and has been found to be well parameterised by:

$$\left(\frac{\sigma}{E}\right)^2 = \left(\frac{94.3\%}{\sqrt{E}}\right)^2 + (8.4\%)^2 [68]. \quad (2.5)$$

2.2.4. Muon system

As described above muons are highly penetrating, and thus are only rarely contained by the inner detector. Very few other charged particles are able to leave the calorimeters^[1]_[2] so the presence of tracks in the muon system is sufficient to identify muons. The muon tracking system uses three types of gaseous particle detectors, located throughout the iron magnet return yoke. In all three types of detector when a charged particle travels through the gaseous detector it ionises the gas, the resulting free electrons then drift

Page: 35

 Number: 1 Author: ptd Subject: Inserted Text Date: 09/06/2016 23:45:15
traverse

 Number: 2 Author: ptd Subject: Inserted Text Date: 09/06/2016 23:45:28
without being absorbed

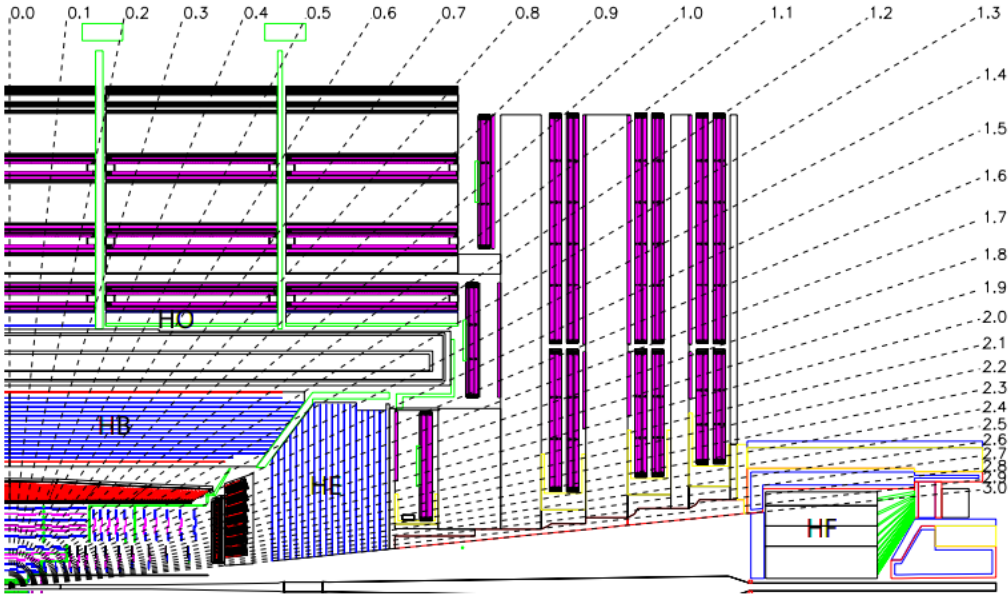


Figure 2.9.: A schematic of a quadrant of the CMS HCAL in the $r - z$ plane, indicating the subsystems that comprise it [30].

towards the detector's anode resulting in an electrical signal. The two primary types of detectors used are the drift tube (DT), which is used in the barrel section of the detector ($|\eta| < 1.2$), and the cathode strip chamber (CSC), which is used in the endcap ($0.9 < |\eta| < 2.4$). The DT and CSC systems identify muons and provide measurements of their momentum. These measurements can be combined with those from the tracker to improve the muon momentum resolution. This combined reconstruction and momentum measurement along with its resolution is described in Section 3.5. Additionally there is a resistive plate chamber (RPC) system in both the barrel and endcap regions ($|\eta| < 1.6$), the primary purpose of which is to provide trigger and **[l]aunch crossing** identification information. A diagram of the CMS muon system can be found in Figure 2.10.

Each system has its own particular advantages and disadvantages which make it best suited for use in the various parts of the muon system. DTs are inexpensive and reliable, but they are not usable in regions with high muon and neutron background rates, making them well suited to the barrel portion of the detector, where large areas must be instrumented and rates are low. Each DT is a 2m long wire in a $13 \times 43\text{mm}^2$ tube. The length is limited by the segmentation of the iron return yoke, and the cross-section by the requirement that the occupancy and drift time are low enough to prevent multiple muon hits being read out at the same time. The DTs are organised in 4 stations, interspersed with return yoke iron plates. The first three stations have 8 chambers each, 4 to measure

Page: 36

 Number: 1 Author: ptd Subject: Highlight Date: 09/06/2016 23:46:05
[hyphenate]

 Number: 2 Author: ptd Subject: Highlight Date: 09/06/2016 23:46:20

 Number: 3 Author: ptd Subject: Highlight Date: 09/06/2016 23:46:24

the muon’s position in the $r - \phi$ plane and 4 to measure the z co-ordinate. The final outermost layer does not have the z -measuring chambers. These chambers consist of 8-12 stacked DTs, with each layer offset from the previous one by half the width of a tube to avoid gaps.

Due to their fast response time, fine segmentation and radiation resistance CSCs are ideal for the endcap region where the muon and background rates are higher. Each CSC is a multiwire proportional chamber with 7 planes of cathode strips running radially outwards with 6 planes of anode wires, which run azimuthally, interleaved between them. Both the anode and cathode wires are read out to provide η and $r - \phi$ co-ordinate measurements respectively. Similarly to the DT system the design number of CSC stations in each endcap is 4 interspersed with iron return yoke plates. During Run 1 only three of the CSC stations were present, the fourth station in each endcap was added during the long shutdown and is present for Run 2. The position resolution in the $r - \phi$ plane of the CSCs varies from 75-83 μm.

The RPCs are gas gaps surrounded by anode and cathode plates with read out strips between them. The advantage of RPCs is that their response is good at high rates, and they have very good time resolution, making them ideal for use in the trigger and assignment of muons to a bunch crossing. However, they have much poorer position resolution than the DTs or CSCs. There are 6 layers of RPCs in the barrel and 3 in the endcap.

2.2.5. Trigger system

The design bunch crossing rate of the LHC is 40 MHz, and for the data used in this thesis it varied from 20-40 Hz. Since each event consists of approximately 1 MB of data, writing every event to tape would correspond to a data rate of 20-40 TB/s which is not feasible. It is also not feasible for the detector electronics to read out the detector at this frequency. It is therefore necessary to use a trigger system to perform an “online” reconstruction and reduce the event rate by selecting only the most interesting events.

The trigger is separated into two stages, the L1 trigger and the HLT. First the L1 trigger, which is built of custom-designed electronics, reduces the rate to a maximum of 100 kHz. The decision to accept an event in the L1 trigger or not starts with local information on the energy deposits in the calorimeters and hits in the muon systems, which is stored for all events for 128 bunch crossings. A decision must therefore be made within 128 bunch

Page: 37

 Number: 1 Author: ptd Subject: Inserted Text Date: 09/06/2016 23:47:07
1

 Number: 2 Author: ptd Subject: Inserted Text Date: 09/06/2016 23:47:31
; [comma splice]

 Number: 3 Author: ptd Subject: Highlight Date: 09/06/2016 23:47:55

 Number: 4 Author: ptd Subject: Inserted Text Date: 09/06/2016 23:48:28
was either 20 or 40

 Number: 5 Author: ptd Subject: Highlight Date: 09/06/2016 23:49:22
High Level Trigger (HLT)

[need to spell out any acronyms prior to first use]

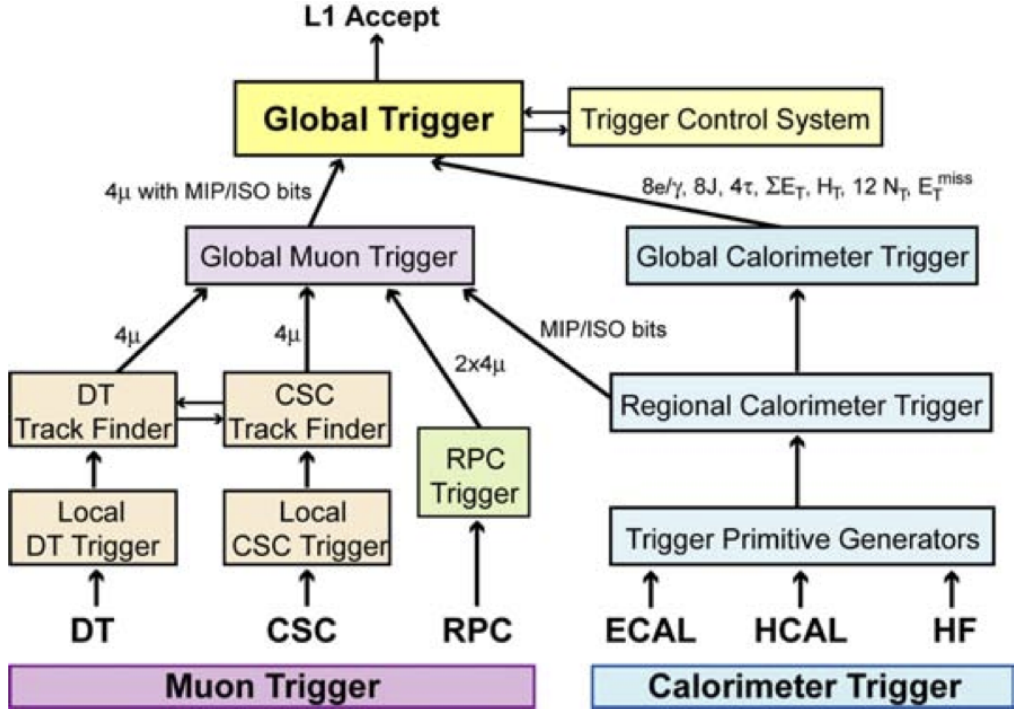


Figure 2.11.: A schematic of the L1 trigger system. The arrows indicate the flow of data, the information transferred between systems is also indicated [30].

crossings or the event is discarded. Due to the limited time available and the limited available bandwidth of the data acquisition system, this information is generally not available at the detector's full resolution. After it is collected from the detector the local information is then passed to the regional trigger systems, which generate lists of trigger candidates, such as electrons or jets, ranked by energy and quality. These ranked lists from each region are then passed to the global muon and calorimeter system triggers, which select the highest ranked candidates across the whole detector and give them to the global trigger, which makes a final decision. This process is shown in Figure 2.11.

If an event is accepted by the L1 trigger the full detector information is read out to the HLT farm on the surface, which reduces the rate further still to approximately 1 kHz. The HLT consists of several thousand commercially available CPUs. Despite having the full detector information, the time available does not allow for the full offline reconstruction to be performed. ~~Never the less,~~ [1] the algorithms available at the HLT are much closer to those used offline than those available at L1, allowing the trigger to better select events that would also pass requirements on the offline quantities. If they are accepted

 Number: 1 Author: ptd Subject: Inserted Text Date: 09/06/2016 23:53:51
Nevertheless

hits the track with the best fit, i.e. that having the lowest χ^2 , is kept. This process of reconstructing tracks starting from seeds is repeated up to six times, with hits associated to a successfully reconstructed track removed for the next iteration.

After the full set of iterations is complete the tracks are refitted again using another Kalman filter, initialised with the innermost hit on the track and proceeding to iteratively add the hits on the track from inside to outside. This refitting aims to reduce biases from the track’s seed including those introduced for **[1]vo hit** seeds that include constraints from the beamspot. The refitted tracks are then smoothed by another Kalman filter, which is initialised with the current **[2]est fit** track hypothesis and iterates from the outside of the detector inwards.

The smoothed tracks then have quality criteria, such as a requirement on the maximum number of layers the track traverses without leaving a hit, imposed to reject fake tracks. The efficiency of the CTF is estimated in data using tracks from muons from Z decays, and is found to be greater than 99% for muons with $1 < p_T < 100$ GeV. For muons with $p_T = 100$ GeV the p_T resolution of the CTF is found to be approximately 2.8% [71].

3.2. Primary vertex

The very high instantaneous luminosities present at the LHC lead to a large probability of multiple proton-proton interactions occurring in each bunch crossing. It is therefore essential to identify the Primary vertex (PV), which relates to the highest energy interaction or “hard scatter”. It is also useful to identify the PV to distinguish “prompt” particles directly from the hard scatter from those resulting from processes which occur later such as heavy flavour hadron decay or photon conversion.

The CMS PV reconstruction algorithm has three steps **[3]** track selection, clustering of tracks into vertices and finally fitting the position of these vertices and is described in more detail in Ref. [71]. In the first step, track selection, the subset of tracks with non-significant transverse impact parameters is chosen. This selection removes tracks not coming from the primary interaction region.

The next step of clustering tracks into prototype vertices uses a “deterministic annealing” (DA) algorithm [72]. These prototype vertices then have their position determined by an adaptive vertex fitter [73]. This fitter starts by performing a fit to the position of the vertex, then assigning weights, w_i to each track according to the probability that it

Page: 42

 Number: 1 Author: ptd Subject: Highlight Date: 09/06/2016 22:14:23
[hyphenate]

 Number: 2 Author: ptd Subject: Highlight Date: 09/06/2016 22:14:42
[hyphenate]

 Number: 3 Author: ptd Subject: Inserted Text Date: 09/06/2016 22:15:30
:

belongs to the vertex, before repeating the process iteratively. Both of these algorithms also use the concept of “cooling,” where the algorithm is performed repeatedly as a temperature parameter, which controls the size of fluctuations around the current state of the system, is gradually reduced, to increase the chance of finding the global best fit solution.

The number of degrees of freedom of the resulting vertex is defined as:

$$n_{dof} = 2 \sum_{i=1}^{\#tracks} w_i - 3. \quad (3.1)$$

This variable is highly correlated with the number of tracks compatible with the vertex and can therefore be used to select vertices coming from true proton-proton interactions.

The PV is defined to be the vertex with the highest sum of the squared p_T of all the tracks contributing to it. If there is no reconstructed vertex the nominal beam crossing point is used. In the analyses described in this thesis events are required to have a real vertex, which has $n_{dof} > 4$ and a maximum displacement in the z -direction (xy -plane) direction from the centre of the detector of 24 cm (2 cm).

The performance of the vertex reconstruction algorithm has been measured using events with at least one jet with $p_T > 20$ GeV [71]. The efficiency to reconstruct at least one primary vertex in these events is found to be greater than 99% for vertices with at least three tracks. The position resolution is found to vary as a function of the number of tracks associated to the vertex, being approximately $100\mu\text{m}$ for vertices with 5 tracks and approaching $10\mu\text{m}$ for vertices with greater than 50 tracks.

3.3. Particle flow

Particle flow (PF) is an algorithm used by CMS to combine information from different sub-detectors into individual particles [74–76]. This approach is particularly beneficial for CMS as it allows the accurate momentum measurements of the inner tracker, and the excellent energy measurements and granularity of the ECAL to be combined and used to improve the energy measurement of objects seen in the HCAL. The PF approach also allows calibrations specific to charged and neutral hadrons to be applied. The PF algorithm classifies particles as charged hadrons, neutral hadrons, photons, muons and electrons. This set of particles, referred to as PF candidates, can then further be used

Page: 43

 Number: 1 Author: ptd Subject: Inserted Text Date: 09/06/2016 22:16:42
[insert half-space]

 Number: 2 Author: ptd Subject: Inserted Text Date: 09/06/2016 22:16:49
[insert half-space]

 Number: 3 Author: ptd Subject: Inserted Text Date: 09/06/2016 22:17:04
[insert space]

to calculate the \cancel{E}_T , as input to the jet reconstruction, for reconstructing taus and to calculate the isolation of leptons.

The PF algorithm starts with tracks, reconstructed as described in Section 3.1, and calorimeter clusters, which are reconstructed separately in each sub-detector of the calorimeter system. Clustering starts with seeds, which are the calorimeter cells which have the local maximum energy which is also more than twice the expected calorimeter noise, which is 80 (300) MeV in the EB (EE) and 800 MeV in the HCAL. Cells adjacent to the cluster are added if they also have energy more than twice the expected calorimeter noise. Cluster-track pairs whose cluster position and track trajectory are compatible are then linked together to identify charged particles. Linking between tracks from the inner tracker and the muon system is also performed to identify muons. The information from tracks with associated ECAL clusters, i.e. those compatible with electrons, is further used to search for clusters compatible with having come from Bremsstrahlung photons from the electron. This is described further in Section 3.4.

Once electrons, muons and charged hadrons have been identified, further calorimeter clusters are identified as neutral hadrons or photons if they are in the HCAL or ECAL respectively. Excess energy in a calorimeter cluster compared to that expected from the associated tracks also allows the presence of neutral particles that would otherwise not have been identified to be determined.

3.4. Electrons

As described in Section 3.3, electrons are reconstructed by matching ECAL deposits with tracks from the inner tracker. This process is complicated by the fact that electrons can lose significant amounts of energy, in the form of Bremsstrahlung photons, as they traverse the inner tracker. Approximately 35% of electrons lose at least 70% of their initial energy in this way [77]. The Bremsstrahlung photons often convert to electron-positron pairs which are then further spread in the ϕ direction by CMS’s solenoidal magnetic field. The electron reconstruction, which is described in detail in Ref. [78], employs so-called “supercluster” algorithms to combine ECAL deposits from both the initial electron and the Bremsstrahlung photons.

Due to their different geometries, different supercluster algorithms are used in the barrel and endcaps. In the barrel the “hybrid” clustering algorithm is used, this begins with a seed crystal which is the crystal with local maximum energy greater than 1 GeV. Arrays

Page: 44

[T] Number: 1 Author: ptd Subject: Inserted Text Date: 09/06/2016 22:17:53
)

[T] Number: 2 Author: ptd Subject: Inserted Text Date: 09/06/2016 22:18:12
[insert space]

[T] Number: 3 Author: ptd Subject: Inserted Text Date: 09/06/2016 22:18:47
;

[T] Number: 4 Author: ptd Subject: Inserted Text Date: 09/06/2016 22:19:32
:

of 5×1 crystals in $\eta \times \phi$ are then added around the seed crystal if they are within 17 crystals of it in either direction in ϕ and have energy greater than 0.1 GeV. Contiguous arrays are grouped into clusters. The final supercluster consists of all clusters from a seed with cluster energy greater than 0.35 GeV.

In the endcap the “multi- 5×5 ” algorithm is used. This algorithm also starts with seed crystals, in this case those with energy higher than their four direct neighbours and also greater than 0.18 GeV. Clusters are then made up of the 5×5 square of crystals centered on the seed. Individual clusters whose seeds are within 0.07 in η and 0.3 in ϕ of each other are grouped and kept as a supercluster if their total energy is greater than 1 GeV. A reference position for the supercluster is taken to be the energy-weighted average position of all the clusters belonging to it, and the maximum difference in ϕ between any cluster and the reference position is taken to be the size of the cluster in ϕ . The individual clusters in a supercluster are then extrapolated to the preshower detector. Any preshower deposits within the supercluster’s ϕ size plus 0.15 in ϕ and within 0.15 in η of a cluster in the supercluster are added to it.

The energy-weighted average position and energy of the final supercluster are then used to extrapolate the electron’s track back to the innermost layers of the tracker for both electron charge hypotheses. This extrapolation is then matched to hits within a $\phi - z$ window of it, whose size is determined by the uncertainties on the ϕ position of the supercluster and the z position of the beamspot. This size was typically 5 cm in 2012. This matched hit is used to update the estimated electron trajectory so that a hit in the second layer of the inner tracker can be searched for in a much narrower window. Hits in both the first and second layers compatible with a supercluster are then used as seeds for dedicated electron track reconstruction, performed using a Gaussian sum filter (GSF) algorithm [79], which performs better than a Kalman Filter for tracks with significant energy loss.

Electron identification criteria are applied to reject fake electrons caused by other particles such as pions. The variables used include:

- $\Delta\eta_{in}$ and $\Delta\phi_{in}$, which are the η and ϕ distances between the electron track position extrapolated to the ECAL and the supercluster position.
- $\sigma_{in\eta}$, the energy-weighted η width of the cluster.
- H/E , the ratio between the energy deposited in the HCAL and in the ECAL in the region of the electron’s seed cluster.

All of these variables are generally lower for real prompt electrons.

~~We also require the [1]electrons [2]be isolated, i.e. have a low amount of other activity present around them in the detector. The variable used for this requirement is the effective area corrected PF isolation, I_{PF} . In Run 1 it was defined as the sum of the p_T of the PF candidates within a cone of $\Delta R < 0.4$ around the direction of the electron, minus the expected contribution from PU across the area of the electron.~~

In the VBF invisible Higgs boson decay searches described later in this thesis two sets of requirements on the above variables are used to identify electrons, both of which require that $|\eta| < 2.4$. The “veto” set of identification criteria is looser and is used to veto events containing electrons. The other “tight” set of criteria is stricter and is used ~~[3]hen we want~~ to study events containing electrons. Tight electrons are required to be separated by more than 0.3 in ΔR from any veto muons to remove fake electrons from muons. The veto (tight) criteria have an efficiency of 93% (85%) for reconstructing central electrons with $p_T > 50$ GeV [80]. The veto (tight) electrons used in the analyses described in this thesis are required to have $p_T > 10(20)$ GeV unless stated otherwise.

3.5. Muons

Due to their relatively high mass and lack of strong force interactions, most muons deposit very little energy in the CMS calorimeters and thus leave the detector after passing through the muon system. As described in Section 3.3, this means that muons can be reconstructed by searching for compatible tracks from the inner tracker and the muon system. The approach of requiring both inner tracker and muon system tracks greatly improves the discrimination between muons and hadronic activity and is referred to as “global” muon reconstruction.

The CMS global muon reconstruction algorithm starts with each track in the muon system and searches for compatible tracks in the inner tracker [81]. If a compatible inner tracker track is found, a track fit, similar to that described in section Section 3.1, is performed using the hits in both the inner tracker and muon system. The fit accounts for energy losses as the muon traverses the detector. It is found that for muons with $p_T > 200$ GeV the global-muon fit is better than that from the tracker only [81]. However, due to the increased hadron discrimination described above all muons used for analyses in this thesis are required to have both inner tracker and muon system tracks. As with electrons it is also required that muons are isolated. The same isolation variable, I_{PF} ,

Page: 46

 Number: 1 Author: ptd Subject: Inserted Text Date: 09/06/2016 22:22:08
In addition,

[Do not use personal pronouns]

 Number: 2 Author: ptd Subject: Inserted Text Date: 09/06/2016 22:21:54
are also required

 Number: 3 Author: ptd Subject: Cross-Out Date: 09/06/2016 22:28:38

as described in Section 3.4 is used for muon isolation. Global muon reconstruction is sufficient for use in vetoing events containing muons, and muons passing the above reconstruction are referred to as “veto” muons.

Where we want to study events containing muons, further identification criteria are used. This is because whilst global muon reconstruction removes most hadrons, some so-called “punch through” hadrons, which are energetic enough to travel all the way through the CMS calorimeters, can still be reconstructed as muons. Furthermore, it is desirable to separate real but non-prompt muons from hadron decay, from prompt muons from the hard scatter or tau decay. The identification consists of requiring a high quality global muon track fit, that the muon’s track passes through at least ~~1~~² least 5 inner tracker layers, with at least one being a pixel layer, that the muon’s track includes at least two hits in the muon system, and that there is at least one muon system track segment present. Muons passing these additional requirements are referred to as “tight” muons. In addition to the above requirements both veto and tight muons are required to have $|\eta| < 2.1$.

The efficiency of veto (tight) muon reconstruction has been found to be 98-99% (96-98%) depending on the η of the muon, for muons with $p_T > 10 \text{ GeV}$ [81]. This efficiency measurement was performed using events with J/ψ or Z boson decays to muon pairs. The veto (tight) muons used in the analyses described in this thesis are required to have $p_T > 10(20) \text{ GeV}$ unless stated otherwise.

3.6. Jets

As it is a hadron collider, quarks and gluons are very common at the LHC. Furthermore, the presence of two final state quarks is one of the primary signatures of VBF Higgs production² which is one of the main focuses of this thesis. Ascertaining the momentum of these strongly interacting particles is therefore very important. As discussed in Section 1.2.1, the hadronisation of strongly interacting particles results in highly collimated jets of particles. The momentum of the original parton which gave rise to the jet can be reconstructed by combining all of the particles in the resulting jet.

 Number: 1 Author: ptd Subject: Cross-Out Date: 09/06/2016 22:29:42

 Number: 2 Author: ptd Subject: Inserted Text Date: 09/06/2016 22:29:56

,

3.6.1. Jet clustering

Jet clustering algorithms take the many different types of particles that are expected to be present in the particle showers from hadronisation, and combine them into jets [82]. It is important that jet clustering algorithms do not produce different reconstructed jets if a jet undergoes soft gluon radiation (called infrared unsafety) or if a gluon in it splits in two (called colinear unsafety). The algorithm used by CMS is a so-called sequential recombination algorithm. This class of algorithms requires a metric for calculating the distance between particles in the event, d_{ij} , and a metric for calculating the distance to a nominal beamline particle, d_{iB} to be defined. The algorithms then proceed as follows:

- 1 Calculate the distance between all pairs of particles in the event including the nominal beamline.
- 2 If the smallest distance is a d_{ij} combine i and j together into a single new particle particle_1 and return to step 1.
- 3 If the smallest distance is a d_{iB} , consider i to be a final state jet and remove it from the list of particles. Return to step 1.
- 4 Stop when no particles remain.

The particular algorithm used by CMS is the infrared and colinear safe anti- k_T algorithm [83]. Its distances are defined as:



$$d_{ij} = \min(p_{Ti}^{-2}, p_{Tj}^{-2}) \frac{\Delta R_{ij}^2}{R^2}, \quad (3.2)$$

$$d_{iB} = p_{Ti}^{-2}, \quad (3.3)$$

where ΔR_{ij} is the distance in the $\eta - \phi$ plane between particles i and j and R is a parameter of the algorithm analogous to the maximum radius of the jet. This algorithm starts by clustering around the hardest particle in a region and therefore usually produces circular jets, with easy to calculate areas.

The anti- k_T algorithm is implemented using the FASTJET package [84] with the PF candidates, described in Section 3.3, used as input, the output jets are referred to as PF jets. For analyses using data from LHC Run 1 R of 0.5 is used. In addition to these jets reconstructed from PF candidates, in MC events “generator” jets are also reconstructed by applying the anti- k_T algorithm, with the same radius as that used for the PF jets, to

Page: 48

 Number: 1 Author: ptd Subject: Inserted Text Date: 09/06/2016 22:31:08
(pseudo-)particle

 Number: 2 Author: ptd Subject: Inserted Text Date: 09/06/2016 22:47:41
; [comma splice]

 Number: 3 Author: ptd Subject: Sticky Note Date: 09/06/2016 22:46:29
[The notation in these two equations breaks the conventional notation you seem to use elsewhere. The subscript "T" should be consistently in upright roman script; the subscripts i and j should be consistently in italic mode; \Delta{R}, R and p should always be in math mode.]

 Number: 4 Author: ptd Subject: Inserted Text Date: 09/06/2016 22:48:28
cross-section

the final state particles produced by the generator before they are passed through the detector simulation.

3.6.2. Jet identification

In order to reject jets that are badly reconstructed or just due to detector noise, identification criteria are imposed on the jets reconstructed by the above algorithm. These requirements are that:

- The jet contains at least two PF candidates.
- The total jet energy contribution from neutral hadrons must be less than 99%.
- The total jet energy contribution from photons must be less than 99%.
- The jet has contributions from both the ECAL and HCAL.
- Jets with η such that tracking information is available must have at least one charged object which contributes to the jet's energy and less than 99% of their energy [1] from electrons.

Real jets from quarks or gluons pass these requirements with over 99% efficiency [85].

In addition to jets from detector noise, it is also possible for the jet reconstruction to include particles that are not from the PV, but instead come from PU vertices. This can lead either to an overestimation of the energy of a real jet from the PV, or to fake jets made up of energy from several vertices. The CMS pileup jet identification procedure [86] combines several variables sensitive to the pileup contribution in a jet, such as information on how the p_T of the jet is shared between its constituents and the constituents' tracking information, into a boosted decision tree (BDT) [87]. Simulated real jets from quarks pass this identification with 88-99% efficiency depending on how central they are, while jets from pile-up are rejected with 40-87% efficiency [86].

Jets are also required to have $\eta < 4.7$ so that they are fully contained within the CMS detector. Finally, jets which are within 0.5 in the $\eta - \phi$ plane of any veto electron, defined in Section 3.4, or veto muon, defined in Section 3.5, are vetoed, to avoid using jets which are due to misreconstructed leptons.

 Number: 1 Author: ptd Subject: Inserted Text Date: 09/06/2016 22:49:18
must be

3.6.3. Jet energy corrections

The energy of the jets clustered and identified by the CMS jet reconstruction often does not match the energy of the particle that initiated the jet. This can have many causes such as additional energy from PU, miscalibration of the energy response of the calorimeters or energy deposited in uninstrumented areas of the detector. To account for these mismatches a correction to the jet energy is applied that has the following functional form and is described in detail in Ref. [88]:

$$p_\mu^{\text{cor}} = C_{\text{offset}}(p_T^{\text{raw}}) \cdot C_{\text{rel}}(\eta) \cdot C_{\text{abs}}(p'_T) \cdot C_{\text{res}}(p''_T, \eta) \cdot p_\mu^{\text{raw}}. \quad (3.4)$$

Each C in the equation represents a correction, p_μ^{cor} is the corrected jet four-momentum, p_μ^{raw} is the jet four-momentum before correction, p'_T is the p_T after the offset and relative correction, C_{offset} , and p''_T is the p_T after all but the residual correction, C_{abs} .

The purpose of C_{offset} is to remove energy from the jet which is not due to activity from the PV such as detector noise and PU. The correction is calculated on a jet-by-jet basis by multiplying the median p_T density of the event in which the jet is by the jet's area.

The relative correction, C_{rel} , serves to make the jet energy response uniform in η . MC truth information and the dijet p_T balance method, where the p_T of a well measured jet in the central region of the detector is compared to a second jet at a different η in events with only two jets, C_{rel} data are used to calculate C_{rel} .

The absolute correction C_{abs} , makes the jet energy response uniform in p_T . As well as being calculated using MC truth information, the correction is also calculated by using $Z/\gamma+jets$ events, where the transverse momentum of the jets should balance the Z/γ . Both Z bosons that decay leptonically and photons have very good energy resolution, so any imbalances can be assumed to be due to jet mismeasurement.

Finally C_{res} , which is applied only to data and not MC, corrects for residual differences seen in both p_T and η response between data and MC. The total uncertainty on the overall jet energy correction is taken to be the sum in quadrature of the uncertainties on the individual corrections. The correction and its uncertainty are shown in Figure 3.1. The other two types of jets in the figure are not used in analyses described in this thesis and so are not discussed.

Page: 50

 Number: 1 Author: ptd Subject: Inserted Text Date: 09/06/2016 22:52:32
corrections (C_offset and C_rel)

 Number: 2 Author: ptd Subject: Inserted Text Date: 09/06/2016 22:53:18
correction (C_abs)

 Number: 3 Author: ptd Subject: Inserted Text Date: 09/06/2016 22:54:41
data

 Number: 4 Author: ptd Subject: Cross-Out Date: 09/06/2016 22:54:54

 Number: 5 Author: ptd Subject: Inserted Text Date: 09/06/2016 22:55:27
; [comma splice]

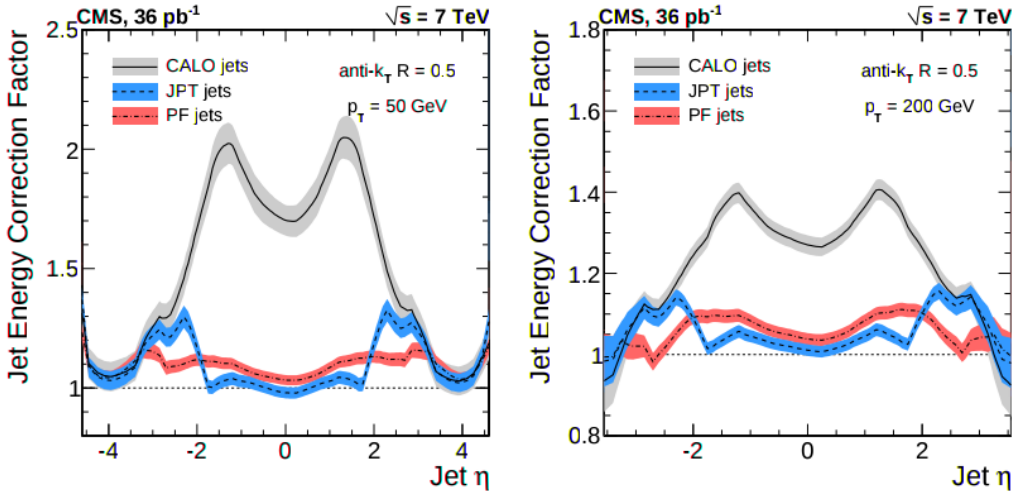


Figure 3.1.: Total jet-energy-correction factor as a function of jet η for jets with $p_T = 50 \text{ GeV}$ (left) and $p_T = 200 \text{ GeV}$ (right), for several types of jet reconstruction used at CMS. The bands indicate the corresponding uncertainty [88].

3.7. Missing transverse energy

Particles which interact only weakly with normal matter such as neutrinos and hypothetical particles will pass through the CMS detector without interacting. The only signature that they leave is a momentum imbalance between the visible particles in an event. The high hermeticity of the CMS detector allows this imbalance, the \cancel{E}_T , first described in Section 1.2.1, to be measured accurately. As the analyses described in this thesis are searches for invisibly decaying Higgs bosons, the measurement of \cancel{E}_T is crucial.

The CMS \cancel{E}_T reconstruction algorithm defines \cancel{E}_T as the negative vectorial sum of the p_T of all PF candidates [89]. For processes such as Z boson decays to muon pairs or $\gamma + \text{jets}$ there should be no \cancel{E}_T as all the decay products are visible. However, as can be seen from Figure 3.2, these events often still appear to have \cancel{E}_T due to the resolution of the p_T measurements of the various objects making up the PF candidates, primarily the jets which are numerous and do not have as good resolution as other objects.

The jet energy corrections, described in Section 3.6.3, alter the energy of jets, and in doing so alter the total energy present in the event. These changes are propagated to the \cancel{E}_T . Furthermore, as charged particle flow candidates can be determined to be from the PV or a PU vertex it is also possible to correct the \cancel{E}_T for PU contributions. This correction uses the ratio of the energy response of CMS for charged and neutral particles to estimate the neutral PU contribution from the charged PU contribution.

Page: 51

 Number: 1 Author: ptd Subject: Sticky Note Date: 09/06/2016 23:15:45

[Two commas missing - As it stands, this sentence implies that neutrinos and dark matter are examples of "normal matter", which I am sure is not what you meant... in fact very much the opposite.]

 Number: 2 Author: ptd Subject: Inserted Text Date: 09/06/2016 23:16:04

,

 Number: 3 Author: ptd Subject: Highlight Date: 09/06/2016 23:16:38

dark matter

 Number: 4 Author: ptd Subject: Inserted Text Date: 09/06/2016 23:16:18

,

 Number: 5 Author: ptd Subject: Cross-Out Date: 09/06/2016 23:18:29

 Number: 6 Author: ptd Subject: Highlight Date: 09/06/2016 23:20:13

[Unless if you mean Z decays to \gamma+jets as well (I don't think you do...), you need to insert two commas: "pairs, or \gamma+jets,"]

CMS uses a [1]adron plus strips (HPS) algorithm for reconstructing hadronic tau decays, described in detail in Ref. [91]. Almost all hadronic tau decay modes consist of one or three charged hadrons and up to two neutral pions [90]. The HPS algorithm aims to reconstruct both the charged hadrons and the photons which result from the neutral pion decays.

The HPS algorithm is seeded by a PF jet, described in Section 3.6, and starts by creating a [2]rip with the four-momentum of the most energetic electromagnetic (EM) PF candidate, i.e. photon or electron, in the jet. Other EM candidates are then searched for within a window of 0.05 (0.2) in η (ϕ) of the strip’s centre. The most energetic particle that is found is added to the strip and the four-momentum is updated. This process is repeated until no more particles are found, and if the strip has $p_T > 1 \text{ GeV}$ at this point it is kept. Combinations of charged hadrons and strips consistent with tau decay modes are then searched for, and if one is found the resulting combination is taken to be a hadronic tau.

Taus are required to be isolated. The isolation is calculated as the sum of all hadronic and photon PF candidates from the PV within a cone of size $\Delta R = 0.5$ of the tau. PF candidates not compatible with the PV within 0.8 in R of the tau are used to estimate and correct for the contribution to the isolation from PU.

Electrons which emit Bremsstrahlung photons can look very much like one charged hadron plus a neutral pion. A BDT is trained, using similar variables to those used for the electron identification in Section 3.4, to remove these particles. Taus that are consistent with being from a muon are also rejected. This rejection is performed by requiring that the tau is not reconstructed as a track compatible with hits in the muon system. The final efficiency of the CMS hadronic tau reconstruction for taus with $p_T > 20 \text{ GeV}$ is found to be 55%, with a fake rate of 2 (3)% for non-hadronic tau objects to be reconstructed as hadronic taus in the barrel (endcap) region of the detector.

3.9. MC weights

As discussed in Section 1.3 proton-proton collisions at the LHC are simulated using MC generators. In some cases the results of these simulations need to be modified to better match the observed data, by “weighting” the MC events. One example of this is cross-section weighting, where a weight is applied to account for the difference between the number of events generated and that expected to be observed in data for a given integrated luminosity. Further weights are applied to correct the generated distribution

Page: 53

T Number: 1 Author: ptd Subject: Highlight Date: 09/06/2016 23:22:11

While I can guess what you mean here, this is clearly CMS jargon, so at least insert quotes: "hadrons plus strips"

T Number: 2 Author: ptd Subject: Highlight Date: 09/06/2016 23:28:26

[You need to define what you mean by "strip" in this context; this is jargon, not unambiguous to a CMS-outsider... Is a strip a sequence of adjacent ECAL/HCAL cells in phi (or in eta)? Or is it simply a rectangular region demarcated in eta-phi space? or something else...?]

Chapter 4.

Search for invisibly decaying VBF produced Higgs bosons in Run 1 prompt data

As described in Chapter 1, searches for invisible Higgs boson decays are well motivated by their sensitivity to new physics, such as DM . Because $\mathcal{B}(H \rightarrow \text{inv})$ of an SM 125 GeV Higgs boson is very small, any evidence for invisible Higgs boson decays at the LHC would be evidence for physics beyond the SM. This chapter describes the search for invisible Higgs boson decays using data taken by CMS in 2012 which was promptly reconstructed. A dedicated trigger was developed specifically for this analysis. The total integrated luminosity collected with this trigger that was certified for use in physics analyses was 19.2 pb^{-1} [92]. The analysis was published in Ref. [1].

4.1. Event selection

Signal events are expected to have two jets with a characteristic VBF topology and a large amount of \cancel{E}_T . Several background processes, with significantly higher cross-sections than the signal process, can also produce events containing these objects. It is therefore necessary to design selection criteria, known as “cuts”, to remove as many of these background events from the analysis as possible, whilst retaining the maximum number of signal events.

The most significant of these background processes is the production of a vector boson in association with jets, “V+jets”. Leptonic decays of W bosons and Z boson decays to

Page: 55

 Number: 1 Author: ptd Subject: Highlight Date: 09/06/2016 23:29:18

 Number: 2 Author: ptd Subject: Highlight Date: 09/06/2016 23:29:38

neutrinos both produce \cancel{E}_T and, due to the approximately 1000 times higher cross-section for vector boson production than Higgs boson production, in many events the associated jets have a VBF-like topology [93]. V+jets backgrounds with a W (Z) are referred to as “W (Z)+jets”. A further background process that can produce significant numbers of VBF-like jets due to its very large cross-section is QCD production of multiple jets (“QCD multijets” or simply “QCD”). Whilst these multijet events have very little \cancel{E}_T from real invisible particles, it is possible for significant “fake” \cancel{E}_T to be caused by mismeasurement of the jets. The production of two vector bosons or top quarks can also lead to two jets and real \cancel{E}_T , although they have much lower cross-sections than the other background processes and their contribution is not as significant.

4.1.1. Trigger

The trigger requirements can be viewed as the first stage of the event selection. Their primary role is to reduce the rate of events that must be recorded by the detector, whilst retaining the maximum number of signal events. As described in Section 2.2.5, the decision whether to keep an event must be made very rapidly and, as a result, the object reconstruction algorithms used are less sophisticated, and the granularity of the information available from the CMS subdetectors is worse than those offline. The trigger criteria have therefore been chosen to be as loose as possible whilst achieving the required rate reduction.

As it is the key variable which indicates the presence of invisible particles, all events passing the trigger are required to have significant \cancel{E}_T . To pass the L1 trigger selection events are required to have $\cancel{E}_T > 40$ GeV. The HLT selection also requires that events have $\cancel{E}_T^{\text{no-}\mu} > 65$ GeV. The use of $\cancel{E}_T^{\text{no-}\mu}$ at trigger level ensures that events that are needed for the control regions used in the background estimation techniques described in Section 4.2 are not rejected. In addition to this $\cancel{E}_T^{\text{no-}\mu}$ requirement events must have at least one pair of jets [1] the event which is VBF-like to pass the HLT selection. The VBF-like requirements on the jets consist of requiring their η separation, $\Delta\eta_{jj}$, [2] greater than 3.5, that they are in opposite forward/backward halves of the detector and that they have high invariant mass, $M_{jj} > 800$ GeV. All of these jet requirements are motivated by the lack of colour connection between VBF events leading to large angular separations between the two jets, as described in Section 1.2.1. Not requiring that the VBF-like pair of jets also be the two highest p_T jets reduces inefficiencies caused by different p_T orderings in jets reconstructed by the trigger and by the offline reconstruction.

Page: 56

 Number: 1 Author: ptd Subject: Cross-Out Date: 09/06/2016 23:30:23

 Number: 2 Author: ptd Subject: Inserted Text Date: 09/06/2016 23:30:44
to

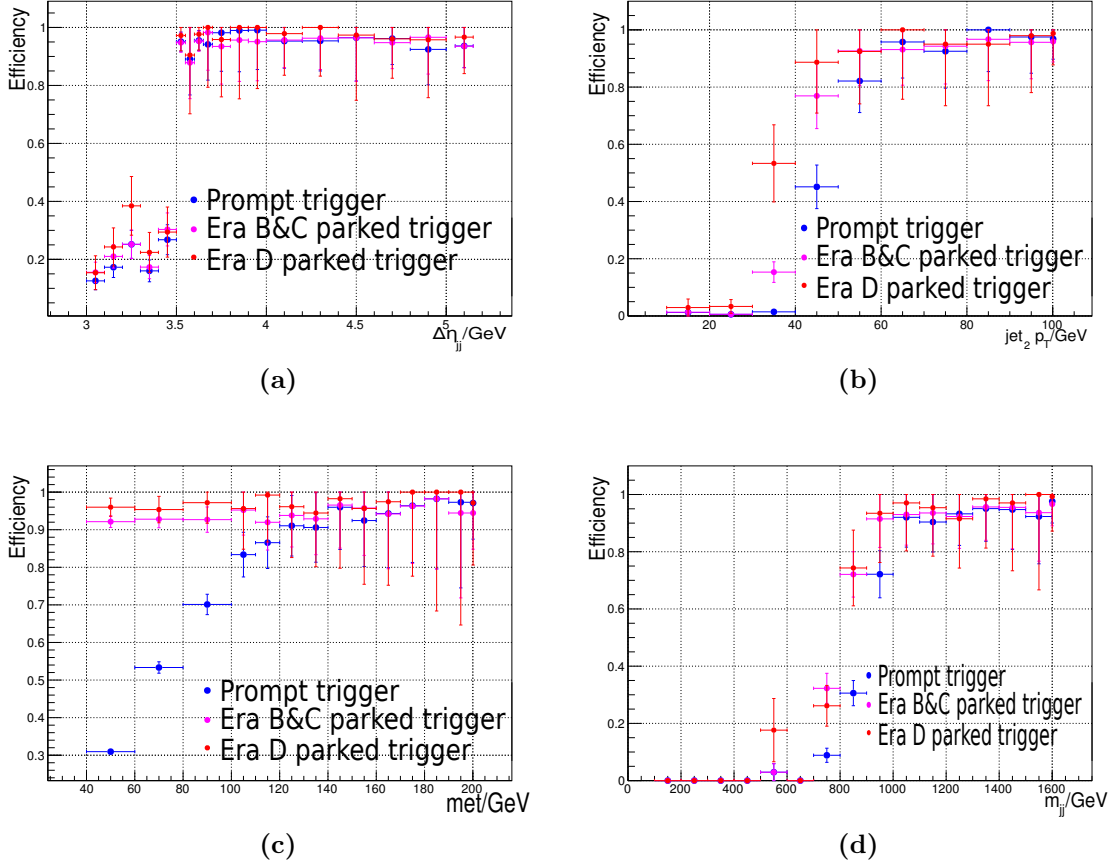


Figure 4.1.: The efficiency of the HLT requirements used in the prompt (blue) and parked (purple and red) data analyses as a function of the values of several offline variables, measured in a sample of events recorded on a single-muon trigger. (a) Efficiency as a function of offline $\Delta\eta_{jj}$, (b) efficiency as a function of sub-leading jet p_T , (c) efficiency as a function of offline $\cancel{E}_T^{\text{no-}\mu}$, (d) efficiency as a function of M_{jj} .

The efficiency for events passing both the prompt analysis trigger and the two triggers used for the parked data analysis, described in [Chapter 4.4](#) as a function of their values of several offline variables, measured in single muon data collected using an uncorrelated trigger, is shown in Figs. 4.1 and 4.2. The events used in the trigger efficiency measurement are required to pass the following cuts:

$$M_{jj} > 1100 \text{ GeV}, \cancel{E}_T^{\text{no-}\mu} > 130 \text{ GeV}, \text{leading 2 jets' } p_T > 50 \text{ GeV}, \Delta\eta_{jj} > 4.2, \eta_{j1} \cdot \eta_{j2} < 0. \quad (4.1)$$

In each measurement the cut on the variable being studied is removed. The measured trigger efficiency is applied as an event-by-event weight to all MC samples.

 Number: 1 Author: ptd Subject: Highlight Date: 09/06/2016 23:33:10
[to be fixed]

4.1.2. Offline selection

The offline selection is chosen for three reasons. Firstly, the reconstruction algorithms for some objects are only well validated for certain values of p_T and η . This consideration decides the p_T thresholds for jets and leptons to be used. Secondly, as can be seen from Figure 4.1, the values of the offline variables where the trigger becomes fully efficient are in some cases much higher than the online cut. Because the variables used in the trigger are highly correlated, and the measurements of trigger efficiency made do not take this into account, the offline cuts on all variables used in the trigger were chosen such that the trigger efficiency for the variable at that point is greater than 95%. Finally, some of the cuts imposed aim to reduce the contribution from background processes, which improves the signal to background ratio in the resulting region, and thus the expected limit on $\mathcal{B}(H \rightarrow \text{inv})$.

The specific set of offline selection cuts chosen begins by requiring that events have no veto muons or electrons, as defined in [\[1\]ections](#) 3.4 and 3.5. Signal events are not expected to contain leptons, while background events are, so this lepton veto reduces the background from W and Z boson decays and also from top quarks without removing signal events. The two highest p_T jets in the event are then identified as the VBF tag pair, and tighter versions of the trigger selection, motivated by the trigger efficiency considerations described above, are then applied. Specifically, the tag jets are required to be in opposite forward/backward halves of the detector, to both have $p_T > 50$ GeV to have $M_{jj} > 1100$ GeV and $\Delta\eta_{jj} > 4.2$. Again due to trigger efficiency considerations, $\cancel{E}_T^{\text{no-}\mu}$ is required to be greater than 130 GeV. Because events with veto muons have been removed by the lepton veto, $\cancel{E}_T^{\text{no-}\mu}$ in this region is identical to \cancel{E}_T . However, it is important [\[3\]](#) for background estimation methods [\[4\]](#) that $\cancel{E}_T^{\text{no-}\mu}$ and not \cancel{E}_T is used.

As well as the [\[5\]igger based](#) selection, further cuts are made to reduce the QCD background to a level much lower than the V+jets backgrounds. The two tag jets are required to have an azimuthal separation, $\Delta\phi_{jj} < 1.0$, since multijet events with \cancel{E}_T due to mismeasurement are most likely to have their jets back-to-back in the detector, i.e. with $\Delta\phi_{jj} = \pi$. Events where there are any jets with $p_T > 30$ GeV between the two tag jets in η are also vetoed. This CJV is motivated by the lack of colour connection, described in Section 1.2.1, between the quarks in VBF production that makes the presence of such jets unlikely in genuine signal events. The region of phase space remaining after all these cuts have been applied is called the signal region.

 Number: 1 Author: ptd Subject: Highlight Date: 10/06/2016 00:10:17
Sections [capitalise]

 Number: 2 Author: ptd Subject: Inserted Text Date: 10/06/2016 00:12:32

 Number: 3 Author: ptd Subject: Inserted Text Date: 10/06/2016 00:11:14

,

 Number: 4 Author: ptd Subject: Inserted Text Date: 10/06/2016 00:11:23

,

 Number: 5 Author: ptd Subject: Highlight Date: 10/06/2016 00:11:45
[hyphenate]

Finally, the values of the cuts are optimised to provide the best expected limit on $\mathcal{B}(H \rightarrow \text{inv})$ for a 125 GeV Higgs boson, which is calculated using the method described in Section 1.4 using the same background estimation and systematic uncertainties as the final analysis [1] described in Sections 4.2 and 4.3 respectively [2]. For the tag jet p_T and $\cancel{E}_T^{\text{no-}\mu}$, no improvement in the expected limit is seen by tightening the cut, so the requirement is set at the 95% efficiency point of the trigger. The distributions and cut values for several of the other variables used are shown in Figure 4.3. The full selection gives an efficiency of $(6.8 \pm 0.3) \times 10^{-3}$ for selecting events from invisible decays of a [4]BF produced 125 GeV Higgs boson, measured using MC.

4.2. Background estimation

As discussed in Section 4.1 there are several background processes which are capable of producing VBF-like jets in association with \cancel{E}_T . The event selection removes most of these events, however a significant number still remain and it is important to estimate this number precisely. [5]ata-driven methods, where data “control regions”, which are similar to the signal region, are used to estimate the most significant backgrounds. This data-driven approach is particularly important as the very stringent kinematic requirements placed on the tag jets lead to large uncertainties on estimates taken from MC alone. The particular method used to estimate each of the backgrounds will be described in this section.

4.2.1. $W \rightarrow e\nu + \text{jets}$

The $W + \text{jets}$ background where the W boson decays to an electron and an electron neutrino, $W \rightarrow e\nu$, is estimated using single electron events. All aspects of the event selection are the same as those used in the signal region, except for the electron veto, which is replaced with the requirement that there is exactly one tight electron in the event and no other veto electrons. These requirements give a single electron control region composed of events with jets that have the same kinematics as those in the signal region, but which is dominated by $W \rightarrow e\nu$ events.

The number of $W \rightarrow e\nu$ events in the signal region is then estimated by using the ratio between the expected number of events in the signal and control regions from MC to extrapolate from the number of events seen in data in the single electron control region

Page: 60

 Number: 1 Author: ptd Subject: Inserted Text Date: 10/06/2016 00:12:54
(

 Number: 2 Author: ptd Subject: Inserted Text Date: 10/06/2016 00:13:27
,

 Number: 3 Author: ptd Subject: Inserted Text Date: 10/06/2016 00:13:38
)

 Number: 4 Author: ptd Subject: Highlight Date: 10/06/2016 00:13:58
[hyphenate]

 Number: 5 Author: ptd Subject: Highlight Date: 10/06/2016 00:18:03
[Something wrong with this sentence... does not read properly. Do you mean

Data-driven methods, WITH data "control-regions" [no comma] which are similar to the signal region,
are used to estimate the most significant backgrounds

?]

Table 4.1.: The inputs to, and results of, the $W \rightarrow e\nu$ background estimation. $N_{W \rightarrow e\nu}$ is, for the signal region the number of events expected from $W \rightarrow e\nu$ backgrounds, and for the control region the number of events remaining in the region after the subtraction of other backgrounds.

	Signal region	Control region
N_{Data}	N/A	64
N_{Bkg}	N/A	7.42 ± 2.78 (MC stat.)
N_{MC}	105 ± 10 (MC stat.)	86.6 ± 7.1 (MC stat.)
$N_{W \rightarrow e\nu}$	68.7 ± 10.3 (stat) ± 8.8 (MC stat.)	56.6 ± 8.5 (stat)

using the following formula:

$$N_{Exp}^S = (N_{Data}^C - N_{Bkg}^C) \cdot \frac{N_{MC}^S}{N_{MC}^C}, \quad (4.2)$$

where N_{Exp}^S is the number of expected events in the signal region from this background process, N_{Data}^C is the number of events seen in the control region in data, N_{Bkg}^C is the number of events from other backgrounds in the control region estimated using MC, which is expected to be small, and N_{MC}^S and N_{MC}^C are the numbers of events predicted by MC to be in the signal and control regions respectively. The fact that estimations from MC are only used in ratios, or where they are expected to be small, significantly reduces the dependence of the final background estimation on the overall rate of the process predicted by MC and instead allows the observed rate in data to be used. It is important that the shape of the variables which differ between the control and signal regions are well modelled by the MC. The modelling of the shape of two key variables, the $E_T^{no-\mu}$ and the electron p_T , are shown in Figure 4.4. It can be seen that whilst the overall rate is significantly different between data and MC, the shape of the distribution is modelled well. The inputs to, and results of, the background estimation are shown in Table 4.1.

4.2.2. $W \rightarrow \mu\nu + \text{jets}$

The method used to estimate the background from $W+\text{jets}$ where the W boson decays to a muon and a muon neutrino, $W \rightarrow \mu\nu$, is very similar to that used for $W \rightarrow e\nu$. A single muon control region is used which replaces the muon veto of the signal region with a requirement that there is exactly one tight muon and no other veto muons. All

Table 4.3.: The inputs to, and results of, the $W \rightarrow \tau\nu$ background estimation. $N_{W \rightarrow \tau\nu}$ is, for the signal region the number of events expected from $W \rightarrow \tau\nu$ backgrounds, and in the control region the number of events remaining in the region after the subtraction of other backgrounds.

	Signal region	Control region
N_{Data}	N/A	32
N_{Bkg}	N/A	14.7 ± 3.4 (MC stat.)
N_{MC}	95.6 ± 8.5 (MC stat.)	29.2 ± 3.6 (MC stat.)
$N_{W \rightarrow \tau\nu}$	56.5 ± 21.5 (stat) ± 8.6 (MC stat.)	17.3 ± 3.9 (stat)

efficiency and fake rate. Specifically [1] an alternative isolation algorithm was investigated which used a multi-variate analysis (MVA) approach to estimate the isolation sum, as well as different working points for the anti-electron and anti-muon discriminators [91]. The tau identification efficiency was found to be higher for both the alternative isolation algorithm and different working points for the anti-lepton discriminators, being twice as large if both were used compared to the standard tau identification. However, the rate of $W \rightarrow e\nu$ events being identified as $W \rightarrow \tau\nu$ was also significantly increased, going from 2% for the standard identification to 15% when the alternative isolation and anti-lepton discriminators were used. It was therefore decided to use the tau identification described in Section 3.8.

The final estimation of the background from $W \rightarrow \tau\nu$ is carried out using Equation 4.2, with the single tau control region with no CJV being used as the control region. The inputs to, and results of, the background estimation are shown in Table 4.3. Distributions of the tau p_T and $\Delta\phi_{jj}$ in the single tau control region are shown in Figure 4.6, it can be seen that the shape of the two distributions in data and MC agree well with the exception of the high $\Delta\phi_{jj}$ region which is not part of either the signal or tau control regions.

4.2.4. $Z \rightarrow \nu\nu + \text{jets}$

The background from $Z+\text{jets}$ where the Z decays to neutrinos, $Z \rightarrow \nu\nu$, is different from the $W+\text{jets}$ backgrounds described above, in that nothing is required to be misidentified in order for these events to contribute to the signal region. The method used to estimate the $Z \rightarrow \nu\nu$ background therefore differs slightly from that used above. The method

 Number: 1 Author: ptd Subject: Inserted Text Date: 10/06/2016 00:20:08

,

 Number: 2 Author: ptd Subject: Inserted Text Date: 10/06/2016 00:21:32
and [to avoid comma splice]

uses a dimuon control region which is populated by events from the process $Z/\gamma^* \rightarrow \mu\mu$. As this process can be mediated by a photon, the kinematics of the jets in $Z/\gamma^* \rightarrow \mu\mu$ events can be different to those from $Z \rightarrow \nu\nu$. The dimuon control region that is defined therefore has a requirement that the invariant mass of the dimuons be between 60 and 120 GeV. The control region is otherwise identical to the signal region, except that the muon veto is replaced with a requirement that there are exactly two tight muons and no other veto muons.

As well as the possibility of different kinematics, $Z/\gamma^* \rightarrow \mu\mu$ and $Z[1] \rightarrow \nu\nu$ also have different cross-sections. The formula used to estimate the $Z[2] \rightarrow \nu\nu$ background takes this into account as follows:

$$N_{Exp}^S = (N_{Data}^C - N_{Bkg}^C) \cdot \frac{\sigma(Z \rightarrow \nu\nu)}{\sigma(Z/\gamma^* \rightarrow \mu\mu)} \cdot \frac{\epsilon_{VBF}^S}{\epsilon_{VBF}^C}, \quad (4.3)$$

where $\sigma(Z \rightarrow \nu\nu)$ is the cross-section for $Z \rightarrow \nu\nu$ and $\sigma(Z/\gamma^* \rightarrow \mu\mu)$ is the cross-section for $Z/\gamma^* \rightarrow \mu\mu$. ϵ_{VBF}^S and ϵ_{VBF}^C are the efficiencies for $Z \rightarrow \nu\nu$ events to pass the signal region selection and $Z/\gamma^* \rightarrow \mu\mu$ events to pass the control region selection respectively. As Z bosons can be created via either QCD or electroweak processes, which ~~both~~⁴ have different cross-sections and efficiencies, ϵ_{VBF}^S and ϵ_{VBF}^C , are a cross-section weighted average of the efficiency for both types of production, calculated as:

$$\epsilon_{VBF}^S = \frac{\sigma(Z \rightarrow \nu\nu, EWK) \frac{N_{MC}^S(EWK)}{N_{gen}(Zmass,EWK)} + \sigma(Z \rightarrow \nu\nu, QCD) \frac{N_{MC}^S(QCD)}{N_{gen}(Zmass,QCD)}}{\sigma(Z \rightarrow \nu\nu, EWK) + \sigma(Z \rightarrow \nu\nu, QCD)}, \quad (4.4)$$

$$\epsilon_{VBF}^C = \frac{\sigma(Z/\gamma^* \rightarrow \mu\mu, EWK) \frac{N_{MC}^C(EWK)}{N_{gen}(EWK)} + \sigma(Z/\gamma^* \rightarrow \mu\mu, QCD) \frac{N_{MC}^C(QCD)}{N_{gen}(QCD)}}{\sigma(Z/\gamma^* \rightarrow \mu\mu, EWK) + \sigma(Z/\gamma^* \rightarrow \mu\mu, QCD)}, \quad (4.5)$$

where EWK and QCD denote where cross-sections or numbers of events are for electroweak or QCD production of a Z boson. N_{gen} is the number of events in the $Z+jets$ MC sample at generator level. Due to the limited size of the available $Z \rightarrow \nu\nu$ MC samples, the same $Z/\gamma^* \rightarrow \mu\mu$ samples used for the MC estimate of the number of events in the control region are used to obtain an estimate from MC of the number of events from the $Z \rightarrow \nu\nu$ process in the signal region. For this estimate the leptons in the $Z/\gamma^* \rightarrow \mu\mu$ samples are ignored, the production cross-section is scaled to the appropriate $Z \rightarrow \nu\nu$ value and it is required that there is a ~~generator level~~ dimuon in the event with invariant mass between 80 and 100 GeV. The generated dimuon mass for this sample was required to be greater than 50 GeV, so the cross-sections used in Equations 4.3, 4.4 and 4.5 are also calculated with this constraint. For the control region N_{gen} is calculated

Page: 68

 Number: 1 Author: ptd Subject: Cross-Out Date: 10/06/2016 00:22:24

 Number: 2 Author: ptd Subject: Cross-Out Date: 10/06/2016 00:22:29

 Number: 3 Author: ptd Subject: Highlight Date: 10/06/2016 00:29:11

[The subscript seems to be "V BF", with a space between "V" and "BF"... Needs to be fixed, here and everywhere else the same problem occurs. Happens again in page 104, for instance.]

 Number: 4 Author: ptd Subject: Cross-Out Date: 10/06/2016 00:25:16

 Number: 5 Author: ptd Subject: Highlight Date: 10/06/2016 00:33:43

[Similar to "V BF" issue pointed out above: in this formula we get "EW K" and "QC D". Use eg \mbox{\mathrm{QCD}} to ensure no spaces, and roman upright script. Needs to be fixed here, in the text below, and everywhere else it occurs (for instance, happens again in page 104).]

 Number: 6 Author: ptd Subject: Highlight Date: 10/06/2016 00:34:34

[The superscript here should be "C" instead of "S", I think.]

 Number: 7 Author: ptd Subject: Highlight Date: 10/06/2016 00:23:46

[hyphenate]

Table 4.4.: The input variables for the calculation of ϵ_{VBF}^S and ϵ_{VBF}^C using Equations 4.4 and 4.5 respectively.

Variable	Value
$\sigma(Z \rightarrow \nu\nu, \text{EWK})$	1.380 pb
$\sigma(Z \rightarrow \nu\nu, \text{QCD})$	6600 pb
$\sigma(Z/\gamma^* \rightarrow \mu\mu, \text{EWK})$	0.303 pb
$\sigma(Z/\gamma^* \rightarrow \mu\mu, \text{QCD})$	1168 pb
$\frac{N_{MC}^S(\text{EWK})}{N_{gen}(\text{Zmass,EWK})}$	$(1.3 \pm 0.1) \cdot 10^{-3}$
$\frac{N_{MC}^S(\text{QCD})}{N_{gen}(\text{Zmass,QCD})}$	$(1.4 \pm 0.2) \cdot 10^{-6}$
$\frac{N_{MC}^C(\text{EWK})}{N_{gen}(\text{EWK})}$	$(7.5 \pm 0.3) \cdot 10^{-4}$
$\frac{N_{MC}^C(\text{QCD})}{N_{gen}(\text{QCD})}$	$(9.2 \pm 1.2) \cdot 10^{-7}$

after requiring that the mass of the generator level dimuon is between 60 and 120 GeV, denoted by the label $\text{[3]mass } \text{[4]}$. Equations 4.4 and 4.5.

The inputs to Equations 4.4 and 4.5 are given in Table 4.4. The cross-sections for electroweak Z boson production were calculated at NLO using VBFNLO which specialises in vector boson production. The cross-section for QCD production of $Z/\gamma^* \rightarrow \mu\mu$ is calculated using FEWZ inclusively for all leptons and then divided by three to obtain the figure for muons only. This cross-section is then multiplied by the ratio between the cross-section for $Z \rightarrow \nu\nu$ and $Z/\gamma^* \rightarrow \mu\mu$, which was calculated to be 5.651 at NLO using MCFM, to obtain the QCD production cross-section for $Z \rightarrow \nu\nu$. The inputs to Equation 4.3 are given in Table 4.5, with the exception of the ratio between the total production cross-sections for $Z \rightarrow \nu\nu$ and $Z/\gamma^* \rightarrow \mu\mu$ which is taken to be the same 5.651 that it is found ~~[6]~~ to be for QCD production. This approximation is used because the electroweak contribution to the ratio is smaller than that from QCD by more than a factor of one thousand and is therefore negligible. The distributions of $E_T^{\text{no-}\mu}$ and M_{jj} for a Z control region with relaxed selection, to ensure sufficient numbers of events, are shown in Figure 4.7, demonstrating that the MC samples model the data distribution well.

Page: 69

 Number: 1 Author: ptd Subject: Highlight Date: 10/06/2016 00:35:15

 Number: 2 Author: ptd Subject: Highlight Date: 10/06/2016 00:35:18

 Number: 3 Author: ptd Subject: Inserted Text Date: 10/06/2016 00:35:38
"

 Number: 4 Author: ptd Subject: Inserted Text Date: 10/06/2016 00:35:46
"

 Number: 5 Author: ptd Subject: Highlight Date: 10/06/2016 00:36:07
Equations

 Number: 6 Author: ptd Subject: Cross-Out Date: 10/06/2016 00:36:59

 Number: 7 Author: ptd Subject: Inserted Text Date: 10/06/2016 00:36:53
was

Table 4.5.: The inputs to, and results of, the $Z \rightarrow \nu\nu$ background estimation using Equation 4.3. ϵ_{VBF} in the signal (control) region is calculated using Equation 4.4 (4.5). $N_{Z \rightarrow \nu\nu}/N_{Z/\gamma^* \rightarrow \mu\mu}$ is in the signal region the number of events expected from $Z \rightarrow \nu\nu$ backgrounds, and for the control region the number of events remaining in the region after the subtraction of other backgrounds. The systematic uncertainties are calculated as described in Section 4.3.

	Signal region	Control region
N_{Data}	N/A	12
N_{Bkg}	N/A	0.3 ± 0.1 (MC stat.)
ϵ_{VBF}	$(1.65 \pm 0.15 \text{ (stat)} \pm 0.22 \text{ (syst)}) \cdot 10^{-6}$	$(1.11 \pm 0.12 \text{ (stat)} \pm 0.12 \text{ (syst)}) \cdot 10^{-6}$
$\boxed{\Gamma_{Z \rightarrow \nu\nu/Z \rightarrow / \gamma^* \rightarrow \mu\mu}}$	$99 \pm 29 \text{ (stat)} \pm 25 \text{ (syst)}$	11.7 ± 0.1 (MC stat.)

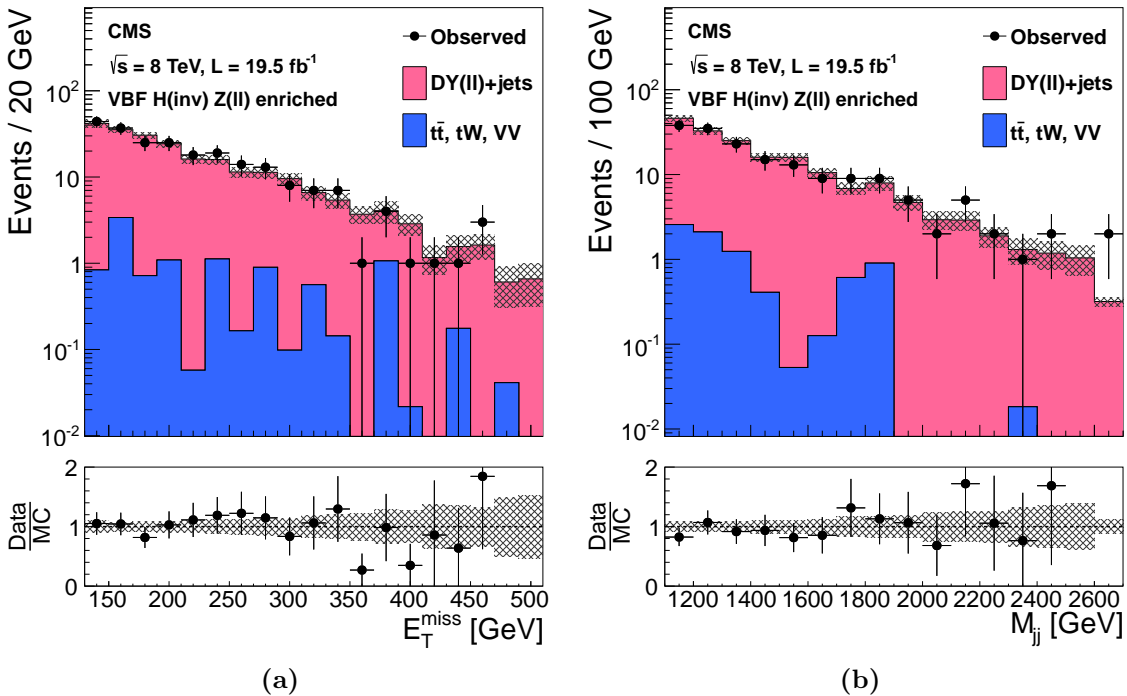


Figure 4.7.: Distributions of the $E_T^{\text{no-}\mu}$ (a) and M_{jj} (b) in a relaxed Z control region, with no requirement on $\Delta\phi_{jj}$, the CJV removed, and the requirements on M_{jj} and $\Delta\eta_{jj}$ relaxed to 1000 GeV and 3.5 respectively. DY(II)+jets indicates the contribution from $Z+jets$ processes and $t\bar{t}$, tW , VV indicates the contribution from minor backgrounds. The hatched region illustrates the systematic uncertainty [1].

Page: 70

 Number: 1 Author: ptd Subject: Highlight Date: 10/06/2016 00:40:14
[This is garbled... Delete and then copy & paste from the caption above.]

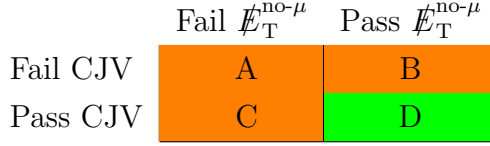


Figure 4.8.: A diagram of the regions used in the QCD ABCD background estimation method. Region D is the signal region and regions A, B and C are mutually exclusive control regions.

4.2.5. QCD

The QCD background remaining after the full event selection is mostly from events where jets are mismeasured. The size of the MC samples available for studying this process is not sufficient for them to be relied upon for extrapolation from a control region to the signal region. The remaining QCD background is therefore estimated using a so-called “ABCD” method. In this method four regions, A, B, C and D, are defined according to whether events pass or fail the $\cancel{E}_T^{\text{no-}\mu}$ and CJV cuts^[1] shown in Figure 4.8. Region D is the signal region and regions A, B and C are three mutually exclusive control regions.

The efficiency to pass the $\cancel{E}_T^{\text{no-}\mu}$ and CJV cuts can be determined from the ratios between regions A and B, and A and C respectively. The number of events expected in the signal region is then:

$$N_D = N_A \cdot \frac{N_B}{N_A} \cdot \frac{N_C}{N_A} = \frac{N_B \cdot N_C}{N_A}, \quad (4.6)$$

where $N_{A,B,C}$ is the number of events observed in region A, B, C in data minus the number expected from V+jets or other minor backgrounds, i.e. the number of events in the region believed to be from QCD. This method relies on the probability of an event passing the CJV being uncorrelated with the $\cancel{E}_T^{\text{no-}\mu}$ of the event. This has been checked by comparing the $\cancel{E}_T^{\text{no-}\mu}$ distribution, below the 130 GeV signal region requirement, for events which pass and fail the CJV.^[2] The maximum fractional difference observed between bins of these two distributions is 40%, so this is added as a systematic to the QCD background yield. The method was also tested in a region orthogonal to the signal region with all requirements the same as those of the signal region except $\Delta\phi_{jj}$ which was required to be greater than 2.6. In this test region, which is expected to be QCD dominated, the prediction agreed with the expectation within 15%, which is within the

 Number: 1 Author: ptd Subject: Inserted Text Date: 10/06/2016 00:41:13

,

 Number: 2 Author: ptd Subject: Inserted Text Date: 10/06/2016 00:42:43
(see Figure 4.9)

4.2.6. Minor backgrounds

In addition to the V+jets and QCD backgrounds which account for 94% of the expected events in the signal region, there is also a small number of events expected from other minor backgrounds including single top quark production, top quark pair production, diboson production and $Z/\gamma^* \rightarrow \mu\mu$. Due to their small contributions these numbers of events are taken directly from MC. The diboson backgrounds are simulated using PYTHIA 6, the single top quark background using POWHEG and the top quark pair production and $Z/\gamma^* \rightarrow \ell\ell$ backgrounds using MADGRAPH. The cross-sections used to normalise these MC samples were taken from the most **1** to date CMS published results at the time of the analysis [94–98]. The final estimate of the number of events from minor backgrounds in the signal region is 20 ± 8.2 (MC stat), with 70% of these expected to be from diboson production.

4.3. Systematic uncertainties

The dominant uncertainties in the analysis are the statistical uncertainties on the V+jets backgrounds due to the number of data events observed in the control regions. In addition, as well as those mentioned in Section 4.2, there are several further systematic uncertainties on the expected numbers of signal and background events. These uncertainties are described individually below and the fractional uncertainty on the total expected number of signal and background events from all sources of uncertainty are summarised in Table 4.7.

4.3.1. Jet energy scale

The reconstructed energy of a jet reconstructed by CMS is not necessarily the same as the true energy of all the particles that make it up. As described in Section 3.6.3, jet corrections are applied to remedy this. The correction for the ratio between reconstructed and true jet energy is referred to as the JES. Uncertainties on the JES come from several sources. The JES obtained from the dijet p_T balance method for instance has an uncertainty from the jet resolution bias [88]. This bias arises because the jet p_T spectrum sharply falls with increasing p_T . Such a spectrum leads to the well measured jet being used as the base for the balance method to be more likely to have fluctuated up in p_T than down. The main uncertainties in the photon/Z balance methods come from the

 Number: 1 Author: ptd Subject: Highlight Date: 10/06/2016 00:43:46
up-to-date [hyphenate]

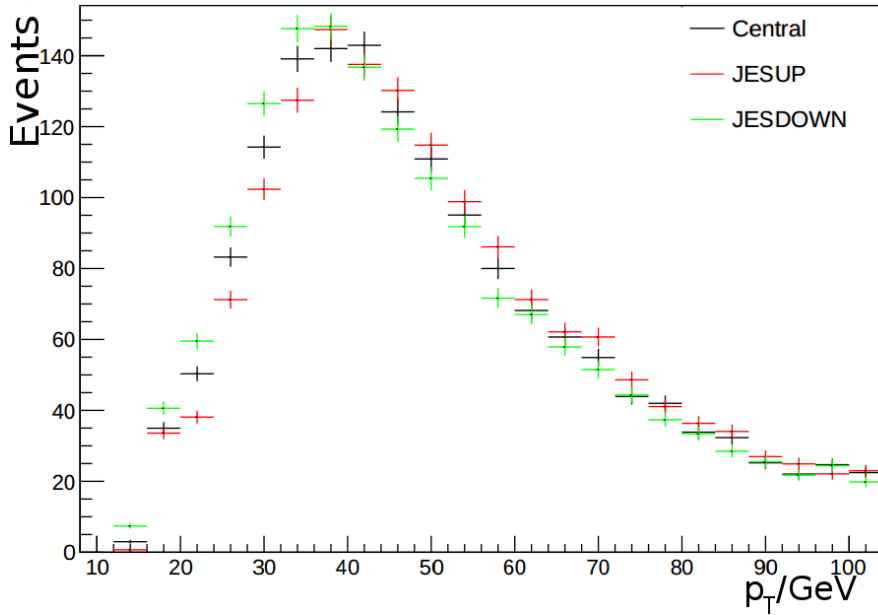


Figure 4.10.: The distribution of the sub-leading jet’s p_T in W+Jets MC events with the nominal JES and for JESUP and JESDOWN.

limited number of events in the samples used. The JES obtained in MC is also different when measured with different MC generators, which leads to an uncertainty.

These uncertainties on the JES give rise to an uncertainty on the energy of all jets in CMS events. The impact of this uncertainty on the expected and observed event yields in this analysis was estimated by altering the JES correction up by one standard deviation, “JESUP”, and down by one standard deviation “JESDOWN”, and recalculating the energy and momentum of all jets in each event. The \cancel{E}_T is recalculated taking into account the updated jet energies. Furthermore, as the jet energy scale uncertainty varies with p_T and η , it is possible for the p_T ordering of the jets to change when the JES is changed. The VBF tag pair is therefore ~~rechosen~~^[1] to be the new highest p_T pair of jets.

After modifying the JES, the analysis is ~~reperformed~~^[2] and the resulting change in the expected signal and background yields is taken to be the uncertainty due to the JES. The sub-leading jet’s p_T in a W+jets MC sample is shown for the nominal JES, JESUP and JESDOWN in Figure 4.10. It can be seen that altering the JES results in a smooth change in the jet p_T , indicating that the difference in the number of events passing the analysis cuts is not due to individual events with large weights migrating in and out of the signal region.

Page: 74

 Number: 1 Author: ptd Subject: Inserted Text Date: 10/06/2016 00:45:25
[not a word, unfortunately ;-)]

chosen again, so as

 Number: 2 Author: ptd Subject: Inserted Text Date: 10/06/2016 00:45:56
[ditto]

performed again

4.3.2. Jet energy resolution

The width of the jet energy distribution, the jet energy resolution (JER), differs between MC and data. This is partly due to MC samples being generated before and during data taking, and thus before a measurement of the exact resolution in data can be performed. Measuring the JER in data is done in a very similar way to the measurement of the JES using dijet and photon/Z-jet balance techniques and by comparing the reconstructed energy to that generated in MC, and thus has the same sources of uncertainty.

To correct the MC resolution to match that in the data, the p_T of all jets in MC is “smeared”. The smearing is carried out using two methods. The first method is used for jets in MC that are within 0.5 in the $\eta - \phi$ plane of a generator jet. In this method the difference between the reconstructed and generator jet p_T is scaled by a correction factor, c , chosen to be the ratio between the resolution of the data and MC and calculated as a function of the jet’s p_T and η . The resulting jet p_T is given by:

$$p'_T = \max [0, p_{T\text{gen}} + \boxed{1}(p_T - p_{T\text{gen}})], \quad (4.7)$$

where p_T is the initial transverse momentum, p'_T is the transverse momentum after smearing and $p_{T\text{gen}}$ is the matched generator jet’s [2]. This procedure has the advantage that the smearing is not reliant on random factors and is therefore reproducible, making synchronisation between analysis implementations easier.

The second method is used when a jet has no matching generator jet. In this case a random correction is necessary. The technique used is to add a fluctuation to the jet’s [3] p_T with a size obtained by sampling a gaussian with width:

$$\sqrt{(c^2 - 1) \sigma_{MC}}, \quad (4.8)$$

where c is the same correction factor from the method above and σ_{MC} is the initial MC resolution as a function of p_T and η . σ_{MC} was measured by performing a gaussian fit to the distribution of the ratio between the generator level and offline jet p_T observed in W+jets MC. As well as being random and thus difficult to reproduce, this method has the disadvantage that it can only be used to worsen the resolution.

The analysis is performed three times with three different smearings, one where the MC resolution is smeared to match the nominal data resolution, which is used for the main signal and background estimations, and two where the MC resolution is made to match the improvement, “JERBETTER” and worsening, “JERWORSE” of the jet energy

Page: 75

 Number: 1 Author: ptd Subject: Highlight Date: 10/06/2016 12:51:31
[italic, for consistency with notation in text/equation above and below...]

 Number: 2 Author: ptd Subject: Inserted Text Date: 10/06/2016 12:51:46
jet

 Number: 3 Author: ptd Subject: Inserted Text Date: 10/06/2016 00:46:39
jet

probe method used to measure them, and the difference in the resulting signal and background yield used as the uncertainty from this source.

An uncertainty of 8% is added to the estimate of the $W \rightarrow \tau\nu$ background to account for the uncertainty in the tau identification efficiency, which is measured using $Z \rightarrow \tau\tau$ events where one tau decays to a muon and the other hadronically [99]. 5% of events in the $W \rightarrow \tau\nu$ control region also appear to be due to $W \rightarrow e\nu$ events where the electron or a jet has been misreconstructed as a tau, so a further 5% systematic is assigned to the $W \rightarrow \tau\nu$ estimate.

4.3.5. Other uncertainties

Additional uncertainties arise from several sources. For instance, the $Z \rightarrow \nu\nu$ background estimate is reliant on the ratio of the cross-sections for the $Z \rightarrow \nu\nu$ and $Z/\gamma^* \rightarrow \mu\mu$ processes in the phase space of this analysis. A 20% uncertainty on this ratio was applied to cover the difference between the values of the ratio calculated using MADGRAPH and using MCFM [5]. Further uncertainties come from the measurement of the distribution of the number of primary vertices used in the pileup weights, described in Section 3.9, the PDFs and QCD scale used in the signal cross-section measurements [100, 101], differences in the ggH $\Delta\phi_{jj}$ spectrum depending on the MC generator used [5], the cross-sections used to normalise the minor backgrounds, described in Section 4.2.6, and the measurement of the total integrated luminosity [92].

4.4. Results

The final results of all the background estimation methods and systematic uncertainty studies are summarised in Table 4.8. The total number of events expected from background processes in the signal region is 332 ± 46 (stat) ± 45 (syst). The presence of a Higgs boson with a mass of 125 GeV, SM production and $\mathcal{B}(H \rightarrow \text{inv}) = 100\%$ would be expected to yield 224 ± 31 signal events would be expected, with 6% of these from ggH and the remainder from VBF production. 390 events are observed, which is within one standard deviation of the **Background only** prediction. Figure 4.11 shows the $\cancel{E}_T^{\text{no-}\mu}$ and M_{jj} of the background and signal events expected, and the data observed, in the signal region.

 Number: 1 Author: ptd Subject: Highlight Date: 12/06/2016 17:36:32
[hyphenate]

As no excess is observed, the asymptotic CL_S technique, described in Section 1.4, is used to place an upper limit on the production cross-section times branching fraction, $\sigma \times \mathcal{B}$, at 95% CL. Under the assumption of SM production this limit can be interpreted as a limit on $\mathcal{B}(H \rightarrow \text{inv})$. All systematic uncertainties are modelled as log-normally distributed nuisance parameters, with the exception of the statistical uncertainty on the $Z \rightarrow \nu\nu$ background, which is modelled as a gamma-normally distributed nuisance due to the low number of events in the dimuon control region. A gamma-normal distribution is used in the case of control regions with low numbers of events because in this case the central limit theorem does not apply so the Poisson probability of observing a certain number of events is very asymmetric; this asymmetry is well modelled by a gamma-normal distribution [102].

The resulting upper limits are shown as a function of Higgs boson mass in Figure 4.12, with the 95% CL observed (expected) limit on $\mathcal{B}(H \rightarrow \text{inv})$ for a 125 GeV Higgs boson being 65% (49%). The green and yellow bands shown in Figure 4.12 denote the one and two sigma uncertainty bands respectively of the expected limit, also calculated using the asymptotic technique. The one (two) sigma band represents the region that the observation is expected to lie in 68% (95%) of the time if the **Background only** hypothesis is true.

This was the first published search for invisibly decaying Higgs bosons in the VBF channel. It can be seen that for all values of Higgs boson mass investigated the observed limit is approximately one sigma above the expected limit. If the measurements of the limit at each Higgs boson mass were not correlated, this could be seen as evidence for an excess. However, as this analysis has only a single bin, and no information on the shape of the event variable distributions is used, the measurements for the different Higgs boson masses are 100% correlated with each other. The analysis therefore sees no significant evidence of non-SM behaviour.

The parked data, described in Section 2.2.5, used for this analysis was collected using a range of triggers with similar but looser requirements than those used for the prompt data (“prompt”) analysis described in the previous chapter. These looser requirements allow areas of phase space which were previously removed by the prompt trigger to be used. However, these areas also have very large QCD backgrounds, and require the analysis selection and some background estimation methods to be redesigned compared to the prompt analysis. As it was reconstructed later the parked data also uses different, better, detector calibrations (such as the jet energy calibrations), calculated with the full Run 1 LHC dataset. The parked data analysis was also carried out using a new code

 Number: 1 Author: ptd Subject: Highlight Date: 12/06/2016 17:37:13
[hyphenate]

Table 4.9.: A summary of the requirements of the triggers used for this analysis in each Run 1 era. All triggers require that there is at least one pair of jets in the event satisfying all of the jet requirements listed in this table. All requirements are on HLT variables unless stated otherwise.

Variable	Cut in era				
	A	B & C	D		
L1 \cancel{E}_T	> 40 GeV				
$\cancel{E}_T^{\text{no-}\mu}$	> 65 GeV	No requirement			
jet p_T of both jets	> 40 GeV	> 35 GeV	> 30 GeV		
M_{jj}	> 800 GeV	> 700 GeV			
$\Delta\eta_{jj}$	> 3.5				
$\eta_{j1} \cdot \eta_{j2}$	> 0				

framework, which was fully validated against that used in the prompt analysis. This analysis was made public [\[1\]](#) Ref. [2].

4.5. Trigger

The triggers used to collect the parked data varied throughout Run 1, due both to the available trigger bandwidth changing, and to the rate of the triggers used varying as the LHC instantaneous luminosity increased during the run. Run 1 was split into 4 “eras”: A, B, C and D, with 0.9, 3.9, 7.2 and 7.3 fb^{-1} of integrated luminosity collected in each respectively. During era A data were not parked, so the prompt data are used. The two other triggers used, one for eras B and C, and one for era D, differed from the prompt trigger in that there was no requirement on the \cancel{E}_T present at the HLT level and the jet p_T and M_{jj} requirements were looser. The exact values of the trigger selection cuts are summarised in Table 4.9. These looser requirements allow the [\[2\]](#) trigger driven selection applied in the prompt analysis to be relaxed, and [\[3\]](#) more optimal signal and background control regions to be used. As the region accessible with the parked data includes the prompt data signal region as a subset, no improvement would be possible from applying the analysis designed for the prompt data to the parked data without modification. Measuring the trigger efficiency is essential for any analysis. However, it is particularly

important in this analysis, where several elements of the selection are chosen to avoid regions which are expected to contain significant numbers of signal events but the trigger

Page: 82

 Number: 1 Author: ptd Subject: Inserted Text Date: 12/06/2016 14:33:02
published

 Number: 2 Author: ptd Subject: Highlight Date: 12/06/2016 14:54:04
trigger-driven

 Number: 3 Author: ptd Subject: Inserted Text Date: 12/06/2016 14:53:41
better optimised

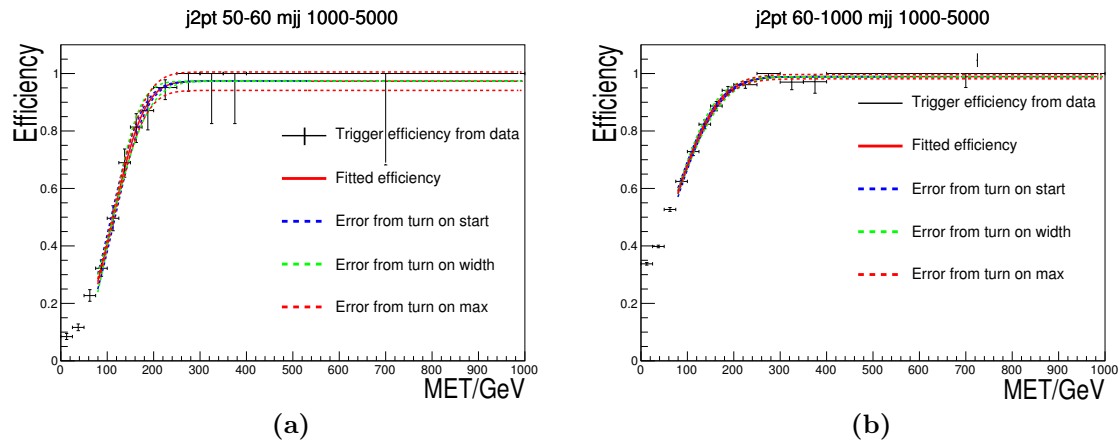


Figure 4.14.: The results of performing a fit of the function in Equation 4.9 to the efficiency of the trigger used in era D, measured in a sample of single muon events collected with an orthogonal trigger. The dashed bands show the uncertainty on the fit due to each of the three parameters of the fit. The two bins of dijet mass (m_{jj}) and sub-leading jet's p_T ($j2pt$) shown are those with the two highest numbers of events from the final signal region described in Section 4.6. The results of the fits in the other bins are shown in Appendix A.

shown in the following equation:

$$w(p_{\text{T}j2}, M_{jj}, \mathbb{E}_{\text{T}}^{\text{no-}\mu}) = \frac{\sum_i \mathcal{L}_i \epsilon_i(p_{\text{T}j2}, M_{jj}, \mathbb{E}_{\text{T}}^{\text{no-}\mu})}{\sum_i \mathcal{L}_i}, \quad (4.10)$$

where i are the three triggers, $\epsilon_i(p_{\mathrm{T}j2}, M_{jj}, \cancel{E}_{\mathrm{T}}^{\mathrm{no-}\mu})$ is the measured efficiency for trigger i as a function of the event's sub-leading jet p_{T} , M_{jj} and $\cancel{E}_{\mathrm{T}}^{\mathrm{no-}\mu}$, and \mathcal{L}_i is the integrated luminosity collected using trigger i . The resulting trigger efficiency varies smoothly and leads to no unphysical discontinuities in the distributions of event variables as can be seen from the figures in the remainder of this chapter.

4.6. Event selection

As mentioned above [1] significant challenge in the analysis of the parked data is that the additional areas of phase space collected by these triggers, but not collected by the prompt data triggers, have very large contributions from QCD backgrounds. The QCD contribution to VBF analyses is very hard to model because whilst the cross-sections for these processes are very high, the probability of any individual event being VBF-like is very low. The number of MC events that must be generated to make a representative

sample is therefore prohibitively large. As a result of these difficulties, the parked data selection is separated into two stages. The first “preselection” stage selects a region of phase space which is not expected to be dominated by QCD processes. After this preselection has been made the background processes expected to contribute are the same as in the prompt analysis, and studies were undertaken into which background estimation methods and final signal region selection leads to the best expected limit.

4.6.1. Preselection

The first element of the preselection was motivated by the trigger. The following selection was applied to ensure that the values of all event variables are above the trigger thresholds of all triggers used, and that the $\cancel{E}_T^{\text{no-}\mu}$ was above the lowest value of the **Turn on** centre, B, as defined in Equation 4.9, obtained from the fits described in Section 4.5:

$$\begin{aligned} \eta_{j1} \cdot \eta_{j2} &< 0, \text{ leading jet } p_T > 50 \text{ GeV}, \Delta\eta_{jj} > 3.6, \\ \text{sub-leading jet } p_T &> 40 \text{ GeV}, M_{jj} > 80 \text{ GeV}, \cancel{E}_T^{\text{no-}\mu} > 90 \text{ GeV}. \end{aligned} \quad (4.11)$$

Where $j1$ and $j2$ are the leading and sub-leading p_T jets in the event and are chosen as the VBF tag jets. We also require that for the “signal-like” selection there are no veto electrons or muons in the event. The W+jets and Z+jets control regions used in the background estimates described in Section 4.7 impose different lepton requirements. QCD multijet processes still dominate the region defined by this selection, as can be seen in Figure 4.15a, where there are a lot more data events than expected from the background MC prediction. This difference is due to mismeasured QCD events not being adequately modelled by the available MC samples, which are described in further detail in Section 4.7.9.

Additional selection requirements were applied to reduce the observed differences from the mismeasured QCD multijet background. The first variable that was used to achieve this reduction is the \cancel{E}_T significance, \mathcal{S} , which is defined as the ratio between $\cancel{E}_T^{\text{no-}\mu}$ and the square root of the sum of the transverse energy of all particles in the event, which is an estimate of the statistical error on the \cancel{E}_T . The intention of the \mathcal{S} cut is to remove events which have a large amount of \cancel{E}_T , but also have an even larger amount of visible energy, meaning that the \cancel{E}_T is likely to be from mismeasurement of the visible particles. The preselection requires that \mathcal{S} be greater than 3. The value of this cut was chosen by looking at Figure 4.15a and removing the region with the most disagreement between

Page: 86

 Number: 1 Author: ptd Subject: Highlight Date: 12/06/2016 15:03:53
turn-on

 Number: 2 Author: ptd Subject: Highlight Date: 12/06/2016 15:04:45
[insert half-space and "GeV" should be in mathrm]

data and MC. The resulting region shown in Figure 4.15b still does not display good data-MC agreement, however the disagreement is smaller.

After the cut on \mathcal{S} , a requirement that the $\cancel{E}_T^{\text{no-}\mu}$ is not too close to any jets in ϕ was made. This requirement was motivated by the fact that if the \cancel{E}_T is due only to the mismeasurement of a jet, the \cancel{E}_T will be aligned with that jet. Two variables were investigated, the first was the minimum azimuthal angle difference between either of the two tag jets and the $\cancel{E}_T^{\text{no-}\mu}$, $\min\Delta\phi(j_{1/2}, \cancel{E}_T^{\text{no-}\mu})$, and the second was the minimum azimuthal angle difference between any jet with p_T greater than 30 GeV and the $\cancel{E}_T^{\text{no-}\mu}$, $\min\Delta\phi(j, \cancel{E}_T^{\text{no-}\mu})$. At a similar signal efficiency the difference between the observed number of events and the MC background prediction, which is an indication of the remaining QCD multijet background, was found to be 80% smaller for a cut on $\min\Delta\phi(j, \cancel{E}_T^{\text{no-}\mu})$ than a cut on $\min\Delta\phi(j_{1/2}, \cancel{E}_T^{\text{no-}\mu})$. The same cut on $\min\Delta\phi(j, \cancel{E}_T^{\text{no-}\mu})$ was also found to reduce top quark related backgrounds by a factor of two compared to a cut on $\min\Delta\phi(j_{1/2}, \cancel{E}_T^{\text{no-}\mu})$. We therefore require that $\min\Delta\phi(j, \cancel{E}_T^{\text{no-}\mu}) > 1.0$ for events to pass the preselection. $\min\Delta\phi(j, \cancel{E}_T^{\text{no-}\mu})$ was found to give significantly better signal efficiency than the $\Delta\phi_{jj}$ variable used in the prompt analysis for the same background rejection, so no cut was made on $\Delta\phi_{jj}$.

The M_{jj} distribution after the $\min\Delta\phi(j, \cancel{E}_T^{\text{no-}\mu})$ cut is shown in Figure 4.15c. Whilst the agreement for large M_{jj} is good, it can be seen that the first bin of the distribution, where mismeasured QCD multijet events would be expected, due to their not recoiling against another object, shows a significant disagreement. The final cut of the preselection is therefore to require $M_{jj} > 1000$ GeV. This cut also ensures that none of the bins used to describe the trigger efficiency which have too few events to be reliable are used. In summary the full preselection is as follows:

$$\begin{aligned} \eta_{j1} \cdot \eta_{j2} &< 0, \text{ leading jet } p_T > 50 \text{ GeV}, \Delta\eta_{jj} > 3.6, \\ \text{sub-leading jet } p_T &> 40 \text{ GeV}, M_{jj} > 100 \text{ GeV}, \cancel{E}_T^{\text{no-}\mu} > 90 \text{ GeV}, \\ \min\Delta\phi(j, \cancel{E}_T^{\text{no-}\mu}) &> 1.0, \mathcal{S} > 3.0. \end{aligned} \quad (4.12)$$

Distributions of several variables after the full preselection are shown in Figure 4.16. No estimate of the QCD contribution is given in these distributions, and it can be seen that there is still disagreement between data and MC in the areas where QCD would be expected to contribute. Further selection is, therefore, necessary.

 Number: 1 Author: ptd Subject: Inserted Text Date: 12/06/2016 15:05:56
While the

 Number: 2 Author: ptd Subject: Inserted Text Date: 12/06/2016 15:06:07

,

 Number: 3 Author: ptd Subject: Inserted Text Date: 12/06/2016 15:06:16

,

 Number: 4 Author: ptd Subject: Cross-Out Date: 12/06/2016 15:06:36

 Number: 5 Author: ptd Subject: Inserted Text Date: 12/06/2016 15:06:53
applied to

 Number: 6 Author: ptd Subject: Highlight Date: 12/06/2016 15:05:17
[insert half-space and "GeV" should be in mathrm]

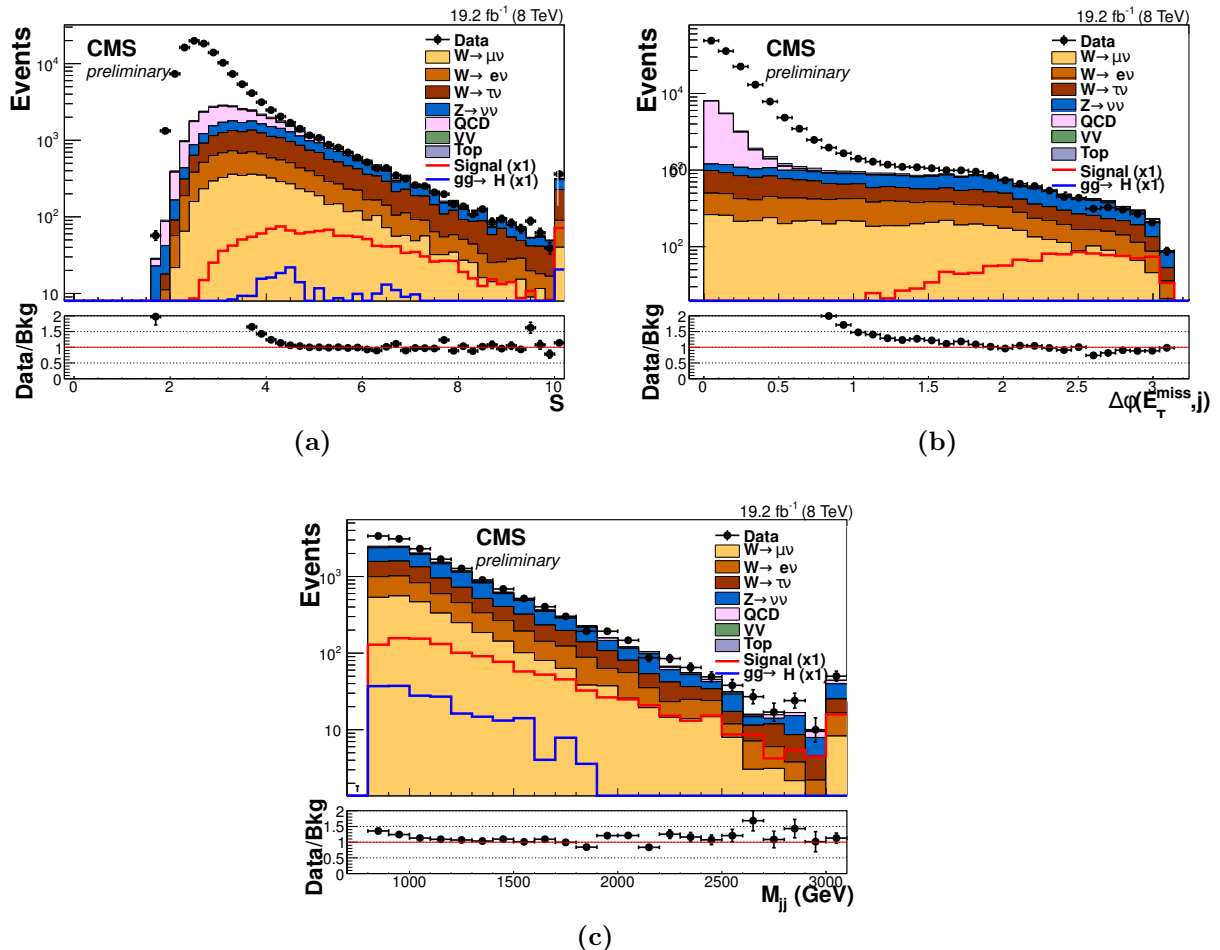


Figure 4.15.: (a) \mathcal{S} after the [1]gger driven selection described in Equation 4.11. (b) $\min\Delta\phi(j, \cancel{E}_T^{\text{no-}\mu})$ after the [2]gger driven selection and requiring $\mathcal{S} > 3$. (c) M_{jj} after the [3]gger driven selection and requiring $\mathcal{S} > 3$ and $\min\Delta\phi(j, \cancel{E}_T^{\text{no-}\mu}) > 1$. All three plots are of the signal-like region with the MC scaled using the background estimation methods described in Section 4.7. The disagreement between data and the predictions from background MC samples is believed to be due to mismeasured QCD multijet events which are not well modelled by the available MC samples. The last bin of each distribution contains the events above the range displayed. Signal ($gg \rightarrow H$) refers to an SM VBF (ggH) produced Higgs boson with $\mathcal{B}(H \rightarrow \text{inv}) = 100\%$.

Page: 88

 Number: 1 Author: ptd Subject: Highlight Date: 12/06/2016 15:07:35
trigger-driven

 Number: 2 Author: ptd Subject: Highlight Date: 12/06/2016 15:07:54

 Number: 3 Author: ptd Subject: Highlight Date: 12/06/2016 15:07:47

4.6.2. Signal region selection

As can be seen from Figure 4.16, there is still a significant difference between the data and the MC background prediction. It is also evident that the main areas where disagreement occurs are where contributions from QCD backgrounds (which are not included in the figure) would be expected to contribute, at low \mathcal{S} and low $\min\Delta\phi(j, \cancel{E}_T^{\text{no-}\mu})$, i.e. with jets close to the $\cancel{E}_T^{\text{no-}\mu}$. Outside these QCD-like regions good agreement between data and MC is seen, indicating very low numbers of QCD events remaining. The approach taken was to place tight requirements on these two variables to reduce the QCD background to be much smaller than the other backgrounds considered. The large uncertainty on any estimate of the number of events from QCD multijet processes therefore also became [1] negligible. A requirement that events have $\min\Delta\phi(j, \cancel{E}_T^{\text{no-}\mu}) > 2$ and $\mathcal{S} > 4$, was therefore imposed. The resulting relatively QCD-free “optimisation” region was blinded (i.e. the data were not looked at) to use for studies to determine the final signal region selection. All of the studies described in this chapter from this point until the results section were performed blind unless stated otherwise.

Two methods to select the signal region were investigated. The first method was a [2]it based selection. Starting from the optimisation region the cuts on \mathcal{S} , $\min\Delta\phi(j, \cancel{E}_T^{\text{no-}\mu})$, $\Delta\eta_{jj}$, sub-leading jet p_T and M_{jj} were varied one at a time and the expected limit for each combination of cuts was calculated. The method described in Section 1.4 was used, with the background estimation techniques and systematic uncertainties described in Sections 4.7 and 4.8 respectively, to calculate the expected limit. In the case of the QCD background, which has only a very small contribution to the signal region, the background estimation was performed once for the optimisation selection and used for all cut values. The estimations for all other background processes were repeated for each set of cuts. After each variable was varied the selection was updated to use the cut value that gave the best expected limit. After all the variables had been varied the process was repeated until no improvement in the expected limit was seen so as to avoid ignoring other better sets of cuts. The cut values that gave the best expected limit define the signal region and are as follows:

$$\begin{aligned} \eta_{j1} \cdot \eta_{j2} < 0, \Delta\eta_{jj} > 3.6, \text{ leading jet } \cancel{E}_T > 50 \text{ GeV}, \\ \text{sub-leading jet } \cancel{E}_T > 45 \text{ GeV}, M_{jj} > 1200 \text{ GeV}, \\ \cancel{E}_T^{\text{no-}\mu} > 90 \text{ GeV}, \mathcal{S} > 4.0, \min\Delta\phi(j, \cancel{E}_T^{\text{no-}\mu}) > 2.3. \end{aligned} \quad (4.13)$$

Page: 90

 Number: 1 Author: ptd Subject: Inserted Text Date: 12/06/2016 15:08:53
becomes

 Number: 2 Author: ptd Subject: Highlight Date: 12/06/2016 15:10:10
cut-based

 Number: 3 Author: ptd Subject: Highlight Date: 12/06/2016 15:11:02
italic "p"

 Number: 4 Author: ptd Subject: Highlight Date: 12/06/2016 15:10:37

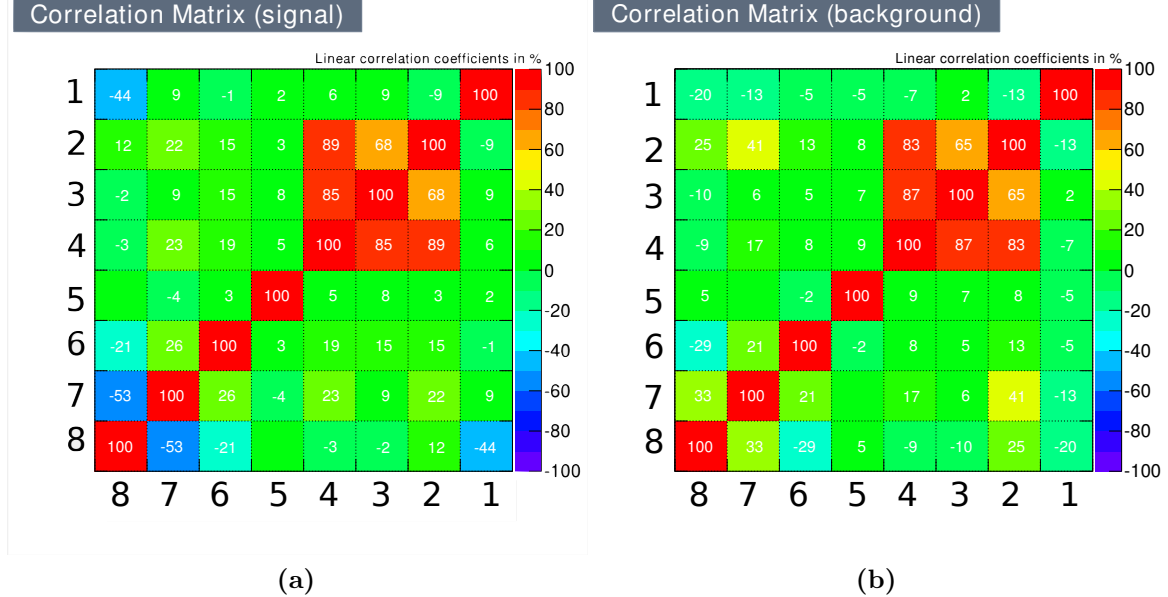


Figure 4.17.: Matrices of correlation coefficients for several variables in signal (a) and V+jets background (b) events passing the signal region selection. The variables are 1) the azimuthal angle difference between the $\vec{E}_T^{\text{no-}\mu}$ and the clustered energy in the event, 2) the square root of the hadronic energy in the event, 3) \mathcal{S} , 4) $\vec{E}_T^{\text{no-}\mu}$, 5) M_{jj} , 6) the number of jets with $p_T > 30$ GeV between the two tag jets in η , 7) the vectorial sum of the tag jets p_T and the $\vec{E}_T^{\text{no-}\mu}$, 8) the ratio between the magnitude of the vectorial sum of the tag jet's p_T and the $\vec{E}_T^{\text{no-}\mu}$.

After this selection was defined a second MVA based method of optimising the selection was investigated to see if we could improve on the cut based selection. BDT and Fisher discriminants were trained using signal and background events passing the signal region selection [87]. The signal selection was used as the basis for this training so as to ensure that the number of events from the QCD background in the studied region was small. The optimisation procedure defined above was then repeated with the value of the discriminant considered as an additional variable. One advantage of MVA based selection over simple rectangular based selection is that information about the correlation between variables is taken into account. The correlation coefficients between the variables used as inputs to the MVA are shown for signal and V+jets background events in Figure 4.17. These variables were chosen as they showed the most difference between signal and background distributions and correlations out of a wide range of variables investigated. Without the addition of any additional systematic uncertainties associated with the understanding of the variables input to the MVA, the largest improvement in the expected limit was less than 1%. It was therefore decided to use the based selection as the final event selection.

Page: 91

 Number: 1 Author: ptd Subject: Inserted Text Date: 12/06/2016 15:12:27
vector sum of the [?]

 Number: 2 Author: ptd Subject: Inserted Text Date: 12/06/2016 15:17:22
an alternative, MVA-based,

 Number: 3 Author: ptd Subject: Inserted Text Date: 12/06/2016 15:17:34
it

 Number: 4 Author: ptd Subject: Inserted Text Date: 12/06/2016 15:17:52
cut-based

 Number: 5 Author: ptd Subject: Inserted Text Date: 12/06/2016 15:22:21
Fisher
[after Ronald Fisher]

 Number: 6 Author: ptd Subject: Inserted Text Date: 12/06/2016 15:22:59
"optimisation" [if correct]

 Number: 7 Author: ptd Subject: Highlight Date: 12/06/2016 15:25:35
[hyphenate]

 Number: 8 Author: ptd Subject: Inserted Text Date: 12/06/2016 15:23:32
an

 Number: 9 Author: ptd Subject: Cross-Out Date: 12/06/2016 18:21:28
[technically, BDTs are rectangular as well...?]

 Number: 10 Author: ptd Subject: Highlight Date: 12/06/2016 15:26:01
[hyphenate]

 Number: 11 Author: ptd Subject: Inserted Text Date: 12/06/2016 15:27:59
a

 Number: 12 Author: ptd Subject: Inserted Text Date: 12/06/2016 15:30:09
considering any of the

 Number: 13 Author: ptd Subject: Highlight Date: 12/06/2016 15:26:29
[hyphenate]

4.7. Background estimation

After the full event selection the V+jets backgrounds, as in the prompt analysis, dominate. Also, as in the prompt analysis, contributions are expected from top quark and diboson related processes. Finally, whilst it is reduced significantly by the selection described above, it is also necessary to estimate the expected contribution from the very small number of remaining QCD multijet events.

The methods used to estimate the V+jets backgrounds are based on those used in the prompt analysis. Equation 4.2 is used in several of these methods in this section, and it is repeated here:

$$N_{Exp}^S = (N_{Data}^C - N_{Bkg}^C) \cdot \frac{N_{MC}^S}{N_{MC}^C}. \quad (4.14)$$

The terms on the right hand side of this equation which multiply the estimation from MC of the number of events due to a particular background process are often collectively referred to as the Data driven scale factor. The changes in event selection for this analysis necessitated several changes from the methods for the prompt analysis. The use of this Data driven method to investigate the top quark related background was also investigated. Furthermore, among other improvements, the systematic uncertainty on the $Z \rightarrow \nu\nu$ background was re-evaluated. All of these changes and improvements are described in this section.

4.7.1. Top quarks

Almost all top quarks decay to a W boson and a b quark. Top quarks are either created in pairs, or via “single top” production where only one top quark is created in association with other quarks or a W boson. Top pair production results in two W bosons and two b quarks. Single top production results in some combination of W bosons and quarks. Either single or pair production of top quarks can result in the appearance of \cancel{E}_T and jets with no leptons, if at least one of the W bosons decays leptonically and the lepton is misreconstructed. The resulting jets can coincidentally have VBF-like topology. Whilst the contribution from these processes is expected to be small in the signal region, making up around 1% of events there, the presence of W bosons and jets makes these processes very likely to contribute to the control regions used to estimate the W+jets background contribution. In the $W \rightarrow \tau\nu$ control region approximately 15% of events are estimated

Page: 92

T Number: 1 Author: ptd Subject: Highlight Date: 12/06/2016 15:57:45

[If what I suggest below is correct (let me know if not) please re-write accordingly, for improved clarity:

"The terms on the right-hand [hyphenate] side of this equation which multiply the estimation from MC (N^S_MC) of the number of events due to a particular background process in the signal region are often..."]

T Number: 2 Author: ptd Subject: Highlight Date: 12/06/2016 15:42:25

data-driven

[Earlier in the thesis you hyphenated data-driven correctly. However, here, and many times after this, you use data-driven as an adjective but forget about hyphenating. Please find all such occurrences and hyphenate.]

T Number: 3 Author: ptd Subject: Highlight Date: 12/06/2016 15:37:49

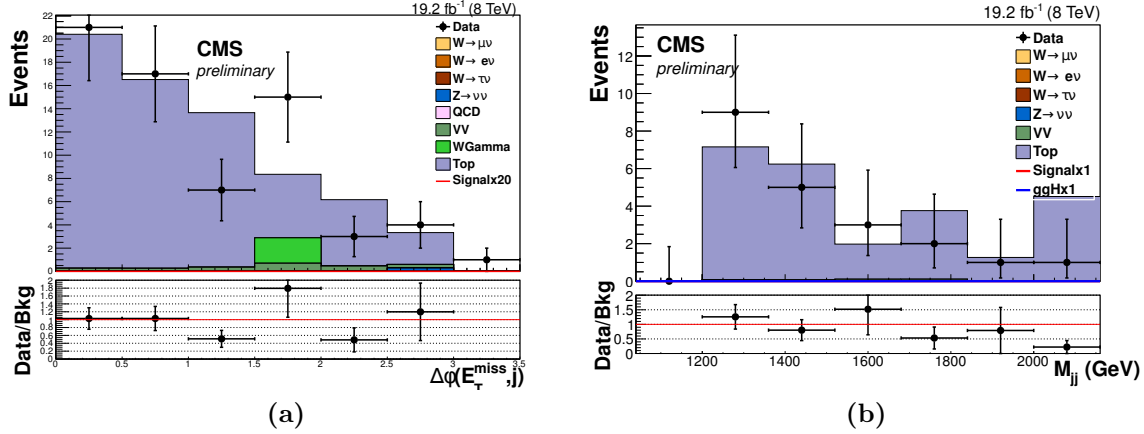


Figure 4.18.: The distribution of $\min\Delta\phi(j, \cancel{E}_T^{\text{no-}\mu})$ (a) and M_{jj} (b) in the top control region with one tight electron and one tight muon. The last bin of each distribution contains the events above the range displayed.

to come from top quark processes. Data driven methods for estimating the top quark background and its uncertainties were therefore investigated.

Initially, a dilepton control region was investigated. This had the same cuts on the jet and \cancel{E}_T related variables as the signal region, but the lepton veto was replaced with a requirement that there is exactly one tight electron and one tight muon. This final state would be expected in the case of top quark pair production or single top production with a W boson, where both the resulting W bosons decay leptonically to different flavour leptons. This region had only single figure numbers of events expected, so the cut on $\min\Delta\phi(j, \cancel{E}_T^{\text{no-}\mu})$ was loosened to 0. It can be seen from Figure 4.18 that the ratio between data and MC in this region does not depend significantly on $\min\Delta\phi(j, \cancel{E}_T^{\text{no-}\mu})$. The data driven scale factor obtained from this dilepton region was, within the statistics available, consistent with 1 and a good agreement between data and MC was seen in all variables studied. A modification of this control region where events with either two tight electrons or two tight muons, and no other leptons were selected was also studied. This final state would also be expected where two W bosons from top quark production decayed leptonically, except this time to the same flavour of lepton. In order to avoid Z boson contributions the leptons' invariant mass was required to be incompatible with that of a Z boson, i.e. outside of the range from 60 to 120 GeV. This control region also yielded good data-MC agreement and a scale factor compatible with 1.

An issue with both of these control regions is that the ratio of pair production to single top quark production is very different from both the signal region and the $W \rightarrow \tau\nu$ control region. MC estimations indicate that these top control regions have a negligible

Page: 93

 Number: 1 Author: ptd Subject: Highlight Date: 12/06/2016 15:37:54

 Number: 2 Author: ptd Subject: Highlight Date: 12/06/2016 15:38:09

single top contribution, while the top background in the signal region has almost no top quark pair contribution. The $W \rightarrow \tau\nu$ region is expected to be a mixture, its top quark background being 30% from single top events and 70% for top quark pairs, again estimated from MC. A single top control region was therefore also investigated.

The single top region differed from the signal region in that the $\min\Delta\phi(j, \cancel{E}_T^{\text{no-}\mu})$ cut was removed, exactly one tight electron or muon was required, further leptons were vetoed and one of the tag jets was required to be compatible with being a b-jet. The restriction to a single lepton significantly reduces the top quark pair production contribution where both resulting W bosons decay leptonically, and the requirement of one b-jet reduces the W+jets contribution.

Identification of the b-jet was done using the combined secondary vertex (CSV) discriminant [103]. B quarks are both heavier and longer lived than many other particles created at the LHC, meaning that their secondary decay vertex can be distinguished from the PV. CSV is an MVA based discriminant which uses information on secondary vertices and the lifetime of the particle to discriminate between jets from b quarks and those from light quarks. The medium working point used for this control region has an efficiency of approximately 85% for b-quarks and mis-identifies light quark jets as b jets approximately 1% of the time.

MC estimates indicate the single top region is 17% single top. This region again showed good data-MC agreement (as can be seen in Figure 4.19) and a scale factor compatible with 1 within uncertainties. Because good agreement between data and MC and scale factors compatible with 1 are seen in all investigated control regions, it was decided to use the MC prediction for the top background in all regions with no additional scale factor. A 20% systematic uncertainty was applied to this prediction which covered the largest deviation from 1 seen in the scale factors from the various control regions.

4.7.2. $W \rightarrow e\nu + \text{jets}$

The $W \rightarrow e\nu$ background in the parked data analysis is estimated using the same method as that used for the prompt analysis based on equation 4.14. The control region used has the same requirements as the signal region, except that the electron veto is replaced with a requirement that there is one tight electron and no other electrons present in the event. The requirement of an electron removes signal events and enriches the region in $W \rightarrow e\nu$ events. The distributions of several variables in data and MC (which has been

 Number: 1 Author: ptd Subject: Inserted Text Date: 12/06/2016 15:59:50
)

 Number: 2 Author: ptd Subject: Inserted Text Date: 12/06/2016 15:59:38
(see

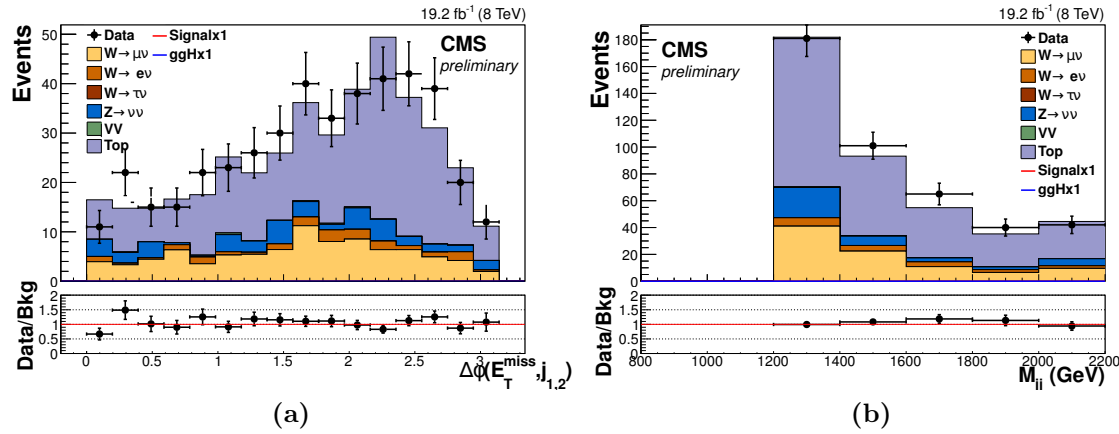


Figure 4.19.: The distribution of $\min\Delta\phi(j_{1/2}, \cancel{E}_T^{\text{no-}\mu})$ (a) and M_{jj} (b) in the single top control region. The last bin of each distribution contains the events above the range displayed.

Table 4.10.: The inputs to, and results of, Equation 4.14, when used to estimate the $W \rightarrow e\nu$ estimate in the signal region.

	Signal region	Control region
N_{Data}	N/A	68 ± 8.2 (stat)
N_{Bkg}	N/A	3.5 ± 1.2 (MC stat)
N_{MC}	114.9 ± 8.9 (MC stat)	128.0 ± 8.0 (MC stat)
$\frac{N^{data} - N^{bkg}}{N^{MC}}$	0.50 ± 0.06 (stat) ± 0.03 (MC stat)	
$N_{W \rightarrow e\nu}$	57.9 ± 7.4 (stat) ± 7.7 (syst)	N/A

scaled by the **Data driven** scale factor extracted from this control region) are shown in Figure 4.20, where good agreement can be seen. A table of the inputs to, and results of, Equation 4.14 can be seen in Table 4.10. The table also shows that the expected contribution to this region from other background processes is small, being approximately 5%. The scale factor obtained for this background is 0.5, which is significantly different from 1, this difference is further investigated in Section 4.7.8.

4.7.3. $W \rightarrow \mu\nu + \text{jets}$

As for the $W \rightarrow e\nu$ background the $W \rightarrow \mu\nu$ background is estimated using Equation 4.14 with a control region enriched in $W \rightarrow \mu\nu$ events through a change in lepton requirements. The control region used has the same requirements as the signal region, but with the

Page: 95

 Number: 1 Author: ptd Subject: Highlight Date: 12/06/2016 16:03:36
[should this be simply "N^C_MC"?]

 Number: 2 Author: ptd Subject: Highlight Date: 12/06/2016 15:38:17

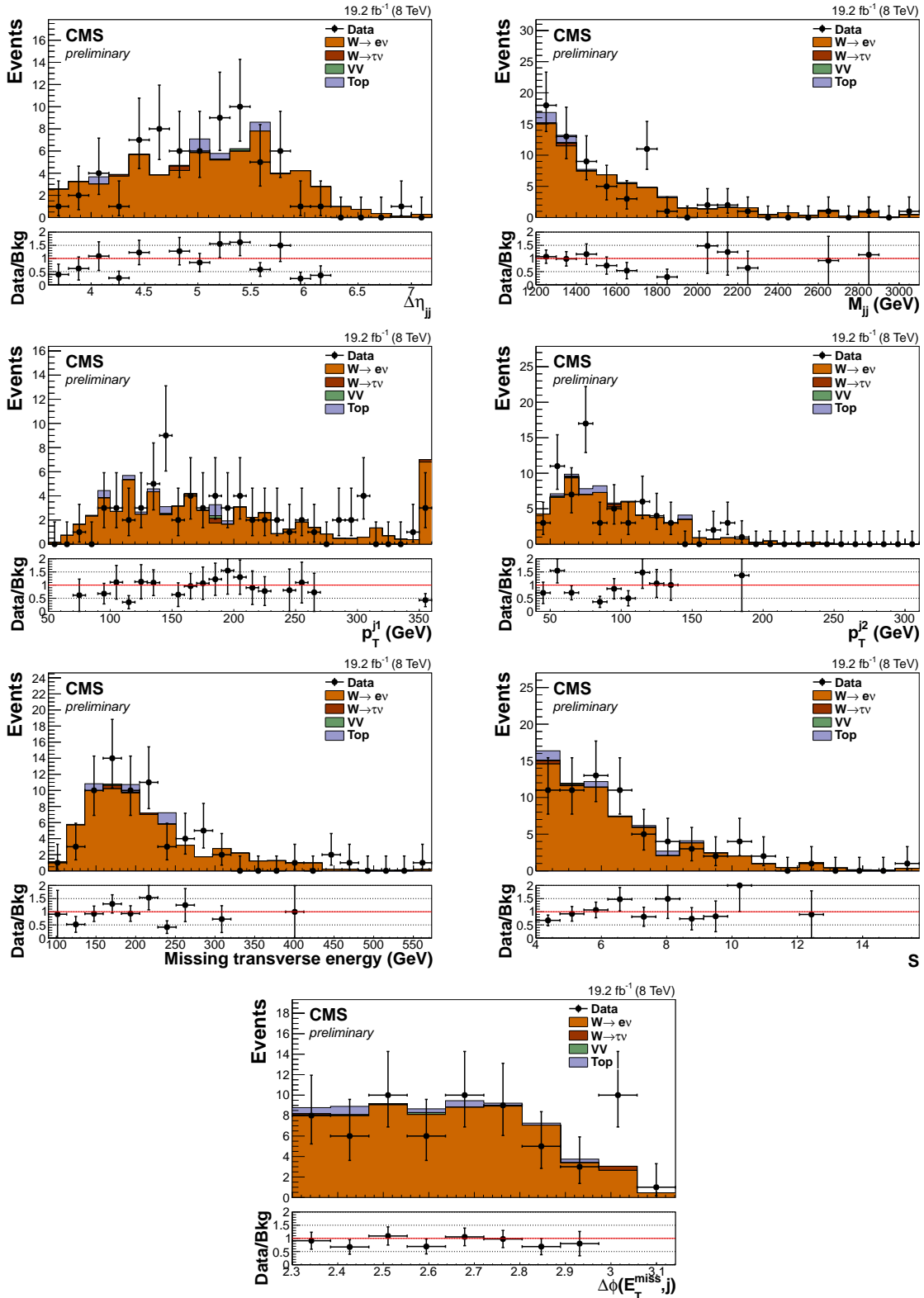


Figure 4.20.: Distributions of variables in data and MC events in the $W \rightarrow e\nu$ control region. MC events from V+jets backgrounds are scaled by their data-driven scale factors. The variables shown are from top to bottom and left to right: $\Delta\eta_{jj}$, M_{jj} , the leading and sub-leading jet's p_T , $E_T^{\text{no-}\mu}$, S and $\min\Delta\phi(j, E_T^{\text{no-}\mu})$. The last bin of each distribution contains the events above the range displayed [2].

 Number: 1 Author: ptd Subject: Cross-Out Date: 12/06/2016 17:32:40
[please fix here, as well as in Figs. 4.21, 4.22 and 4.24.]

 Number: 2 Author: ptd Subject: Inserted Text Date: 12/06/2016 17:32:53
:

[please fix here, as well as in Figs. 4.21, 4.22 and 4.24.]

muon veto replaced with a requirement that there is one tight muon and no other muons present in the event. The distributions of several variables in data and MC (which has been scaled by the **1**ata driven scale factor extracted from this control region) are shown in Figure 4.21, where good agreement can be seen. A table of the inputs to, and results of, Equation 4.14 can be seen in Table 4.11. The contribution from other backgrounds in the $W \rightarrow \mu\nu$ control region is approximately 5%. Again the scale factor obtained for this background is significantly different from 1, being 0.71, and further investigation of this is detailed in Section 4.7.8. Furthermore, the estimated contribution from this background is very different to that expected from $W \rightarrow e\nu$, an investigation of this difference is described in Section 4.7.5.

Table 4.11.: The inputs to, and results of, Equation 4.14, when used to estimate the $W \rightarrow \mu\nu$ estimate in the signal region.

	Signal region	Control region
N_{Data}	N/A	300 ± 17.3 (stat)
N_{Bkg}	N/A	14.8 ± 2.5 (MC stat)
N_{MC}	143.7 ± 10.2 (MC stat)	399.9 ± 14.9 (MC stat)
$\frac{N_{Data}^{data} - N_{Bkg}^{bkg}}{N_{Bkg}}$	0.71 ± 0.04 (stat) ± 0.03 (MC stat)	
$N_{W \rightarrow \mu\nu}$	102.5 ± 6.2 (stat) ± 11.7 (syst)	N/A

4.7.4. $W \rightarrow \tau\nu + \text{jets}$

The signal region requirements do not include a veto of hadronic taus, due to the low identification efficiency and relatively high probability for a jet to be identified as a fake tau. Requiring that there is an identified hadronic tau in addition to the signal region selection results in **a region containing** **3** only 2 data events. In order to increase the number of events in the tau control region the $\min\Delta\phi(j, \cancel{E}_T^{\text{no-}\mu})$ cut was removed. The requirement that there is an identified tau reduces the QCD multijet contribution in the low $\min\Delta\phi(j, \cancel{E}_T^{\text{no-}\mu})$ region significantly compared to what was seen during the choice of the preselection. However, poor data-MC agreement was still observed in the $\min\Delta\phi(j, \cancel{E}_T^{\text{no-}\mu}) < 1$ region, which is evidence that some events from multijet processes are still present. To remove these QCD multijet events, whilst keeping a reasonable number of events in the resulting control region, a requirement that $\min\Delta\phi(j_{1/2}, \cancel{E}_T^{\text{no-}\mu})$ is greater than 1 and that the transverse mass of the hadronic tau and \cancel{E}_T system is

Page: 97

 Number: 1 Author: ptd Subject: Highlight Date: 12/06/2016 15:38:27

 Number: 2 Author: ptd Subject: Highlight Date: 12/06/2016 17:16:51
N^C_MC

[superscript and subscript are the wrong way around; please fix in Table 4.12 as well]

 Number: 3 Author: ptd Subject: Inserted Text Date: 12/06/2016 17:16:12
selecting

greater than 20 GeV is applied. The $\min\Delta\phi(j_{1/2}, \cancel{E}_T^{\text{no-}\mu})$ requirement reduces QCD backgrounds for the same reason that $\min\Delta\phi(j, \cancel{E}_T^{\text{no-}\mu})$ does, but it is a slightly looser requirement as it only considers the two leading jets. The transverse mass of the tau- \cancel{E}_T system is a good variable to reject QCD where a lepton is present as in real W boson events the tau and \cancel{E}_T are expected to originate from the same object and therefore have significant invariant mass, which is not the case for QCD multijet events.

After the anti-QCD cuts the agreement between data and MC is good as can be seen in Figure 4.22. To account for the different $\min\Delta\phi(j, \cancel{E}_T^{\text{no-}\mu})$ selection in this region and the signal region, the **data driven** scale factor was calculated both in the $W \rightarrow \mu\nu$ control region, which has the signal region $\min\Delta\phi(j, \cancel{E}_T^{\text{no-}\mu})$ selection, and in a modified single muon control region with the $W \rightarrow \tau\nu$ control region $\min\Delta\phi(j, \cancel{E}_T^{\text{no-}\mu})$ selection. The difference between these two scale factors was found to be 20%, so a 20% systematic uncertainty was added to the estimate of the $W \rightarrow \tau\nu$ background.

The single tau control region with a $\min\Delta\phi(j_{1/2}, \cancel{E}_T^{\text{no-}\mu})$ cut and no $\min\Delta\phi(j, \cancel{E}_T^{\text{no-}\mu})$ cut was used with Equation 4.14 to estimate the number of $W \rightarrow \tau\nu$ events in the signal region. A table of the inputs to, and results of, Equation 4.14 can be seen in Table 4.12. The contribution from other backgrounds in the $W \rightarrow \tau\nu$ control region is approximately 15%, with most of these other background events being due to top quark related processes. The scale factor obtained for this background is 0.78, which is closer to 1 than those seen in the other W+jets backgrounds, however it also has the largest uncertainty. Further investigation of the V+jets scale factors is detailed in Section 4.7.8.

Table 4.12.: The inputs to, and results of, Equation 4.14, when used to estimate the $W \rightarrow \tau\nu$ estimate in the signal region.

	Signal region	Control region
N_{Data}	N/A	76 ± 8.7 (stat)
N_{Bkg}	N/A	13.3 ± 2.8 (MC stat)
N_{MC}	121.9 ± 8.7 (MC stat)	80.8 ± 6.4 (MC stat)
$\frac{N_{Data} - N_{Bkg}}{N_C^{MC}}$	0.78 ± 0.11 (stat) ± 0.07 (MC stat)	
$N_{W \rightarrow \mu\nu}$	94.6 ± 13.1 (stat) ± 23.8 (syst)	N/A

4.7.5. Differences between the $W \rightarrow e\nu$, $W \rightarrow \mu\nu$ and $W \rightarrow \tau\nu + \text{jets}$ backgrounds

The number of $W + \text{jets}$ events decaying to a particular flavour of lepton with VBF-like jet kinematics should be the same for all three flavours of lepton through lepton universality. Differences between the numbers of background events from $W \rightarrow e\nu$, $W \rightarrow \mu\nu$ and $W \rightarrow \tau\nu$ must therefore be due to differences in the identification of the leptons. Hadronic taus have much lower identification efficiencies than the other two flavours of leptons, so might naively be expected to give rise to a much larger number of background events. However, due to the similarities between hadronic taus and jets, unidentified taus often lead to additional jets in the event and therefore increase the probability that an event will fail the $\min\Delta\phi(j, \cancel{E}_T^{\text{no-}\mu})$ cut [91]. These two competing effects mean that the number of background events from $W \rightarrow \tau\nu$ passing the signal region selection is not necessarily expected to be the same as that from $W \rightarrow e\nu$ and $W \rightarrow \mu\nu$.

By contrast, electrons and muons have much more similar identification efficiencies (see Sections 3.4 and 3.5). The 45% difference seen in the number of expected background events from these two processes was therefore unexpected. This difference was also not seen in the prompt analysis, as can be seen from Table 4.8. The prediction of the $W \rightarrow e/\mu\nu$ backgrounds is made up of a **data driven** scale factor and an estimate from MC of the number of events from the process expected ^[1] in the signal region, N_{MC}^S . Both these elements were studied to try to understand the observed differences.

Firstly, the **data driven** scale factors for the electron and muon backgrounds differ by 30%, which is not sufficient to explain the full difference between the electron and muon background estimates. Furthermore, when systematic errors are taken into account this difference is only approximately one standard deviation. On the other hand, N_{MC}^S does show a significant difference.

To study the difference in N_{MC}^S two sub-regions of the signal region were studied, that with a generator level lepton inside the detector acceptance for both electrons and muons ($|\eta| < 2.1$), and that with a generator lepton outside the detector acceptance for both electrons and muons ($|\eta| > 2.4$). The number of events in these two sub-regions from both $W \rightarrow e\nu$ and $W \rightarrow \mu\nu$ MC can be seen in Table 4.13. The numbers of events with a generator level lepton inside acceptance are approximately one standard deviation higher for electrons. This small difference is expected due to the lower identification efficiency for veto leptons making them less likely to cause an event to fail the lepton

Page: 101

 Number: 1 Author: ptd Subject: Highlight Date: 12/06/2016 15:38:43

 Number: 2 Author: ptd Subject: Highlight Date: 12/06/2016 15:38:53

 Number: 3 Author: ptd Subject: Inserted Text Date: 12/06/2016 17:23:40

|

4.7.6. $Z \rightarrow \nu\nu + \text{jets}$

The irreducible $Z \rightarrow \nu\nu$ background is estimated using a very similar method to that used in the prompt analysis (Section 4.2.4). A reminder of the method highlighting the differences from the prompt analysis is given here.

The method starts by defining a dimuon control region by taking the signal region requirements and replacing the muon veto with the requirement that there are two tight muons with invariant mass compatible with a Z boson, i.e. between 60 and 120 GeV, and no other muons in the event. The number of events in this dimuon control region is then extrapolated to the signal region using efficiencies and cross-section ratios calculated using MC events. As in the prompt analysis ^[1] $Z/\gamma^* \rightarrow \mu\mu$ MC sample with the reconstructed leptons ignored and a requirement that there is a generator level dimuon system with invariant mass between 80 and 100 GeV (i.e. compatible with a Z boson) is used to estimate the contribution in the signal region from $Z \rightarrow \nu\nu$ processes. The mass window used here is tighter than that used to define the dimuon control region because the generator level lepton p_T resolution is better than that of reconstructed leptons. $Z \rightarrow \nu\nu$ MC events are not used for this estimation due to the limited size of the available $Z \rightarrow \nu\nu$ MC samples. Whilst the number of events in the dimuon control region is small the agreement between data and MC is good as can be seen from Figure 4.24 ^[2]

The formulae used to carry out the extrapolation from the control region to the signal region are given in Equation 4.3 which is repeated here for reference:

$$N_{Exp}^S = (N_{Data}^C - N_{Bkg}^C) \cdot \frac{\sigma(Z \rightarrow \nu\nu)}{\sigma(Z/\gamma^* \rightarrow \mu\mu)} \cdot \frac{\epsilon_{VBF}^S}{\epsilon_{VBF}^C}, \quad (4.15)$$

where ϵ^S and ϵ^C are calculated as in Equations 4.4 and 4.5 repeated here:

$$\epsilon_{VBF}^S = \frac{\sigma(Z \rightarrow \nu\nu, EWK) \frac{N_{MC}^S(EWK)}{N_{gen}(Zmass,EWK)} + \sigma(Z \rightarrow \nu\nu, QCD) \frac{N_{MC}^S(QCD)}{N_{gen}(Zmass,QCD)}}{\sigma(Z \rightarrow \nu\nu, EWK) + \sigma(Z \rightarrow \nu\nu, QCD)}, \quad (4.16)$$

$$\epsilon_{VBF}^C = \frac{\sigma(Z/\gamma^* \rightarrow \mu\mu, EWK) \frac{N_{MC}^C(EWK)}{N_{gen}(EWK)} + \sigma(Z/\gamma^* \rightarrow \mu\mu, QCD) \frac{N_{MC}^C(QCD)}{N_{gen}(QCD)}}{\sigma(Z/\gamma^* \rightarrow \mu\mu, EWK) + \sigma(Z/\gamma^* \rightarrow \mu\mu, QCD)}. \quad (4.17)$$

As the $Z/\gamma^* \rightarrow \mu\mu$ and $Z \rightarrow \nu\nu$ cross-sections are calculated before the analysis selection cuts and do not depend on detector calibration, the same values are used as in the prompt analysis shown in Table 4.4. The other inputs to the above equations and the results of the estimation are shown in Table 4.14.

Page: 104

 Number: 1 Author: ptd Subject: Inserted Text Date: 12/06/2016 17:29:07

 Number: 2 Author: ptd Subject: Inserted Text Date: 12/06/2016 17:29:21

Table 4.14.: The inputs to Equations 4.15, 4.16 and 4.17 and the final estimate of the $Z \rightarrow \nu\nu$ background in the signal region for the parked data analysis. Also shown for comparison is the ratio between the MC prediction of the number of $Z/\gamma^* \rightarrow \mu\mu$ events in the control region and the number of data events in the control region. The systematic uncertainties quoted include MC statistical uncertainties and all sources listed in Section 4.8.

$N_{gen}(EWK)$	5781.9	
$N_{gen}(\text{Zmass}, EWK)$	4226.5	
$N_{gen}(QCD)$	22789000	
$N_{gen}(\text{Zmass}, QCD)$	20334000	
<hr/>		
	Signal region	Control region
N_{Data}	N/A	$18 \pm 4.2 \text{ (stat)}$
N_{Bkg}	N/A	$0.2 \pm 0.1 \text{ (MC stat)}$
$N_{MC}(EWK)$	$7.9 \pm 0.2 \text{ (MC stat)}$	$6.0 \pm 0.2 \text{ (MC stat)}$
$N_{MC}(QCD)$	$29.5 \pm 3.0 \text{ (MC stat)}$	$20.5 \pm 2.5 \text{ (MC stat)}$
$\frac{N_{Data}^C - N_{Bkg}^C}{N_{MC}(EWK) + N_{MC}(QCD)}$	$0.67 \pm 0.16 \text{ (stat)} \pm 0.06 \text{ (MC stat)}$	
$N_{Z \rightarrow \nu\nu/Z \rightarrow \gamma^* \rightarrow \mu\mu}$	$158.1 \pm 37.8 \text{ (stat)} \pm 21.2 \text{ (syst)}$	$17.8 \pm 4.2 \text{ (stat)} \pm 0.1 \text{ (MC stat)}$

Although it is not used in the $Z \rightarrow \nu\nu$ background estimation method, the ratio between the number of MC dimuon events, both from electroweak and QCD events, and the number of data events minus expected backgrounds from other processes is shown for comparison with the **data driven** scale factors used in the W+jets background estimate. The ratio is, like those in the W+jets background estimation found to be significantly different from 1.

In the prompt analysis one of the largest uncertainties, being 44% of the size of the total systematic uncertainty on the total background estimate, was the uncertainty on the ratio between the $Z/\gamma^* \rightarrow \mu\mu$ and $Z \rightarrow \nu\nu$ cross-sections in the VBF phase space. To reduce this uncertainty in this analysis the cross-section ratio was calculated both with **MADGRAPH** and **AMCNLO_MG5**. The **AMCNLO_MG5** calculation was carried out by generating both $Z/\gamma^* \rightarrow \mu\mu$ and $Z \rightarrow \nu\nu$ events and calculating the ratio of the efficiencies of events in each sample to pass the analysis selection. The selection was applied to generator level objects, with jets being constructed using the algorithm described in Section 3.6 from the generator level quarks and gluons, and the \cancel{E}_T being taken to be the Z boson's p_T . For the **MADGRAPH** calculation, the same

generator level selection was applied to the $Z/\gamma^* \rightarrow \mu\mu$ samples that are used in the background estimation method and the small available $Z \rightarrow \nu\nu$ sample and the same efficiency ratio was calculated. Within statistical errors (4% for MADGRAPH and 15% for AMCNLO_MG5) the ratios from the two generators were found to be compatible. As there was no evidence for a non-statistical discrepancy between the two, the statistical uncertainty from the MADGRAPH calculations was used as the uncertainty on this ratio. As the samples used for the MADGRAPH calculation are the same as those used in the background estimation method this error is already accounted for by the MC statistical uncertainty on the numbers of events in the $Z/\gamma^* \rightarrow \mu\mu$ sample predicted to be in the signal and control regions and no additional error is necessary.

4.7.7. V+jets consistency tests

To check the consistency of the scale factors obtained from the different V+jets background estimation methods, a study was undertaken to use the single muon control region scale factor to predict the data yield in the other control regions. Rather than calculate a single scale factor for the control region, as was done in the background estimation methods, scale factors were calculated for each bin of the distribution of several variables. These scale factors were then applied to the MC estimate in the corresponding bin of the other control regions, allowing the behaviour of the scale factor as a function of the variable to be seen. The resulting estimate was compared to the data yield minus the background expected from other processes from MC.

The scale factor weighted MC was found to agree better with data than the unweighted MC, with the differences seen between the weighted MC and the data being less than systematic uncertainty in the majority of bins, which gives confidence that the Data driven methods improve the background estimations. The results of these studies in the $E_T^{\text{no-}\mu}$ distribution can be seen in Figure 4.25.

4.7.8. V+jets scale factor investigations

The Data driven scale factors seen in the V+jets background estimation methods are consistently significantly different from 1. To investigate the reason for this difference the variation of the scale factors as a function of the analysis selection criteria was studied. Due to the high thresholds of the triggers with which the parked data were collected, it was necessary to use a different trigger for this study. The particular trigger chosen was

Page: 107

 Number: 1 Author: ptd Subject: Highlight Date: 12/06/2016 15:39:04

 Number: 2 Author: ptd Subject: Highlight Date: 12/06/2016 15:39:10

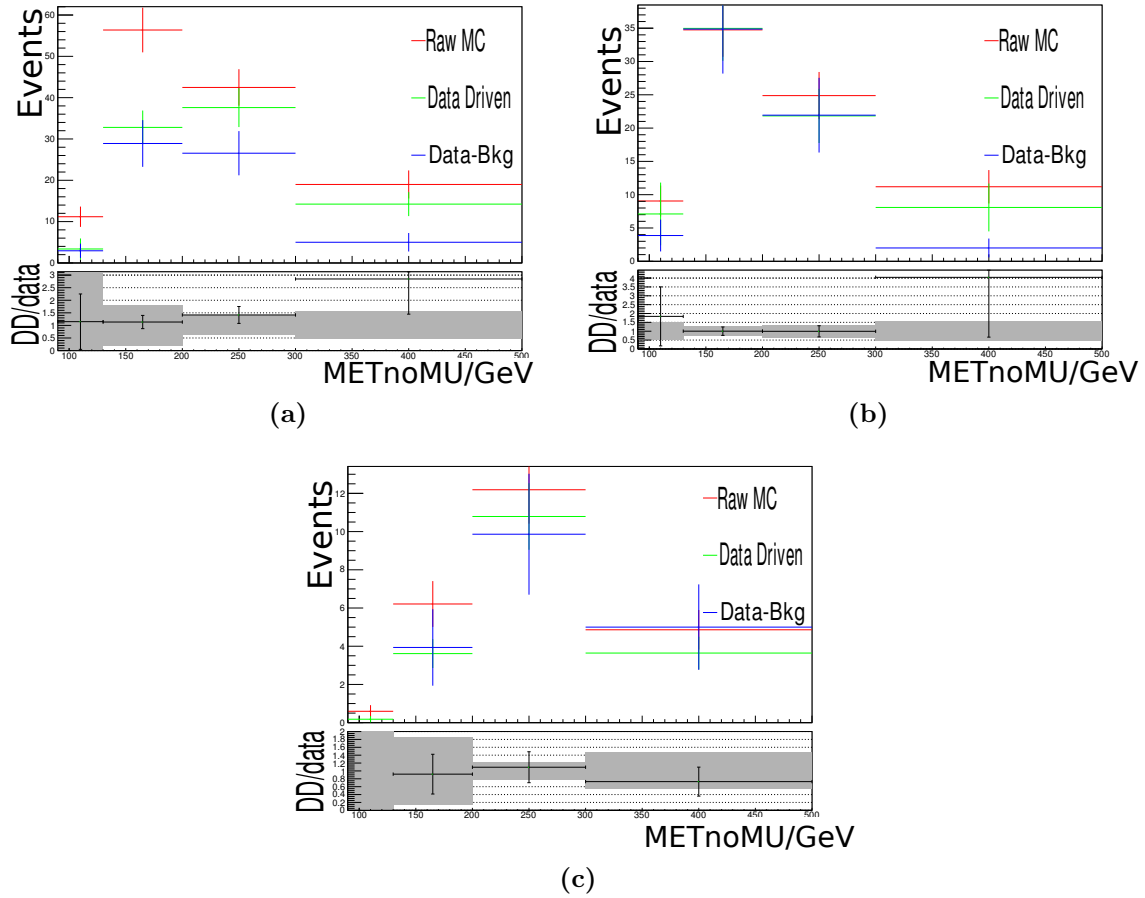


Figure 4.25.: The distribution of $\cancel{E}_T^{\text{no-}\mu}$ expected in the single electron (a), single tau (b) and dimuon control regions (c) from MC (red), data minus other background processes (blue) and MC weighted by the **5**ata driven scale factor calculated for each bin of the $\cancel{E}_T^{\text{no-}\mu}$ distribution in the single muon control region as described in Section 4.7.7 (green). The lower plot shows the ratio between the **6**ata driven scale factor weighted MC and the data minus other background processes. The grey band on the lower plots represents the systematic uncertainty from all sources described in Section 4.8.

Page: 108

 Number: 1 Author: ptd Subject: Highlight Date: 12/06/2016 15:39:46

 Number: 2 Author: ptd Subject: Highlight Date: 12/06/2016 15:39:38

 Number: 3 Author: ptd Subject: Highlight Date: 12/06/2016 15:39:31

 Number: 4 Author: ptd Subject: Highlight Date: 12/06/2016 15:39:24

 Number: 5 Author: ptd Subject: Highlight Date: 12/06/2016 15:39:18

 Number: 6 Author: ptd Subject: Highlight Date: 12/06/2016 15:40:01

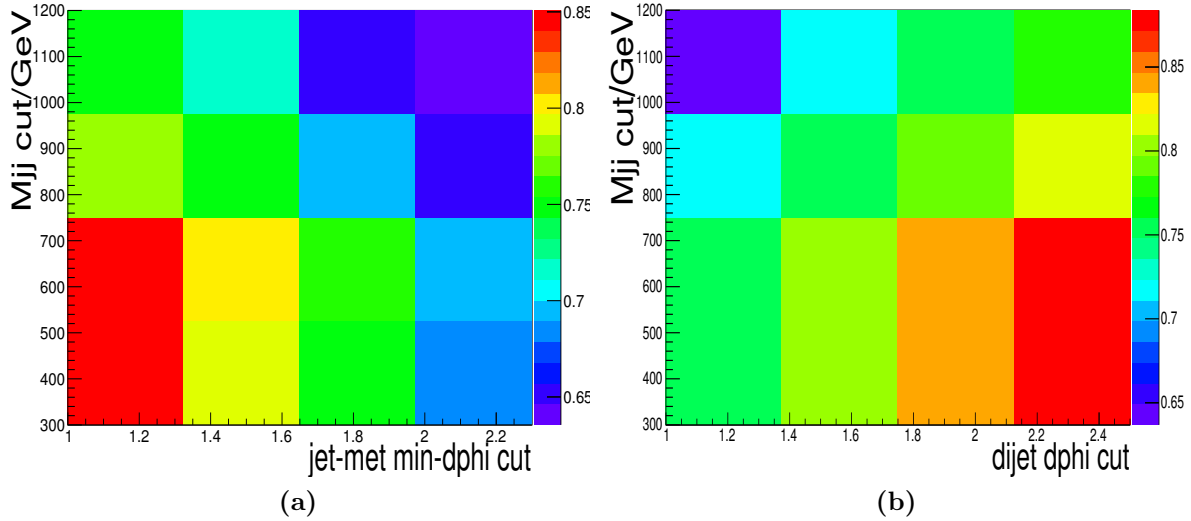


Figure 4.26.: The **data driven** scale factor obtained from a single muon control region, as described in Section 4.7.8, as a function of the cuts on $\min\Delta\phi(j, \cancel{E}_T^{\text{no-}\mu})$ and M_{jj} (a) and $\Delta\phi_{jj}$ and M_{jj} (b). It is important to note that the requirement on $\Delta\phi_{jj}$ is that the event have a value lower than the cut threshold, so the requirement is tighter to the left of the plot. The parked data analysis preselection requirements correspond to the top right bin of (a).

the same single muon trigger used for the trigger efficiency measurements described in Section 4.5. The study was therefore restricted to the single muon control region as it has muons present and contains significantly more events than the dimuon control region. To ensure that the trigger was fully efficient the muon p_T cut was tightened to 25 GeV.

The requirements on the leading and sub-leading jet's p_T , M_{jj} , $\min\Delta\phi(j, \cancel{E}_T^{\text{no-}\mu})$, $\cancel{E}_T^{\text{no-}\mu}$ and \mathcal{S} were then varied to ascertain which requirements caused the largest variations in the scale factor. The $\cancel{E}_T^{\text{no-}\mu}$ and leading jet p_T requirements were found to have no discernible effect on the scale factor. The effects from the sub-leading jet p_T and \mathcal{S} requirements were found to be less than 5%. By contrast, the $\min\Delta\phi(j, \cancel{E}_T^{\text{no-}\mu})$ and M_{jj} requirements were found to significantly alter the scale factor obtained. As can be seen in Figure 4.26a, when these two requirements are loosened the scale factor increases significantly.

To determine whether the scale factor depends more strongly on the jet or $\cancel{E}_T^{\text{no-}\mu}$ azimuthal angle the requirement on $\min\Delta\phi(j, \cancel{E}_T^{\text{no-}\mu})$ was replaced with a requirement on the difference in azimuthal angle between the two tag jets, $\Delta\phi_{jj}$, which doesn't depend on the $\cancel{E}_T^{\text{no-}\mu}$ and the study was repeated. As can be seen in Figure 4.26b, the scale factor was still found to vary in the same range with $\Delta\phi_{jj}$, indicating that the use of the $\cancel{E}_T^{\text{no-}\mu}$

azimuthal angle does not cause a further deviation from 1 than that present already due to jet related effects.

The looser the requirements on the jet kinematics are the closer the scale factor is to 1. It therefore seems that the deviation in the scale factor from 1 is caused by mismodelling of the **[1]t related** variables in V+jets MC. The distributions of variables for events in the various control regions shown in Figures 4.20-4.24 show good shape agreement between data and MC, indicating that the shape in these regions is not significantly mismodelled. Also, the **[2]ata driven** methods used to estimate the V+jets background correct for the overall normalisation difference from mismodelling in areas of phase space outside the analysis control and signal regions. For these two reasons this mismodelling is not expected to cause problems for the analysis.

4.7.9. QCD

As mentioned in Section 4.6 events from QCD multijet processes are very difficult to model using MC, as their high production cross-section and low probability to pass the selection cuts makes the number of events which must be generated prohibitively large. In an attempt to circumvent this problem a dedicated sample of QCD multijet events with VBF-like cuts imposed at generator level was produced. Specifically, the \cancel{E}_T was required to be greater than 40 GeV, at least 2 jets with $p_T > 20$ within the detector acceptance had to be present, and at least one pair of those jets was then required to have $M_{jj} > 700$ GeV and $\Delta\eta_{jj} > 3.2$. As can be seen from Figure 4.15 this sample does not adequately describe the events passing the trigger selection.

To investigate where this mismodelling comes from the reconstructed \cancel{E}_T was plotted as a function of the generator level \cancel{E}_T in the QCD multijet MC sample centrally produced by CMS as shown in Figure 4.27. This sample does not have any generator level cuts on the \cancel{E}_T or jet kinematics. Most events fall in the bottom left of this plot, having low \cancel{E}_T at both generator level and offline. These events would therefore not enter the analysis signal region and would also be rejected by the generator level cut as intended. There is then another class of events distributed around the diagonal of the plot due to the \cancel{E}_T resolution, with higher values of both generator level and offline \cancel{E}_T . These on-diagonal events would be expected to be well modelled by the VBF QCD sample as most of them which fall into the analysis signal region, which requires $\cancel{E}_T > 90$ GeV, would be expected to pass the generator level cut. Finally, there is a third type of events, which have low values of generator level \cancel{E}_T , but high values of offline \cancel{E}_T due to

Page: 110

 Number: 1 Author: ptd Subject: Highlight Date: 12/06/2016 17:34:11
jet-related

 Number: 2 Author: ptd Subject: Highlight Date: 12/06/2016 15:40:12

is determined, (ii) the “3-jet” region where this shape is validated, and (iii) a set of “sideband” regions where a normalisation for the QCD shape is extracted. A schematic of these regions is shown in Figure 4.28

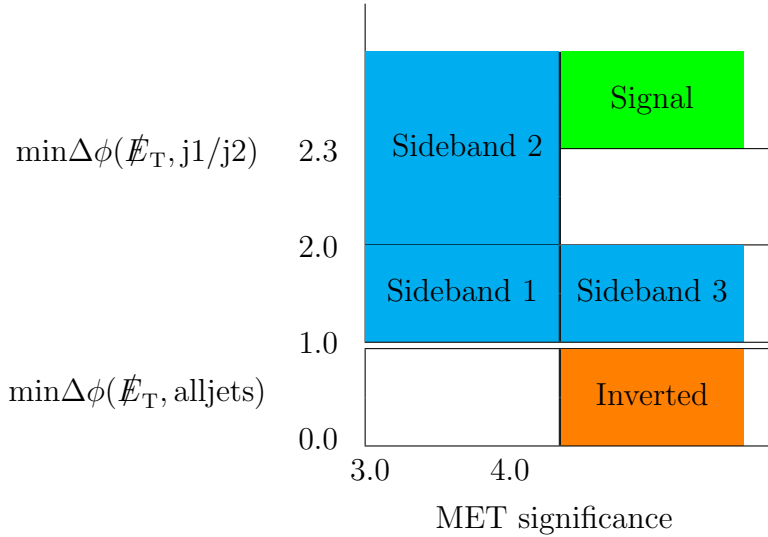


Figure 4.28.: A schematic of the regions used in the QCD background estimation.

The contribution from V+jets backgrounds in these regions is estimated using MC normalised with the **data driven** method described by Equation 4.14. The control regions used for each background in each region are defined by making the same modifications to the region that were made to the signal region to define the V+jets control regions used in Sections 4.7.2-4.7.6.

The inverted region is defined starting from the signal region, by swapping the $\min\Delta\phi(j, \cancel{E}_T^{\text{no-}\mu}) > 2.3$ requirement for a requirement that only $\min\Delta\phi(j_{1/2}, \cancel{E}_T^{\text{no-}\mu})$ is greater than 2.3, and then requiring that $\min\Delta\phi(j, \cancel{E}_T^{\text{no-}\mu})$ is less than 1. The resulting region consists of events with two signal-like jets, well separated from the \cancel{E}_T , but also an additional jet close to the \cancel{E}_T making it non-isolated. As can be seen from Figure 4.29a the inverted region is dominated by QCD events with only 20% of the events expected to come from V+jets and other background processes. The QCD shape is taken to be the shape of the data after subtracting the estimated contribution from all other background processes.

To ensure the QCD shape derived from non-isolated \cancel{E}_T is adequate to describe the QCD background with isolated \cancel{E}_T in the signal region the 3-jet region is used. This region is defined starting from the signal region by relaxing the $\min\Delta\phi(j, \cancel{E}_T^{\text{no-}\mu})$ and S requirements from greater than 2.3 to greater than 1 and from greater than 4 to greater than 3 respectively, then requiring that there are at least three jets with $p_T > 30$ GeV in

top, $W \rightarrow \tau\nu$, $Z \rightarrow \nu\nu$ and QCD multijet backgrounds have already been discussed in Sections 4.7.1, 4.7.4, 4.7.6 and 4.7.9 respectively.

Despite the methods used being similar, in several cases the inputs to the methods have been updated to take into account improved measurements of various parameters using the full Run 1 dataset which were not available at the time of the prompt analysis. For example, the impacts of the JES, JER and UES uncertainties are still estimated by recalculating the p_T of all jets and the \cancel{E}_T after varying each parameter up and down by one standard deviation and reperforming the analysis. However, the total uncertainty from these is smaller, being 6% of the total expected background yield for this analysis where it was 7% in the prompt analysis.

In addition to these changes a study was undertaken to estimate the impact of the trigger efficiency measurement uncertainties on the expected limit. As described in Section 4.5, all MC events are reweighted by the measured trigger efficiency as a function of the events sub-leading jet p_T , $\cancel{E}_T^{\text{no-}\mu}$ and M_{jj} . The uncertainty due to the reweighting process cancels in all **[1]ata driven** background estimates, as a ratio of MC event yields is taken. To estimate the size of the uncertainty that should be applied to processes not estimated with **[2]ata driven** methods, the bin with the largest uncertainty on its fit for each era was chosen. It was then assumed that all bins had this worst-case uncertainty. This assumption resulted in a 2.3% uncertainty on these non-data driven processes. Given that this error is smaller than many of the other errors considered, and that the uncertainty on the efficiency in most of the fit bins is significantly lower than this worst case, this uncertainty was considered negligible.

The fractional uncertainties on the total signal and background estimates from each source of uncertainty considered are shown in Table 4.15 in decreasing order of the size of the uncertainty on the total background yield. It can be seen that the dominant uncertainties are statistical, with these being dominated by the low number of data events in the double muon control region (see Table 4.14).

4.9. Results

The final predicted yields for each background process are shown, along with their uncertainties in Table 4.16. The total predicted event yield from background processes is $439.4 \pm 40.7 \text{ (stat)} \pm 43.5 \text{ (syst)}$. Assuming an SM produced Higgs boson which decays

Page: 116

 Number: 1 Author: ptd Subject: Highlight Date: 12/06/2016 15:40:43

 Number: 2 Author: ptd Subject: Highlight Date: 12/06/2016 15:40:49

Table 4.16.: The estimated numbers of background and signal events from each process, together with the observed yield, in the signal region. The signal yield assumes a Higgs boson mass of 125 GeV and $\mathcal{B}(H \rightarrow \text{inv}) = 100\%$. Where two errors are quoted they are the statistical and systematic uncertainties respectively, where only one is quoted it is the systematic uncertainty.

Process	Event yields
$Z \rightarrow \nu\nu$	$158.1 \pm 37.3 \pm 21.2$
$W \rightarrow e\nu$	$57.9 \pm 7.4 \pm 7.7$
$W \rightarrow \mu\nu$	$102.5 \pm 6.2 \pm 11.7$
$W \rightarrow \tau\nu$	$94.6 \pm 13.1 \pm 23.8$
top	5.5 ± 1.8
Minor backgrounds	3.9 ± 0.7
QCD multijet	17 ± 14
Total background	$439.4 \pm 40.7 \pm 43.5$
Signal(VBF)	273.1 ± 31.2
Signal(ggH)	23.1 ± 15.9
Observed data	508

100% of the time to invisible final states, 296.2 ± 39.4 (syst) events from signal processes are expected. 508 events are observed, which is slightly more than one standard deviation above the [background only] prediction. The distributions of the variables in the signal region used in the analysis selection are shown in Figure 4.31. The shapes of these distributions for data and the predicted backgrounds agree well, giving further evidence that the excess of events is not significant.

As no significant excess is observed the upper limits that can be placed on $\sigma \times \mathcal{B}$ at 95% CL are calculated assuming SM Higgs boson acceptances using the asymptotic CL_S technique described in Section 1.4. The resulting observed limits and expected limits with their 68% and 95% confidence intervals are shown in Figure 4.32a. As in the prompt analysis all systematic uncertainties and all the statistical uncertainties on the control regions except the double muon region are modelled as log-normally distributed nuisance parameters. The statistical uncertainty in the double muon control region is again modelled as gamma-normally distributed due to the low number of events in this region. Assuming SM Higgs production the resulting limits can be interpreted as limits on the invisible branching fraction of the Higgs boson, the results of this interpretation are shown in Figure 4.32b. For a Higgs boson with a mass of 125 GeV the resulting

 Number: 1 Author: ptd Subject: Highlight Date: 12/06/2016 17:35:49
[hyphenate]

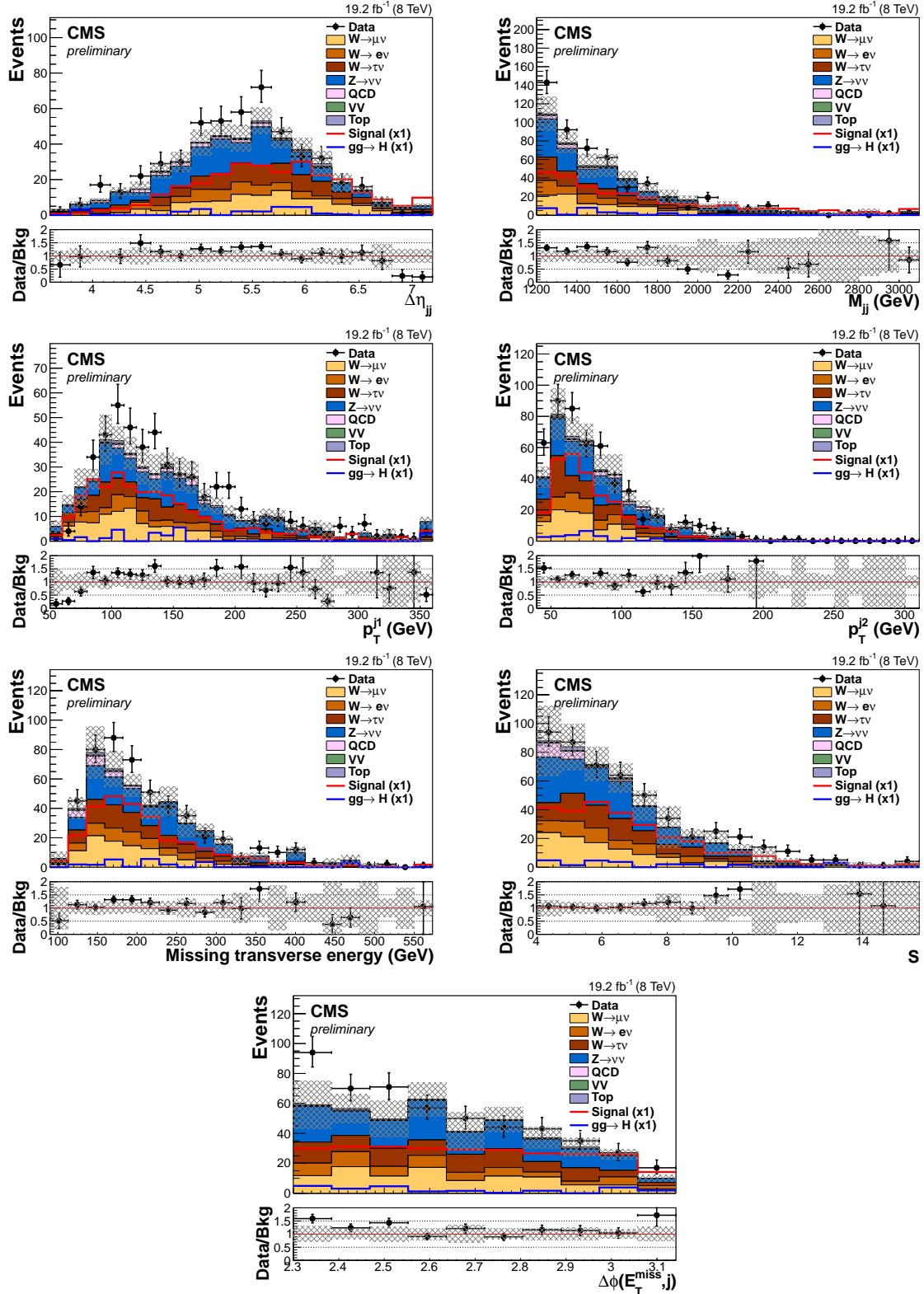


Figure 4.31.: From top to bottom and left to right $\Delta\eta_{jj}$, M_{jj} , the leading and sub-leading jet's p_T , $E_T^{\text{no-}\mu}$, \mathcal{S} and $\min\Delta\phi(j, E_T^{\text{no-}\mu})$ in the signal region. The hatched band indicates the size of the total uncertainty on the background estimate [2].

Chapter 5.

Combinations of Run 1 searches for invisibly decaying Higgs bosons

Whilst the VBF production mode offers the best sensitivity to invisibly decaying Higgs bosons, the limit on $\mathcal{B}(H \rightarrow \text{inv})$ can be improved by taking into account searches performed using other production channels. According to the CL_S method described in Section 1.4 multiple searches can be combined by constructing a likelihood, according to Equation 1.38. Combinations of the VBF analyses with the other channels are described in [\[1\]ections](#) 5.1 to 5.3.

5.1. Searches in other channels

As described in Section 1.2.1, after VBF the next most sensitive production modes to invisible Higgs boson decays are ggH and VH. VH has a much lower production rate than VBF (approximately 4 times less for a 125 GeV Higgs boson). Compensating for this low cross-section, several of the final states in VH production, particularly ZH, give very clean signatures which are easy to identify. Gluon fusion has a much higher rate than VBF, but in most cases the resulting Higgs boson is created alone so there are no visible particles in the final state. However, one or more jets can result from ISR allowing this channel to also be used.

In addition to the VBF analyses, three invisibly decaying Higgs boson searches were carried out by CMS during Run 1. Two of these searches specifically targeted the ZH production mode, one searching for events where the Z boson decayed to two leptons (the $Z(\ell\ell)H$ search) and another where it decayed to two b quarks (the $Z(b\bar{b})H$ search). The

analysis this background was reduced using requirements on $\min\Delta\phi(j, \cancel{E}_T^{\text{no-}\mu})$ and \mathcal{S} . The neutral component of the \cancel{E}_T was also required to be aligned with the charged component in ϕ . The signal region was separated into three categories with low, medium and high \cancel{E}_T and control regions where the signal region selections are relaxed or inverted are used to estimate the remaining backgrounds.

5.1.3. Monojet selection

The “monojet” search, is described in Ref. [108]. This analysis selected events with large \cancel{E}_T , one or more high- p_T jets, and no reconstructed electrons or muons. To separate events due to ggH production with ISR from those due to VH production where the vector boson decays hadronically, events were classified into three signal categories. The categorisation was sequential, i.e. if an event passed the requirements for the first category it was not considered for the second etc.

The first category targeted “unresolved” vector bosons where the high p_T of the vector boson caused its decay products to be very close together. These unresolved vector bosons were identified by searching for so-called “fat” jets with substructure with $p_T > 200$ GeV, (described in detail in Ref. [108]). One additional normal jet was allowed in this category as long as it was within $2\Delta\phi$ of the fat jet.

The second category was the resolved category where the vector boson had lower p_T and its decay products could be identified as two separate normal jets. These jets were required to have an invariant mass between 60 and 110 GeV. This range overlaps with the range used in the $Z(b\bar{b})H$ analysis regions, leading to a non-negligible number of events passing the selection for both analyses. The resolved category was therefore not used in any combinations.

The third category was the “monojet” category. Events in this category were required to have one jet with $p_T > 150$ GeV. One additional jet within $2\Delta\phi$ of the first jet was allowed to be present, with further jets causing the event to be vetoed. Control regions, which differ from the above categories by the presence of one or more leptons or photons, were used to estimate the background.

The category definitions above are not orthogonal to the VBF analysis. To remedy this any events passing the VBF parked data analysis selection were vetoed. This veto removed less than 4% of the expected signal events in the monojet category and none of the signal events expected in the resolved category. As the monojet analysis was

Table 5.3.: Uncertainties correlated between the VBF prompt data, $Z(\ell\ell)H$ and $Z(b\bar{b})H$ searches and the analyses they affect. Also quoted is the relative change in the expected limit on $\mathcal{B}(H \rightarrow \text{inv})$ on removing each uncertainty from the analysis.

Uncertainty	Analyses affected	$\frac{\Delta((\text{limit}))}{\text{limit}}$ on removal
JES	VBF, $Z(\ell\ell)H$	-0.13
PDFs	VBF, $Z(b\bar{b})$, $Z(\ell\ell)H$	-10
QCD scale	VBF, $Z(b\bar{b})$, $Z(\ell\ell)H$	-0.0 \pm 1
Luminosity	VBF, $Z(b\bar{b})H$, $Z(\ell\ell)H$	-0.02
JER	VBF, $Z(\ell\ell)H$	<0.01
UES	VBF, $Z(b\bar{b})H$, $Z(\ell\ell)H$	<0.01
Lepton efficiency	VBF, $Z(\ell\ell)H$	<0.01

available mass points (these ranged from 110 to 400 GeV). Multiplying the interpolated efficiencies for a mass hypothesis by the corresponding Higgs boson production cross-section gives a signal yield estimate for that mass.

In order to combine limits from multiple production channels it is also necessary to make an assumption about the relative cross-section of these two production mechanisms. Assuming the SM production cross-sections, a combination was performed between all three analyses in the mass range 115 to 145 GeV. The results of this combination can be seen in Figure 5.2. The 95% CL observed (expected) limit on $\mathcal{B}(H \rightarrow \text{inv})$ for a 125 GeV Higgs boson was found to be 0.58 (0.44).

Whilst the $Z(b\bar{b})H$ search has no MC samples available for Higgs boson masses above 145 GeV, the $Z(\ell\ell)H$ search has samples up to 300 GeV. The VBF and $Z(\ell\ell)H$ searches were therefore combined in the mass range 115 to 300 GeV. The results of this combination are shown in Figure 5.3. It can be seen that there is an approximately one sigma excess for all values of the Higgs boson mass. This excess is driven by the VBF channel, which also sees a one sigma excess (as shown in Figure 4.12) which is 100% correlated across all Higgs boson mass hypotheses. The observed excess is therefore not significant.

5.3. Combination with the parked data VBF search

The parked data VBF analysis was combined with both the ZH searches and the monojet search, which was finished in 2015 [3]. The prompt data VBF analysis was not included in this combination due to its large overlap with the parked data analysis. As discussed

 Number: 1 Author: ptd Subject: Highlight Date: 12/06/2016 17:42:35
-0.10

Table 5.4.: Uncertainties correlated between the VBF parked data, $Z(\ell\ell)H$, $Z(b\bar{b})H$ and monojet searches and the analyses they affect.

Nuisance	Analyses which it affects
JES	VBF, $Z(\ell\ell)H$
PDFs	VBF, $Z(b\bar{b})$, $Z(\ell\ell)H$, monojet
QCD scale	VBF, $Z(b\bar{b})$, $Z(\ell\ell)H$, monojet
Luminosity	VBF, $Z(b\bar{b})H$, $Z(\ell\ell)H$, monojet
JER	VBF, $Z(\ell\ell)H$
UES	VBF, $Z(b\bar{b})H$, $Z(\ell\ell)H$
Muon identification efficiency	VBF, $Z(\ell\ell)H$, monojet
Electron identification efficiency	VBF, $Z(\ell\ell)H$
Diboson cross-section	VBF, monojet

$\Delta\eta_{jj}$ requirement. The $Z(\ell\ell)H$ analysis uses low p_T jets with $p_T > 30$ GeV similar to those used to calculate $\min\Delta\phi(j, \cancel{E}_T^{\text{no-}\mu})$ in the VBF analysis, but very different from the high p_T central jets in the monojet analysis. The decision was therefore taken to correlate the VBF and $Z(\ell\ell)H$ analyses JES and JER uncertainties and to leave those from the monojet analysis uncorrelated. A study of the impact of [this](#)  choices was carried out, and it was found that all combinations of correlations resulted in the same expected limit.

In the case of the \cancel{E}_T uncertainties, the two ZH searches and the VBF search use the same \cancel{E}_T corrections, whereas the monojet search applies a different set of corrections [108]. The monojet analysis UES uncertainty was therefore not correlated with that from the other analyses.

With these uncertainty correlations the four searches were combined for a Higgs boson mass of 125 GeV assuming SM production-cross-sections for each channel. The 95% CL observed (expected) limit on $\mathcal{B}(H \rightarrow \text{inv})$ for a 125 GeV Higgs boson was found to be 0.36 (0.30). The log-likelihood obtained as a function of $\mathcal{B}(H \rightarrow \text{inv})$ is shown in Figure 5.4. The favoured observed value can be seen to be greater than zero, however this is not significant.

As well as the full combination of all analysis categories, sub-combinations were also performed of all the categories targeting a particular production mode. The results of these sub-combinations and the full combination is shown in Figure 5.5, where the VBF-tagged limit comes from the VBF parked data analysis, the VH-tagged limit from

 Number: 1 Author: ptd Subject: Inserted Text Date: 12/06/2016 17:44:31
these

Another difference from the CMS analysis is that the studies described in this chapter use MADGRAPH to simulate the hard-scattering process, whilst the CMS analysis uses POWHEG. Both the internal CMS simulation and that described in this chapter use PYTHIA for parton-showering and hadronisation. Yields and kinematic distributions of events after selection criteria are applied are obtained from these simulations using an analysis framework developed and validated by the MasterCode collaboration [109].

The validation of these simulations and the analysis framework was carried out in two steps, both using a centre of mass energy of 8 TeV. First, POWHEG and PYTHIA were used to simulate a **1** BF produced 125 GeV Higgs boson decaying to invisible final states, as in the internal CMS simulation. This sample of events was then processed using the **2** DELPHES based reconstruction and MasterCode analysis framework. The resulting event yields were compared to those obtained from a **3** POWHEG and **4** PYTHIA produced sample processed using the full CMS reconstruction and analysis framework. The event yields were found to agree within 10%.

The second step was to compare the 125 GeV **5** BF produced invisibly decaying Higgs boson sample generated with POWHEG to one generated with MADGRAPH with both samples being processed using DELPHES. This comparison was carried out starting from the following requirements:

$$\begin{aligned} \eta_{j1} \cdot \eta_{j2} < 0, \text{jet 1 and jet 2} \not{E}_T > 35 \text{ GeV}, \mathcal{S} > 3, \\ \Delta\eta_{jj} > 3.6, M_{jj} > 700 \text{ GeV}, \text{L1} \not{E}_T > 40 \text{ GeV}. \end{aligned} \quad (6.1)$$

Cuts were then added to this selection one at a time until the applied selection was the same as the parked data analysis signal region selection, which is described in Equation 4.13. The resulting event yields can be seen in Table 6.1. It is important to note that the MADGRAPH samples include both VBF and VH production of the Higgs boson, while the POWHEG samples only include VBF production. This difference explains the MADGRAPH yield being larger than that from POWHEG at the starting point of the comparison. As the selection is tightened the disagreement between POWHEG and MADGRAPH can be seen to reduce until the difference in yield is below 5% for the full selection, where very few VH events are still present. Only event yields after the full selection are used in the results presented in Section 6.2, so the level of agreement is considered acceptable.

The Run 1 signal and background estimates made public [\[7\]](#) Ref. [2] are quoted with their statistical and systematic errors. However, no information on the correlation between

Page: 136

 Number: 1 Author: ptd Subject: Highlight Date: 12/06/2016 17:45:52
[hyphenate]

 Number: 2 Author: ptd Subject: Highlight Date: 12/06/2016 17:46:08
[hyphenate]

 Number: 3 Author: ptd Subject: Highlight Date: 12/06/2016 17:46:44
POWHEG-

 Number: 4 Author: ptd Subject: Highlight Date: 12/06/2016 17:46:30
[hyphenate]

 Number: 5 Author: ptd Subject: Highlight Date: 12/06/2016 17:51:15

 Number: 6 Author: ptd Subject: Highlight Date: 12/06/2016 17:52:04
italic "p"

 Number: 7 Author: ptd Subject: Inserted Text Date: 12/06/2016 17:52:27
given

^[1]Bibliography

- [1] CMS Collaboration, “Search for invisible decays of Higgs bosons in the vector boson fusion and associated ZH production modes”, *Eur. Phys. J.* **C74** (2014) 2980, doi:10.1140/epjc/s10052-014-2980-6, arXiv:1404.1344.
- [2] CMS Collaboration, “Search for invisible decays of Higgs bosons in the vector boson fusion production mode”, Technical Report CMS-PAS-HIG-14-038, CERN, Geneva, (2015).
- [3] CMS Collaboration, “A combination of searches for the invisible decays of the Higgs boson using the CMS detector”, Technical Report CMS-PAS-HIG-15-012, CERN, Geneva, (2015).
- [4] J. Brooke, M. R. Buckley, P. Dunne et al., “Vector Boson Fusion Searches for Dark Matter at the LHC”, arXiv:1603.07739.
- [5] R. Aggleton, C. Asawatangtrakuldee, J. Brooke, O. Buchmueller, D. Colling, G. Davies, P. Dunne, S. Kumar, Q. Li, A. Magnan, K. Mazumdar, A. Nikitenko, J. Pela, P. Srivastavas, D. Wang, “Search for an Invisible Higgs Boson”, *CMS Analysis Note: AN-12-403* (2012).
- [6] S. L. Glashow, “Partial Symmetries of Weak Interactions”, *Nucl. Phys.* **22** (1961) 579, doi:10.1016/0029-5582(61)90469-2.
- [7] S. Weinberg, “A Model [2]F Leptons”, *Phys. Rev. Lett.* **19** (1967) 1264–1266.
- [8] A. Salam, “Weak and electromagnetic interactions”, in *Elementary particle physics: relativistic groups and analyticity*, N. Svartholm, ed., p. 367. Almqvist & Wiksell, Stockholm, 1968. Proceedings of the eighth Nobel symposium.
- [9] Y. N. Murray Gell-Mann, “The eightfold way a review, with a collection of reprints,” [3]

Page: 154

 Number: 1 Author: ptd Subject: Highlight Date: 12/06/2016 18:37:59

[Formatting of references needs to follow convention, and consistent as well. Please look at this in detail. I highlight a few places where I found issues below; not necessarily an exhaustive list.]

For most journals, there are conventional abbreviations that are used in references. For instance, Phys. Lett.; Comp. Phys. Comm., etc. You can find what the standard abbreviations are by eg looking in the references in a CMS publication.]

 Number: 2 Author: ptd Subject: Highlight Date: 12/06/2016 18:24:20
of

 Number: 3 Author: ptd Subject: Highlight Date: 12/06/2016 18:24:47

- [10] D. Hanneke, S. Fogwell, and G. Gabrielse, “New Measurement of the Electron Magnetic Moment and the Fine Structure Constant”, *Phys. Rev. Lett.* **100** (Mar, 2008) 120801, doi:10.1103/PhysRevLett.100.120801.
- [11] E. Noether, “Invariant Variation Problems”, *Gott. Nachr.* **1918** (1918) 235–257, doi:10.1080/00411457108231446, arXiv:physics/0503066. [Transp. Theory Statist. Phys.1,186(1971)].
- [12] E. Noether, “Invariant variation problems”, *Transport Theory and Statistical Physics* **1** (1971), no. 3, 186–207, doi:10.1080/00411457108231446.
- [13] C. N. Yang and R. L. Mills, “Conservation of Isotopic Spin and Isotopic Gauge Invariance”, *Phys. Rev.* **96** (Oct, 1954) 191–195, doi:10.1103/PhysRev.96.191.
- [14] Particle Data Group Collaboration, “Review of Particle Physics”, *Chin. Phys. C* **38** (2014) 090001, doi:10.1088/1674-1137/38/9/090001.
- [15] F. Englert and R. Brout, “Broken symmetry and the mass of gauge vector mesons”, *Phys. Rev. Lett.* **13** (1964) 321, doi:10.1103/PhysRevLett.13.321.
- [16] P. W. Higgs, “Broken symmetries, massless particles and gauge fields”, *Phys. Lett.* **12** (1964) 132, doi:10.1016/0031-9163(64)91136-9.
- [17] P. W. Higgs, “Broken symmetries and the masses of gauge bosons”, *Phys. Rev. Lett.* **13** (1964) 508, doi:10.1103/PhysRevLett.13.508.
- [18] G. S. Guralnik, C. R. Hagen, and T. W. B. Kibble, “Global conservation laws and massless particles”, *Phys. Rev. Lett.* **13** (1964) 585, doi:10.1103/PhysRevLett.13.585.
- [19] P. W. Higgs, “Spontaneous symmetry breakdown without massless bosons”, *Phys. Rev.* **145** (1966) 1156, doi:10.1103/PhysRev.145.1156.
- [20] T. W. B. Kibble, “Symmetry breaking in non-Abelian gauge theories”, *Phys. Rev.* **155** (1967) 1554, doi:10.1103/PhysRev.155.1554.
- [21] D. Griffiths, “Introduction to Elementary Particles”. Physics textbook. Wiley, 2008.
- [22] ATLAS Collaboration, “Observation of a new particle in the search for the Standard Model Higgs boson with the **ATLAS** detector at the **LHC**”, *Physics Letters B* **716** (2012), no. 1, 1 – 29, doi:<http://dx.doi.org/10.1016/j.physletb.2012.08.020>.

Page: 155

 Number: 1 Author: ptd Subject: Highlight Date: 12/06/2016 18:39:19
Phys. Lett. B

 Number: 2 Author: ptd Subject: Highlight Date: 12/06/2016 18:26:01

 Number: 3 Author: ptd Subject: Highlight Date: 12/06/2016 18:26:11

- [23] CMS Collaboration, “Observation of a new boson at a mass of 125 GeV with the **[1CMS]** experiment at the **[2LHC]**”, *Physics Letters B* **716** (2012), no. 1, 30 – 61, doi:<http://dx.doi.org/10.1016/j.physletb.2012.08.021>.
- [24] Super-Kamiokande Collaboration, “Measurements of the Solar Neutrino Flux from Super-Kamiokande’s First 300 Days”, *Phys. Rev. Lett.* **81** (Aug, 1998) 1158–1162, doi:[10.1103/PhysRevLett.81.1158](https://doi.org/10.1103/PhysRevLett.81.1158).
- [25] F. Zwicky, “Die Rotverschiebung von extragalaktischen Nebeln”, *Helv. Phys. Acta* **6** (1933) 110–127.
- [26] D. Clowe, M. Brada, A. H. Gonzalez et al., “A Direct Empirical Proof of the Existence of Dark Matter”, *The Astrophysical Journal Letters* **648** (2006), no. 2, L109.
- [27] Planck Collaboration, “Planck 2013 results. I. Overview of products and scientific results”, *Astronomy and Astrophysics* **571** (2014) A1, doi:[10.1051/0004-6361/201321529](https://doi.org/10.1051/0004-6361/201321529).
- [28] K. Freese, “Review of Observational Evidence for Dark Matter in the Universe and in upcoming searches for Dark Stars”, *EAS Publ. Ser.* **36** (2009) 113–126, doi:[10.1051/eas/0936016](https://doi.org/10.1051/eas/0936016), arXiv:0812.4005.
- [29] LHC Higgs Cross Section Working Group, S. Dittmaier, et al., “Handbook of LHC Higgs Cross Sections: 3. Higgs Properties: Report of the LHC Higgs Cross Section Working Group”, Technical Report **[3arXiv:1307.1347]**. CERN-2013-004, Geneva, (2013). Comments: 404 pages, 139 figures, to be submitted to CERN Report. Working Group web page:
<https://twiki.cern.ch/twiki/bin/view/LHCPhysics/CrossSections>.
- [30] CMS Collaboration, “The CMS experiment at the CERN LHC”, *JINST* **3** (2008) S08004, doi:[10.1088/1748-0221/3/08/S08004](https://doi.org/10.1088/1748-0221/3/08/S08004).
- [31] D. J. Gross and F. Wilczek, “Ultraviolet Behavior of Non-Abelian Gauge Theories”, *Phys. Rev. Lett.* **30** (Jun, 1973) 1343–1346, doi:[10.1103/PhysRevLett.30.1343](https://doi.org/10.1103/PhysRevLett.30.1343).
- [32] H. D. Politzer, “Reliable Perturbative Results for Strong Interactions?”, *Phys. Rev. Lett.* **30** (Jun, 1973) 1346–1349, doi:[10.1103/PhysRevLett.30.1346](https://doi.org/10.1103/PhysRevLett.30.1346).

Page: 156

 Number: 1 Author: ptd Subject: Highlight Date: 12/06/2016 18:26:18

 Number: 2 Author: ptd Subject: Highlight Date: 12/06/2016 18:26:23

 Number: 3 Author: ptd Subject: Highlight Date: 12/06/2016 18:27:32
[seems to be out of order]

- [33] CMS Collaboration, “Constraints on the Higgs boson width from off-shell production and decay to Z-boson pairs”, *Physics Letters B* **736** (2014) 64 – 85, doi:<http://dx.doi.org/10.1016/j.physletb.2014.06.077>.
- [34] ATLAS Collaboration, “The ATLAS Experiment at the CERN Large Hadron Collider”, *JINST* **3** (2008) S08003, doi:[10.1088/1748-0221/3/08/S08003](https://doi.org/10.1088/1748-0221/3/08/S08003).
- [35] “Measurements of the Higgs boson production and decay rates and constraints on its couplings from a combined ATLAS and CMS analysis of the LHC pp collision data at $\sqrt{s} = 7$ and 8 TeV”, Technical Report CMS-PAS-HIG-15-002, CERN, Geneva, (2015).
- [36] R. C. Cotta, J. L. Hewett, M.-P. Le et al., “Bounds on dark matter interactions with electroweak gauge bosons”, *Phys. Rev. D* **88** (Dec, 2013) 116009, doi:[10.1103/PhysRevD.88.116009](https://doi.org/10.1103/PhysRevD.88.116009).
- [37] M. R. Buckley, D. Feld, and D. Gonçalves, “Scalar simplified models for dark matter”, *Phys. Rev. D* **91** (Jan, 2015) 015017, doi:[10.1103/PhysRevD.91.015017](https://doi.org/10.1103/PhysRevD.91.015017).
- [38] G. D’Ambrosio, G. Giudice, G. Isidori et al., “Minimal flavour violation: an effective field theory approach”, *Nuclear Physics B* **645** (2002), no. 12, 155 – 187, doi:[http://dx.doi.org/10.1016/S0550-3213\(02\)00836-2](http://dx.doi.org/10.1016/S0550-3213(02)00836-2).
- [39] S. Agostinelli, J. Allison, K. Amako et al., “Geant4a simulation toolkit”, *Nuclear Instruments and Methods in Physics Research Section A: Accelerators, Spectrometers, Detectors and Associated Equipment* **506** (2003), no. 3, 250 – 303, doi:[http://dx.doi.org/10.1016/S0168-9002\(03\)01368-8](http://dx.doi.org/10.1016/S0168-9002(03)01368-8).
- [40] J. Favereau, C. Delaere, P. Demin et al., “DELPHES 3: a modular framework for fast simulation of a generic collider experiment”, *Journal of High Energy Physics* **2014** (2014), no. 2, 1–26, doi:[10.1007/JHEP02\(2014\)057](https://doi.org/10.1007/JHEP02(2014)057).
- [41] T. Sjöstrand, S. Mrenna, and P. Skands, “A brief introduction to PYTHIA 8.1”, *Computer Physics Communications* **178** (2008), no. 11, 852 – 867, doi:<http://dx.doi.org/10.1016/j.cpc.2008.01.036>.
- [42] J. Alwall, R. Frederix, S. Frixione et al., “The automated computation of tree-level and next-to-leading order differential cross sections, and their matching to parton shower simulations”, *Journal of High Energy Physics* **2014** (2014), no. 7, 1–157, doi:[10.1007/JHEP07\(2014\)079](https://doi.org/10.1007/JHEP07(2014)079).

Page: 157

 Number: 1 Author: ptd Subject: Highlight Date: 12/06/2016 18:33:15

 Number: 2 Author: ptd Subject: Highlight Date: 12/06/2016 18:28:48

 Number: 3 Author: ptd Subject: Highlight Date: 12/06/2016 18:35:11

[The standard abbreviation for this journal is Comp. Phys. Comm.; use here and everywhere else where applicable.]

 Number: 4 Author: ptd Subject: Highlight Date: 12/06/2016 18:33:06

[see comment in Reference 43]

- [43] P. Nason, “A New method for combining NLO QCD with shower Monte Carlo algorithms”, *JHEP* **11** (2004) 040, doi:10.1088/1126-6708/2004/11/040, arXiv:hep-ph/0409146.
- [44] S. Frixione, P. Nason, and C. Oleari, “Matching NLO QCD computations with Parton Shower simulations: the POWHEG method”, *JHEP* **11** (2007) 070, doi:10.1088/1126-6708/2007/11/070, arXiv:0709.2092.
- [45] S. Alioli, P. Nason, C. Oleari et al., “A general framework for implementing NLO calculations in shower Monte Carlo programs: the POWHEG BOX”, *JHEP* **06** (2010) 043, doi:10.1007/JHEP06(2010)043, arXiv:1002.2581.
- [46] J. Campbell, R. K. Ellis, and D. Rainwater, “Next-to-leading order QCD predictions for $W + 2$ jet and $Z + 2$ jet production at the CERN LHC”, *Phys. Rev. D* **68** (Nov, 2003) 094021, doi:10.1103/PhysRevD.68.094021.
- [47] J. Baglio et al., “Release Note - VBFNLO 2.7.0”, arXiv:1404.3940.
- [48] K. Arnold et al., “VBFNLO: A Parton Level Monte Carlo for Processes with Electroweak Bosons – Manual for Version 2.5.0”, arXiv:1107.4038.
- [49] K. Arnold, M. Bhr, G. Bozzi et al., ‘**bfnlo**: A parton level Monte Carlo for processes with electroweak bosons”, *Computer Physics Communications* **180** (2009), no. 9, 1661 – 1670, doi:<http://dx.doi.org/10.1016/j.cpc.2009.03.006>.
- [50] M. Czakon and A. Mitov, “Top++: A program for the calculation of the top-pair cross-section at hadron colliders”, *Computer Physics Communications* **185** (2014), no. 11, 2930 – 2938, doi:<http://dx.doi.org/10.1016/j.cpc.2014.06.021>.
- [51] Y. Li and F. Petriello, “Combining QCD and electroweak corrections to dilepton production in the framework of the FEWZ simulation code”, *Phys. Rev. D* **86** (Nov, 2012) 094034, doi:10.1103/PhysRevD.86.094034.
- [52] F. Krauss, “Phenomenology at collider experiments”, http://www.ippp.dur.ac.uk/~krauss/Lectures/MonteCarlos/Pheno_5_08.pdf (Accessed March, 2016).
- [53] “Procedure for the LHC Higgs boson search combination in summer 2011”, Technical Report ATL-PHYS-PUB-2011-011, CMS NOTE 2011/005, CERN, Geneva, (Aug, 2011).

Page: 158

 Number: 1 Author: ptd Subject: Highlight Date: 12/06/2016 18:32:41

[I believe this is indeed the standard abbreviation, to be used for References. In many cases you use "Journal of High energy Physics", which you should instead replace with "JHEP".]

 Number: 2 Author: ptd Subject: Highlight Date: 12/06/2016 18:30:05

VBFNLO

 Number: 3 Author: ptd Subject: Highlight Date: 12/06/2016 19:03:16

 Number: 4 Author: ptd Subject: Highlight Date: 12/06/2016 19:03:23

 Number: 5 Author: ptd Subject: Highlight Date: 12/06/2016 19:03:38

- [54] G. Cowan, K. Cranmer, E. Gross et al., “Asymptotic formulae for likelihood-based tests of new physics”, *Eur. Phys. J.* **C71** (2011) 1554,
[doi:10.1140/epjc/s10052-011-1554-0](https://doi.org/10.1140/epjc/s10052-011-1554-0), [10.1140/epjc/s10052-013-2501-z](https://doi.org/10.1140/epjc/s10052-013-2501-z),
[arXiv:1007.1727](https://arxiv.org/abs/1007.1727). [Erratum: [\[1\]](#) *Eur. Phys. J.* C73,2501(2013)].
- [55] L. Evans and P. Bryant, “LHC Machine”, *JINST* **3** (2008), no. 08, S08001,
[doi:10.1088/1748-0221/3/08/S08001](https://doi.org/10.1088/1748-0221/3/08/S08001).
- [56] LEP Injector Study Group, “LEP design report, volume I: The LEP injector chain; LEP design report, volume II: The LEP Main Ring”. CERN, Geneva, 1983.
- [57] ALICE Collaboration, “The ALICE experiment at the CERN LHC”, *JINST* **3** (2008) S08002, [doi:10.1088/1748-0221/3/08/S08002](https://doi.org/10.1088/1748-0221/3/08/S08002).
- [58] LHCb Collaboration, “The LHCb Detector at the LHC”, *JINST* **3** (2008) S08005, [doi:10.1088/1748-0221/3/08/S08005](https://doi.org/10.1088/1748-0221/3/08/S08005).
- [59] ATLAS collaboration, “ATLAS detector photos”,
http://atlas.ch/atlas_photos/lhc/lhc_03.html (Accessed March, 2016).
- [60] M. Benedikt, P. Collier, V. Mertens et al., “LHC Design Report”. CERN, Geneva, 2004.
- [61] CMS Collaboration, “CMS Luminosity - Public Result” [\[2\]](#) ,.
- [62] W. J. Stirling, “Private communicatio” [\[3\]](#) ,.
- [63] T. Sakuma and T. McCauley, “Detector and Event Visualization with SketchUp at the CMS Experiment”, *J. Phys.: Conf. Ser.* **513** 022032,
[doi:10.1088/1742-6596/513/2/022032](https://doi.org/10.1088/1742-6596/513/2/022032).
- [64] CMS Collaboration, “Interactive Slice of the CMS detector”, *CMS Document 4172-v2*.
- [65] Tricomi, Alessia, “Performances of the ATLAS and CMS silicon tracker”, *Eur. Phys. J. C* **33** (2004) s1023–s1025, [doi:10.1140/epjcd/s2004-03-1801-1](https://doi.org/10.1140/epjcd/s2004-03-1801-1).
- [66] CMS Collaboration, “Description and performance of track and primary-vertex reconstruction with the CMS tracker”, *J. Instrum.* **9** (May, 2014) P10009. 80 p.
Comments: Replaced with published version. Added journal reference and DOI.
- [67] CMS Collaboration, “History of ECAL response with laser data” ,.

Page: 159

 Number: 1 Author: ptd Subject: Highlight Date: 12/06/2016 19:29:42
[Use exactly same formatting of reference as above.]

 Number: 2 Author: ptd Subject: Highlight Date: 12/06/2016 19:30:19

 Number: 3 Author: ptd Subject: Highlight Date: 12/06/2016 19:39:32
